VNIVERSITAT DE VALÈNCIA

Recursive methods in quantum field theory and top quark physics at the LHC

Paola Ferrario

IFIC, Departamento de Física Teórica

Tesis doctoral, July 2010

Contents

Introducción

El Gran Colisionador de Hadrones (conocido por sus siglas en inglés, LHC) ya se ha puesto en marcha y se han producido las primeras colisiones. Hay una gran expectación hacia los datos que serán recogidos en los próximos años: su energía a pleno rendimiento, 14 TeV en el centro de masa, nos guiará en la exploración de la física a la escala del TeV, donde esperamos encontrar respuesta a algunos de los misterios de la Naturaleza aún por desvelar. El LHC ya ha registrado la energía más alta alcanzada hasta hoy en aceleradores, con colisiones a 2.36 TeV de energía en el centro de masa, en noviembre del año pasado y a lo largo de los próximos años la verá subir hasta llegar a los 14 TeV.

Al principio de los años '70 el Modelo Estándar (SM) de las interacciones fundamentales se completa y en las décadas siguientes se confirma con una precisión muy alta en un gran número de datos experimentales. Asimismo, se descubren partículas predichas anteriormente, como los bosones de gauge Z y W o el quark top y la composición de la Naturaleza en términos de partículas se comprende cada vez mejor. El Modelo Estándar es una teoría de gauge basada en el grupo de simetría $SU(3)_C \otimes SU(2)_L \otimes U(1)_Y$ y describe tres de las cuatro fuerzas fundamentales presentes en la Naturaleza: la fuerte, la débil y la electromagnética. La cuarta fuerza es la gravedad, que hasta ahora no se ha conseguido incorporar. Las partículas elementales en el Modelo Estándar se clasifican como leptones y quarks, los cuales son fermiones, y bosones de gauge, que son responsables de las interacciones.

No obstante, algunas preguntas quedan todavía abiertas: ¿cuál es el origen de las masas? ¿Por qué estamos hechos de materia y no de antimateria? ¿Qué es esa materia oscura que constituye la mayor parte de nuestro universo y, aun así, no podemos ver? El LHC tiene como objetivo encontrar respuesta a estos y más problemas en los próximos años.

El LHC es un colisionador donde chocan dos haces de protones y está compuesto por dos anillos de alrededor de 27 km de circunferencia. Los haces se encuentran en cuatro puntos, donde están situados cinco experimentos. Hay dos detectores de alta luminosidad, dedicados a distintas funciones, ATLAS y CMS, y dos de baja luminosidad, TOTEM y LHCb, de los cuales el primero tiene como objetivo la detección de protones a pequeños ángulos y el segundo la física del B. Asimismo, existe también un experimento de iones, ALICE, que trabajará con haces de iones de plomo.

Uno de los objetivos principales de ATLAS y CMS es encontrar el bosón de Higgs. El mecanismo de Higgs explica que aquellas partículas que tienen masa la adquieren a través

de la interacción con un campo escalar, llamado bosón de Higgs. A pesar de haberse desarrollado muchas teorías que incluyen uno o más bosones de Higgs, también en escenarios supersimétricos, nadie todavía lo ha detectado hasta hoy. La cota inferior que viene de búsquedas directas se sitúa alrededor de los 114 TeV al 95% de nivel de confianza. Un ajuste global al Modelo Estándar de los datos electrodébiles de LEP indica una preferencia para un Higgs ligero, con un límite superior de 182 GeV. Puesto que argumentos de unitariedad dan un límite superior de 1.2 TeV, el LHC cubrirá el intervalo completo de energías donde nos esperamos encontrar el Higgs. Además, la alta energía del LHC causará un considerable aumento de la sección eficaz de producción del Higgs, comparado con Tevatron. Por eso, contaremos con estadística suficiente para encontrar una señal definitiva. Si esto no aconteciera, se investigarán modelos alternativos. Especialmente en este caso, es muy importante probar modelos como supersimetría (SUSY), ya que, en principio, partículas supersimétricas con masas menores que unos TeV son accesibles a los experimentos. Algunos de los modelos de SUSY pueden explicar también la discrepancia que observamos en el universo entre materia y antimateria. Efectivamente, en SUSY se pueden encontrar nuevas fuentes de violación de CP, distintas a las del Modelo Estándar, así como en las desintegraciones raras de los mesones B. El misterio de la materia oscura puede también beneficiarse de los descubrimientos de SUSY, ya que la partícula supersimétrica más ligera es un candidato excelente para ella. Otro candidato posible puede venir de modelos de dimensiones extra. En estos modelos se introducen más dimensiones espaciales curvadas de tal forma que quedan ocultas en el mundo macroscópico. ATLAS y CMS podrían detectar estas dimensiones escondidas, por medio de excitaciones de Kaluza-Klein de partículas del Modelo Estándar o incluso del gravitón. Este tipo de modelos sería también una manera de estudiar una teoría cuántica de la gravedad, que vive en un mundo con más de tres dimensiones.

Antes de que empiece la emocionante era de los descubrimientos, se ha de pasar por un periodo de medidas precisas de los procesos del Modelo Estándar. Esto es útil, no solo para calibrar los detectores, sino en sí mismo porque se entrará en escalas y regiones del espacio fásico nunca alcanzadas, donde los procesos del SM no han sido nunca estudiados. Esto permitirá poner límites más altos, por ejemplo, sobre las funciones de distribución partónicas, así como probar el funcionamiento correcto de los generadores Monte Carlo en un intervalo de energía más amplio. Por último, procesos como W/Z + jets o produccíon de quark top constituyen un fondo considerable para procesos de nueva física y hace falta conocerlos con gran precisión.

La alta luminosidad de los dos detectores ATLAS y CMS ha sido necesaria porque muchos de los procesos del SM tienen una baja sección eficaz en el LHC. Por otro lado, tener un gran número de partículas colisionando por segundo aumenta la probabilidad de colisiones inélasticas y ésta es la razón por la cual los protones del haz están divididos en grupos. El balance entre estos dos requerimientos ha llevado a un intervalo entre dos colisiones de los haces de 25 ns. La luminosidad a pleno rendimiento nominal es $\mathcal{L} = 10^{34}\mathrm{cm}^{-2}\mathrm{s}^{-1}$. Los partones que colisionan dentro del protón llevan fracción de momento x_1 and x_2. La energía en el centro de masa del proceso individual es entonces $\sqrt{\hat{s}} = \sqrt{x_1 x_2 s}$, donde $\sqrt{s} = 14$ TeV a pleno régimen. Esto significa que la energía accesible es alrededor de

unos TeV, por lo tanto es posible en principio detectar partículas con masas en ese intervalo. Tevatron, que hace colisionar protones y antiprotones, con su energía en el centro de masa de 1.96 TeV ya ha excluido la existencia de nuevas resonancias en distintos modelos con masas más bajas que 1 TeV.

Mientras que LEP colisionaba electrones y protones, el LHC acelera dos haces de protones, lo cual significa que en cada colisión se puede presentar más de un estado inicial y, por consiguiente, más de una interacción fundamental para cada choque. Esto implica que nuestro conocimiento de los procesos físicos que ocurren sea menos preciso, porque los partones que forman parte del protón pueden mezclarse con los estados finales del proceso. Siendo las partículas del haz hadrones, los procesos generados en el LHC están gobernados principalmente por la Cromodinámica Cuántica (QCD). El problema principal de QCD es que la interacción es fuerte (varios órdenes de magnitud más que la débil o la electromagnética), por lo tanto la teoría perturbativa tiene un ámbito de aplicación limitado. La constante de acoplo de QCD varía de tal forma que es pequeña para grandes momentos transferidos, mientras que crece cuando el momento transferido decrece. Entonces, solo se pueden calcular perturbativamente aquellos procesos con alto intercambio de momento, como en el caso de la producción de partículas pesadas, mientras que la hadronización ha de ser enfocada con técnicas no perturbativas. Por lo que se refiere al análisis perturbativo, en el LHC se producirá un gran número de procesos, tanto de señal, como de fondo, especialmente emisión de hadrones a corta distancia. Por eso, es de crucial importancia conocer extremadamente bien el fondo, para ser capaces de distinguir de ése la posible señal de nueva física. Por esta razón, todos los procesos necesitan ser calculados en QCD perturbativa.

Mi trabajo de tesis quiere afrontar el desafío de la nueva física del LHC desde dos puntos de vista. Por un lado, necesitamos cálculos más allá del nivel árbol para obtener una precisión teórica comparable con la precisión de los datos experimentales. De hecho, en experimentos como ATLAS y CMS, los errores estadísticos serán muy bajos. Otras fuentes de errores, como la incertidumbre en las funciones de distribución partónicas y la luminosidad se pueden reducir significativamente tomando el cociente de los observables de interés con determinados procesos del Modelo Estándar, como la producción de Z, W y $t\bar{t}$. Por lo tanto, son indispensables cálculos por lo menos a segundo orden en teoría de las perturbaciones (NLO). Cálculos a un order superior de expansión perturbativa existen solo para un número bajo de *jets* y más allá de ese orden hay muy pocos. Cálculos a órdenes superiores al nivel árbol por lo general son bastante complicados, por lo tanto son útiles nuevos métodos para desarrollarlos. Nuestro objetivo es simplificar y hacer más compactas las expresiones de amplitudes con n patas externas a nivel árbol, con el fin de extenderlas a uno o más *loops* y hacer más sencillas las amplitudes a órdenes superiores. Discutiremos esto en los capítulos 2 y 3.

Por otro lado, la posibilidad de detectar nuevas partículas en la región del TeV hace indispensable la comprensión de la resolución alcanzable. En los capítulos 5 y 6, examinamos la posibilidad de detectar nuevas resonancias que se desintegran a un par de quark top-antitop, en colisionadores de alta energía. Efectivamente, existen distintos modelos de nueva física que introducen partículas masivas, como los axigluones, los gluones de

Kaluza-Klein o los colorones. Algunas de ellas, cuando se desintegran a un par de quark top, producen una asimetría de carga, ya a nivel árbol. En nuestro trabajo, exploramos la posibilidad de medir este tipo de asimetrías en colisionadores hadrónicos. En particular, nos centramos en el escenario del LHC, con el fin de dar una estimación del alcance estadístico que va a proporcionar en detectar nuevas resonancias a través de asimetrías de carga.

Introduction

The CERN Large Hadron Collider (LHC) has started working and performing collisions. There are great expectations for the LHC data: its 14 TeV centre–of–mass energy at full regime will lead us into the TeV scale physics, where we hope to find answers to some of the unrevealed mysteries of Nature. The LHC has already produced the highest energy ever reached on the Earth with collisions at 7 TeV of center-of-mass energy on the 30th of March 2010. Throughout the next years the energy will be raised until 14 TeV.

In the early '70 the Standard Model (SM) of elementary interactions is ultimated and in the following decades it turns out to explain with great precision a lot of experimental data. Also, predicted particles (Z and W bosons, top quark ...) are discovered and the composition of Nature in terms of particles is better and better understood. The Standard Model is a gauge theory based on the symmetry group $SU(3)_C \otimes SU(2)_L \otimes U(1)_Y$. It describes three of the fundamental forces present in Nature: the strong, the weak and the electromagnetic force. The fourth one is gravity which so far has not been incorporated. The elementary particles in the SM are classified as leptons and quarks, which are fermions, and gauge bosons, which are responsible of the interactions. In Table 1 their properties are summarized.

	spin $= \frac{1}{2}$				**spin** $= 1$	
	Leptons		**Quarks**		**Gauge bosons**	
Generation		Q		Q		Force
I	e	-1	u	$2/3$	γ	e.m.
	ν_e	0	d	$-1/3$	g	strong
II	μ	-1	c	$2/3$	$W^\pm$	weak
	ν_μ	0	s	$-1/3$	Z	
III	τ	-1	t	$2/3$		
	ν_τ	0	b	$-1/3$		

Table 1: Particle content of the Standard Model.

Nevertheless, there are some questions still open: which is the origin of mass? Why are we made of matter instead of antimatter? What is this dark matter that makes up most of the matter in our universe and yet we cannot see? The LHC aims to find answers to these and more problems, in the next years.

The LHC is a proton–proton collider, composed by two rings of about 27 km of length. The beams cross in four points, where five experiments are located [1]. There are two high luminosity, multi-purpose detectors, ATLAS and CMS, and two low luminosity ones, TOTEM and LHCb, the first one devoted to the detection of protons at small angles and the second one to B-physics. Furthermore, an ion experiment, ALICE, is set up, and it will work with lead ion beams.

One of the main goals of ATLAS and CMS is to find the Higgs boson. The Higgs mechanism tells us that those particles which have a mass acquire it through the interaction with a scalar field, called Higgs boson. Many theories have been developed that include one or more Higgs bosons, also in supersymmetric scenarios. However, nobody has detected it so far. The current lower limit coming from direct searches is around 114 GeV at 95% confidence level. A global electroweak SM fit of the Large Electron-Positron collider (LEP) data indicates a preference for a light Higgs: an upper limit has been set to 182 GeV [2]. A general unitarity constraint gives an upper limit of 1.2 TeV [3], so the LHC will cover the whole range of energies where we expect to find the Higgs. Moreover, the high energy of the LHC will produce a sizable increase in the Higgs cross section compared to the Tevatron. Therefore, enough statistic will be in hand in order to find a definitive signal. Should this not happen, alternative models can be investigated. Especially in this case, testing models like supersymmetry (SUSY) is very important: in principle, sparticles with mass lower than few TeV are accessible to the experiments. Some of the SUSY models can explain also the discrepancy that we observe in the universe between matter and antimatter. Indeed, new sources of CP violation, different from the SM ones, can be found in SUSY, as well as in rare decays of B mesons. The puzzle of dark matter could also benefit from SUSY discoveries: indeed, the lightest supersymmetric particle is an optimal candidate for the dark matter. Another possible candidate could come from extra–dimensional models. In these models, more dimensions exist, curled up in such a way that they escape the common experience. ATLAS and CMS could detect this hidden dimensions, through Kaluza-Klein excitations of SM particles or even the graviton. This kind of models would be also a way of studying the quantum theory of gravity, which lives in a world with more than three dimensions [4].

Before the exciting discovery era starts, a period of detailed measurements of SM processes has to be passed. This is useful, not only to calibrate the detectors with already known processes, but also because we will be able to enter unprecedented scales and regions of the phase space. This will allow to set higher constraints on parton distribution functions (pdf), as well as checking the correct behaviour of the Monte Carlo generators in a wide range of scales. Finally, processes such as $W/Z+$ jets and top quark production are an important background to new physics processes and their contributions need to be known in detail [5].

The high luminosity of the two multi-purpose detectors has been necessary because

many of the SM processes have a low cross-section at the LHC. On the other hand, having a high number of particles colliding per second increases the probability of inelastic interactions and this is the reason why the beam is divided in bunches. The balance between these two requirements has lead to an interval between two beam crossings equal to 25 ns. The full regime planned luminosity is $\mathcal{L} = 10^{34}\text{cm}^{-2}\text{s}^{-1}$. The colliding partons inside the protons carry momentum fractions x_1 and x_2. The centre-of-mass energy of the single process is thus $\sqrt{\hat{s}} = \sqrt{x_1 x_2 s}$, where $\sqrt{s} = 14$ TeV at full regime. This means that the accessible energy is around a few TeV, thus it is possible in principle to detect particles with masses in such a range. The Tevatron, the proton–antiproton facility located at Fermilab, with its centre-of-mass energy of 1.96 TeV has already ruled out the existence of new resonances in several models with masses lower than 1 TeV.

While LEP collided electrons and positrons, the LHC is a proton-proton accelerator, which means that in every collision we have more than one initial state and consequently more than one fundamental interaction per bunch crossing [3]. This makes our knowledge of the physics processes that occur less precise, because the partons forming the proton can mix with the final states of the process. Since the beam particles are hadrons, the processes generated at the LHC are mainly ruled by Quantum Chromodynamics (QCD). The main problem of QCD is that the interaction strength is high (several orders of magnitudes more than the weak or the electromagnetic one), so perturbation theory has a limited range of application. The QCD coupling constant α_s runs in such a way that for high momentum transfers it is small, while it grows when the momentum transfer decreases. So, processes can be calculated perturbatively only at high momentum transfers, such as in the case of heavy particles production, while the hadronization has to be approached with non-perturbative techniques. As for perturbative analysis, a large number of processes is going to show up at the LHC, both of signal and background, especially short distance hadron emission. So, it is of crucial importance to know extremely well the background also, in order to be able to disentangle the possible signal of new physics from it. For these reasons, all of these processes need to be calculated in perturbative QCD.

My thesis aims to approach the challenge of the new LHC physics from two points of view. On one side, at the LHC, calculations beyond the tree level are needed in order to have a theoretical precision comparable with the precision of the experimental data. Indeed, in experiments such as ATLAS and CMS, statistical errors are very low. Other sources of errors, like the uncertainties on parton distribution functions (PDFs) and the luminosity, can be reduced significantly by taking the ratio of the observables of interest and some benchmark SM processes, such as Z, W and $t\bar{t}$ production [5]. So, at least next-to-leading order (NLO) calculations are indispensable. Next-to-next-to-leading order (NNLO) calculations exist for a few jets, while, beyond that order, there are only very few calculations (see, e.g., [6]). Calculations at orders higher than tree level are in general quite cumbersome, so new methods can be useful to develop them. Our aim is to simplify and compactify the expression of n-legs amplitudes at tree level, in order to extend them to one or more loops and make NLO and NNLO amplitudes simpler. We will discuss this part in Chapters 2 and 3.

On the other side, the exciting possibility of discovering new particles in the TeV region

makes an understanding of the resolution that can be reached mandatory. In Chapter 5 and 6 we examine the possibility of detecting new resonances at high energy colliders, that decay to a top–antitop quark pair. Indeed, there are several models of new physics that introduce massive particles, like axigluons, Kaluza–Klein gluons, colorons. Some of them, when decay to a quark–antiquark pair, produce a charge asymmetry, already at tree level. In this work we explore the possibility of measuring this kind of asymmetries at hadronic colliders. We focused especially on the LHC scenario, in order to work out the statistical reach that it provides in detecting new resonances through charge asymmetries.

Chapter 1

Quantum Chromodynamics

1.1 The running coupling constant

Quantum Chromodynamics (QCD) is the theory which describes the strong interaction, the force responsible of keeping together the nucleus components, that acts on quarks and gluons. QCD is a gauge theory based on the $SU(3)_C$ symmetry group. The group charge is called colour. QCD has two peculiar characteristics: confinement and asymptotic freedom. As its very name suggests, this interaction appears strong since free quarks and gluon are not observed, but only the hadrons that are constituted by them. The hadrons that we observe are neutral in color (that is, they are color-singlet). This property is called confinement and, although it has not been demonstrated yet, it relies on strong evidences and a demonstration of it has been addressed by lattice calculations. On the other side, quarks and gluon behave as free particles when tested at short distances. This feature, known as asymptotic freedom, is due to the running of the color coupling constant α_s that is small at high energies and grows as the energy decreases. The running behaviour of the coupling constant is a consequence of renormalization. When adding quantum corrections to the tree level, infinite quantities are generated that would make the predictions useless. To solve this problem, first the divergent part in every diagram is isolated, in a process called regularization. The price that has to be paid for this is the introduction of a new unphysical scale in the calculation. Then, through a redefinition of the fields that take part in the theory, the new scale dependence is found to disappear with the infinite terms, leaving a finite, well defined prediction. During this procedure the coupling constant appears to be "running", i.e. it depends on the energy scale of the process we are calculating. The differential equation that regulates the α_s dependence on the scale, at one loop level, is [7]:

$$\mu \frac{\partial \alpha(\mu)}{\partial \mu} = \beta_0 \frac{\alpha^2}{\pi}\,, \tag{1.1}$$

where

$$\beta_0 = \frac{2\,N_f - 11\,N_c}{6}\,, \tag{1.2}$$

N_f is the number of quark families and $N_c = 3$ is the number of colours. Integrating Eq. (1.1) between two values Q_0^2 and Q^2, one finds the value of α_s for every Q^2, knowing its value for a fixed Q_0^2:

$$\alpha_s(Q^2) = \frac{\alpha_s(Q_0^2)}{1 - \beta_0 \frac{\alpha_s(Q_0^2)}{2\pi} \ln(Q^2/Q_0^2)} \tag{1.3}$$

From (1.2) it is clear that for $N_f < 16$, the beta function is negative. The negative contribution is introduced by the gluon self-interaction, typical of non-abelian theories. If β_0 is negative, for $Q^2 > Q_0^2$, $\alpha_s(Q^2) < \alpha_s(Q_0^2)$ and the coupling constant becomes smaller and smaller with the raising of the energy. It is also possible an alternative approach that introduces a dimensional scale that gives an estimation of the perturbative domain. Eq. (1.1) can be solved between Q^2 and the infinity, finding:

$$\alpha_s(Q^2) = \frac{1}{\beta_0 \ln(Q^2/\Lambda_{\rm QCD}^2)}\,, \tag{1.4}$$

where $\Lambda_{\rm QCD}$ is the scale where the coupling diverges, extrapolated from the perturbative regime. It is measured to be $\Lambda_{\rm QCD} \simeq 200$ MeV. Actually, expression (1.4) is calculated in perturbation theory, so it is not reliable outside this regime. Anyway, it is sensible to expect α_s to keep on growing when the energy decreases, until the perturbation development is not possible anymore. So, $\Lambda_{\rm QCD}$ can be regarded qualitatively as the magnitude where the interaction becomes strong. Nevertheless, from a rigorous point of view, we can state that it is the scale parameter of the theory which rules the behaviour of α_s at high energies [8].

The QCD Lagrangian reads:

$$\mathcal{L}_{\rm QCD} \equiv -\frac{1}{4} G_a^{\mu\nu} G^a_{\mu\nu} + \bar{\psi}\,(i\gamma^\mu D_\mu - m_f)\,\psi + \mathcal{L}_{\rm g.f.} + \mathcal{L}_{\rm ghosts}\,, \tag{1.5}$$

where

$$\begin{aligned} D_\mu &= \partial_\mu - i g_s G^a_\mu T_a \\ G^a_{\mu\nu} &= \partial_\mu G^a_\nu - \partial_\nu G^a_\mu + g_s f^{abc} G^b_\mu G^c_\nu\,. \end{aligned} \tag{1.6}$$

The T^a are the generators of the $SU(3)_C$ group. We recall that in the symmetry group $SU(N)$ there are $N^2 - 1$ generators, that, in the fundamental representation of the group[1], are traceless hermitian $N \times N$ matrices T^a_{ij} with $i, j = 1, \ldots, N$ and $a = 1, \ldots, N^2 - 1$. The totally antisymmetric structure constants f^{abc} are defined as:

$$[T^a, T^b] = i f^{abc} T_c\,. \tag{1.7}$$

The quark fields ψ are summed over the three different flavours and colours. G^a_μ is the gluon field and g_s is the strong coupling constant such that $\alpha_s \equiv g_s^2/(4\pi)$. $\mathcal{L}_{\rm g.f.}$ is the

[1]The fundamental representation of $SU(N)$ is the one with dimension N.

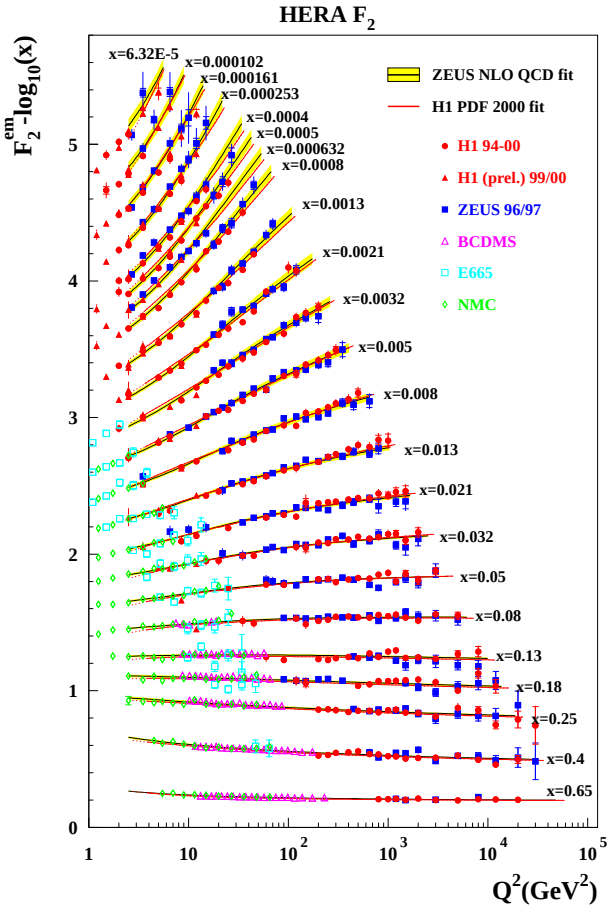

Figure 1.1: Proton structure function F_2 versus Q^2 in the range of $1 - 10^5$ GeV^2 for fixed values of x in the range of $0.65 - 6 \times 10^{-5}$ [11].

gauge fixing term and $\mathcal{L}_{\text{ghosts}}$ is the Faddeev Popov Lagrangian, that guarantees the correct polarization for the gauge boson. Analogously to Eq. (1.7), a totally symmetric tensor d_{abc} can be introduced, such that the anticommutator can be written as:

$$\{T^a, T^b\} = \frac{1}{N}\delta_{ab} + d^{abc}T^c\,. \tag{1.8}$$

At low energies, where perturbative expansion ceases being valid, the efforts of describing QCD have generated different paths such as lattice calculations, effective Lagrangians, (chiral Lagrangian, heavy quark effective theories, Soft Collinear Effective Theories (SCET), Non Relativistic QCD....) and QCD sum rules. However, the scope where QCD can be tested through the current experiments is the perturbative regime. Important steps forward have been made at the electron-proton collider HERA, especially concerning parton distribution functions and proton structure (see, for instance, Fig. 1.1) and at the Tevatron (proton-antiproton collider), where the top quark has been discovered. The

measurements of the coupling constant α_s are among the most compelling evidences of the correctness of QCD. They come mainly by LEP and by scaling violation measurements in deep inelastic scattering at hadron colliders. The agreement among such different kinds of experiments is really amazing, as it is shown in Fig. 1.2. The most recent world average gives $\alpha_s(m_Z^2) = 0.1184 \pm 0.0007$ [12].

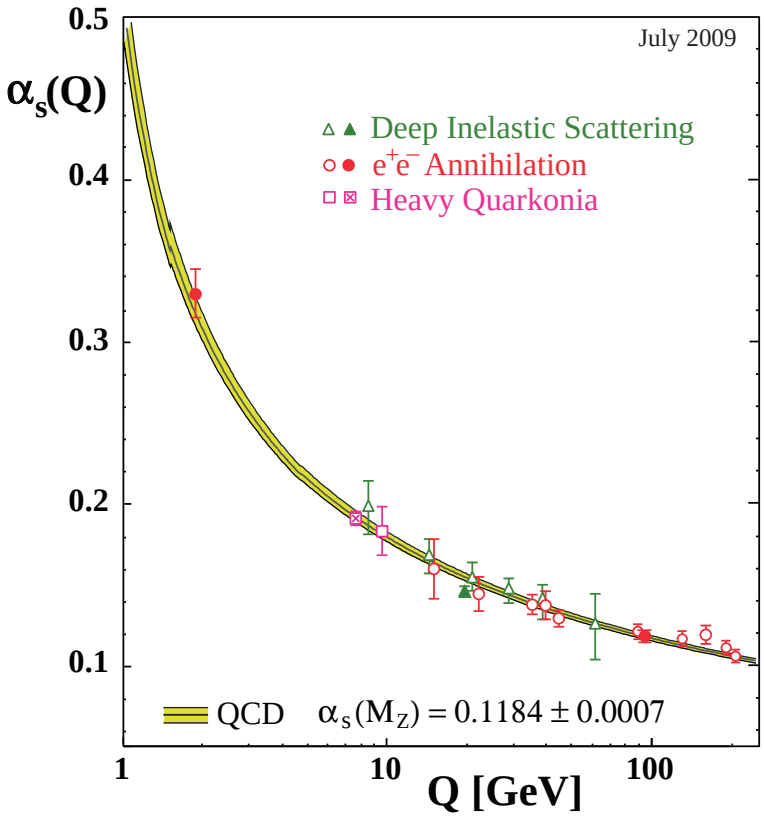

Figure 1.2: Summary of measurements of α_s as a function of the energy scale Q [12].

1.2 Jets

Quarks and gluons are not observed as free particles. Still, it is possible to have clear evidence of them, through the observation of jets. Indeed, a parton emits with high probability soft radiation, i. e. gluons or quarks that move roughly in the same direction or with low energy. That means that what one can observe is a flow of energy and momentum in a particular direction, called jet.

When jets were first observed at LEP in 1975 [9], it was an unequivocal proof of the existence of quarks and gluons. At LEP, an electron and a positron annihilated, producing a back-to-back quark antiquark pair, through a virtual photon or Z. The two-jet signal

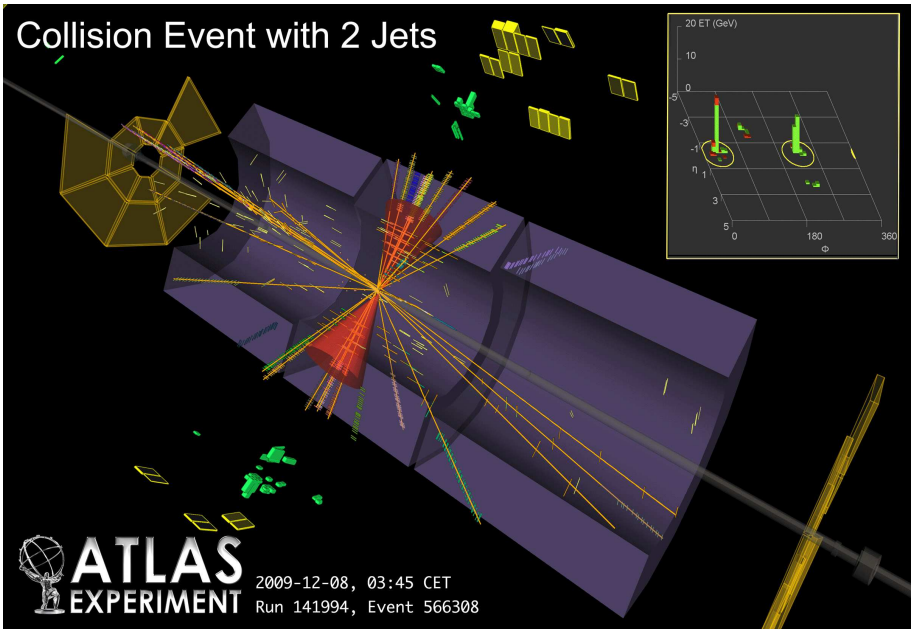

Figure 1.3: First 900 GeV collision events with two jets in stable-beam conditions at ATLAS, December 6, 2009.

reflects exactly this event, where each parton of the pair emits soft radiation. If hard radiation is emitted (with a probability of around 10%), the new parton in turn will origin a third jet. This led to the three-jet observations. QCD can predict very well the details of such events, like the amount of different numbers of jets or the variation depending on the energy. In this way, quantitative tests of QCD have been done that have proved the correctness of the theory to a great extent [10].

At the LHC, the dominant process among the ones with large transverse momentum will be the inclusive dijet production (2 jets + X). At tree level, it is originated by a 2 parton $\rightarrow$ 2 parton event and the signal will be a number of more or less energetic jets coming from the fragmentation of the partons in the final state. It appears clear that identifying jets is not an easy task. An amount of hadronic energy and momentum has to be connected to a single original particle and this is not unambiguous: different algorithms can be built that define which signals found in the detector belongs to one jet and which to another one. While in e^+e^- collisions one has the advantage of a unique initial state, in hadron collisions problems arise in order to identify jets, due to the compositeness of the initial states [14]. Only one parton takes part in the interaction out of the many that constitute the hadron. This means that in the final states a lot of events appear besides the jets, originated by soft radiation from the other partons. Moreover, the parton involved in the interaction can produce initial state brehmsstrahlung, making the final state more and more complicated. All these events are called "beam jets", because they have usually small transverse momentum with respect to the beam axis and a large parallel momentum.

So, one of the requirements of a jet reconstruction algorithm in hadron collisions is to disregard the events with low transverse momentum, in order to eliminate beam jets as much as possible. From a theoretical point of view, a good jet algorithm for hadron collisions should fulfill some more requirements [15]. It should be infrared and collinear safe, that is the same number of jets must be found if a collinear or a soft parton is added, given the same energy. It should be invariant for boosts along the beam axis, since the laboratory frame and the center-of-mass frame of the interaction partons are connected by a boost. Finally, it should be order independent, namely the same result is given if the analysis is applied at parton or detector level.

A jet algorithm is formed by two basic pieces: a test variable and a recombination procedure. The values taken by the variable are used to decide whether two final hadrons belong to the same particular jet or not and the recombination prescription combines the particles in different jets. In hadron collisions a cone definition has often been used [16]. In this kind of algorithms, a jet is a set of particles whose momenta lie in a same angular cone with radius R. Usually, one starts looking at points in the detectors with a high amount of energy and draws a cone with radius R; then, one calculates the centroid of the cone, weighted on the transverse energy of the particles enclosed and draw a new cone around that. One continues until a stability is reached and a jet is thus defined. The procedure is iterated until all the particles with high transverse energy are placed in a jet. The last step is to take care of overlapping jets, either by merging or by splitting them. Cone algorithms have the bad characteristic of being not collinear neither infrared safe, due to the presence of lower bounds on energy. Anyway, a seedless infrared-safe cone method has been recently proposed [17].

The other fundamental class of algorithms is the so called clustering algorithms. They are infrared and collinear safe and no merging neither splitting is needed, since every particle is assigned uniquely to a jet. These algorithms combine together particles that are close each other or that have high p_T. Let us describe more in detail the so called k_T algorithm as an example [15]. In this algorithm a variable is built, that basically represents the relative transverse momentum between two particles i and j:

$$d_{ij} \equiv \min(k_{Ti}^2, k_{Tj}^2) \frac{(y_i - y_j)^2 + (\phi_i - \phi_j)^2}{R^2}\,, \tag{1.9}$$

where y_i is the rapidity of the i particle, ϕ_i is the angle of the momentum of the i particle in the plane perpendicular to the beam axis and R is a parameter characteristic of the algorithm that plays the same role as the cone radius in the cone algorithm. Usually its value is around $\mathcal{O}(1)$. We also remember that k_T is the component of the momentum perpendicular to the beam axis. One has to calculate d_{ij} and $d_{iB} \equiv k_{Ti}^2$ for every pair of objects (particles or pseudo-particle) and find the smallest one. If d_{ij} is the smallest, particles i and j are recombined, that is, a pseudo-particle is added to the particle list and both i and j are removed, otherwise particle i is called a jet and removed from the particle list. This procedure is repeated iteratively until no particles are left in the list. A generalization of the k_T algorithm is the so called anti-k_T [18], where the variables at stake

are:

$$d_{ij} \equiv \min(k_{Ti}^{-2}, k_{Tj}^{-2}) \frac{(y_i - y_j)^2 + (\phi_i - \phi_j)^2}{R^2} \tag{1.10}$$

and $d_{iB} \equiv k_{Ti}^{-2}$.

Chapter 2

N-gluon amplitudes

2.1 Introduction

The calculation of cross sections in gauge theories has been developed for many years by means of Feynman rules in perturbation theory, leading to theoretical predictions in a very good agreement with the experimental results. These calculations are at a fixed order in the coupling constant α_s, which depends on the renormalization scale. Since this dependence is canceled only across different orders of α_s, an error in the truncated serie is produced. Of course, the higher the order, the better the precision one has: we need to go beyond the tree level to reach enough accuracy. NLO and NNLO calculations are required to reduce the error in the scale dependence. In QCD, in the last years, great progresses in NNLO calculations have been made for a number of observables such as totally inclusive quantities (e.g. the $e^+e^- \to$ hadrons total cross–section [19]) or splitting functions [20]. Quite a number of processes have been calculated at NLO, but they are generally limited to four jets. Two of the most recent calculations are, for instance, $q\bar{q} \to t\bar{t}b\bar{b}$ [21] and $W \to 3$ jets [22]. Indeed, complexity increases rapidly with the number of external legs, because the number of the diagrams needed to calculate these processes increases factorially as it is shown in Table 2.1. Every diagram leads to very complicated expressions, due to the presence of non–Abelian couplings and the number of kinematic variables (three more for every external leg) makes all more and more cumbersome.

n	2	3	4	5	6	7	8
# of diagrams	4	25	220	2485	34300	559405	10525900

Table 2.1: The number of Feynman diagrams contributing to the scattering process $gg \to n\ g$ [23].

The intermediate calculations are often quite difficult, while in the final result many terms cancel. For this reason, effort has been made to find methods that make the cal-

culations more efficient. Indeed, unnecessary spurious singularities can arise that make numerical evaluations unstable: compact results can avoid this problem. Compact expressions can also be useful in comparing different results and in understanding how to organize calculations in order to extend the result to an arbitrary number of external legs and to higher orders.

Approaches alternative to Feynman diagrams to calculate n–parton scattering amplitudes have been developed since the 80's. The basic idea is to use all the information supplied by the external particles (color and helicity) in order to decompose the amplitudes in simpler, fundamental pieces. Color decomposition allows to separate the color contribution to the amplitude from the Dirac part, thus obtaining the total amplitude as the sum of sub–amplitudes that have the useful property of being color–ordered. The spinor helicity formalism deals with spinor products, introducing spinorial representations for massless gauge bosons and produces very compact results.

In our work, we have used both these approaches, combining them with recursion relations, to address the calculation of QCD massive amplitudes with a generic number of external legs.

2.2 Recursion relations so far

In the second half of the 80's, a number of people started to organize QCD amplitudes by their color structure [24–27]. They addressed both processes with only gluons legs and with quark–antiquark pairs, calculating numerically a few of these for small values of n. Gluon amplitudes at tree level with all gluons of positive helicity or one single negative helicity vanish:

$$A(1^{\pm}, 2^{+}, ..., n^{+}) = 0\,. \tag{2.1}$$

Then, it is expected that the successive amplitude, with two gluons of negative helicity, can be written in a very compact form. In 1986 Parke and Taylor conjectured an expression for the Maximally Helicity Violating (MHV) squared amplitude at tree level [28]:

$$|\mathcal{M}(1^{-}, 2^{-}, 3^{+}, 4^{+}, 5^{+}, \ldots, n^{+})|^2 \propto \sum_{P} \frac{(1\cdot 2)^4}{(1\cdot 2)(2\cdot 3)\cdots(n\cdot 1)} \tag{2.2}$$

at the order $\mathcal{O}(N_c^{-2}) + \mathcal{O}(g^2)$, where N_c is the number of colors and $(i \cdot j)$ indicates the scalar product of p_i and p_j. The sum is performed over all the non cyclic permutations of $1, \ldots, n$. One year after, Berends and Giele [29] proved the conjecture (2.2) that reads, in terms of the partial amplitude:

$$A_n(1^{+}, \ldots, i^{-}, \ldots, j^{-}, \ldots, n^{+}) = \frac{\langle ij\rangle^4}{\langle 12\rangle\langle 23\rangle\cdots\langle n1\rangle}\,, \tag{2.3}$$

where with $\langle ij\rangle$ we indicate the spinorial product of right–handed spinors

$$\langle ij\rangle = \overline{u_{-}(k_i)}u_{+}(k_j)\,, \tag{2.4}$$

according with the notation that is reported in section 2.4. They built a number of recursion relations for color–ordered partons amplitudes that allow to construct the n–parton amplitude once the $n-1$ amplitude is known. They started with pure–gluon amplitudes that are fundamental in hadron processes since gluons carry the largest cross section and luminosity. From these amplitudes, it is relatively simple to add pairs of fermion–antifermion and vector bosons. The construction of these recursion relations is based on the use of off–shell currents, that is scattering amplitudes with one off-shell leg. To find the on–shell amplitude for n particles one just needs to attach the nth parton to this current. The usefulness of this procedure is double. First, the $n+1$ process can be worked out using the result for n. Moreover, the $n-1$ parton current already involves all the Feynman diagrams, thus eliminating the need to calculate them. Pure gluonic amplitudes can be determined one by one starting with $n = 3$, but for specific helicity configurations their shape is found to be very simple. Expressions valid for an arbitrary number of partons can be guessed and then verified to satisfy the recursion relations. In this way, very compact results have been found. Besides the form of specific amplitudes such as MHV, more conjectures concerning factorizations, symmetries and many other properties can be proven with the tool of the recursion relations. Recursion relations have also been proved very useful for one-loop calculations, combined with the unitarity method [30].

To investigate the hidden structure of a result as simple as the one seen in Eq. (2.3), Witten transformed it into the "twistor" space in 2003 [31]. The first to suggest the use of twistors was Penrose [32], while trying to find a connection between Einstein theory of gravitation and quantum mechanics. The consideration that probably at very small distances the usual space–time structure would not be the correct description, motivated him to look for alternatives. The interest for twistors arises because spinors seem to be more fundamental than four–vectors in Minkowski space. The transformation into twistors space [33] is a type of Fourier transform. It leaves the right–handed spinors $u_+(p)$ unchanged and it transforms the left–handed spinors $u_-(p)$ into their Fourier conjugate μ, defined as:

$$u_-(p)_\alpha = i\frac{\partial}{\partial \mu^\alpha}. \tag{2.5}$$

Relationship (2.5) is completely analogous to the usual Fourier transform between space–time coordinates and momenta ($p = i\frac{\partial}{\partial x}$). Let us use a different spinorial notation, that makes things clearer, in order to look at how the amplitudes are transformed by this change. Calling:

$$(\lambda_i)_\alpha \equiv u_+(p_i)_\alpha, \qquad (\tilde{\lambda_i})_\alpha \equiv u_-(p_i)_\alpha\,, \tag{2.6}$$

we obtain:

$$A(\lambda_i, \tilde{\lambda}_i) \longrightarrow A(\lambda_i, \mu_i) = \int \prod_{i=1}^{n} d\tilde{\lambda}_i e^{i\mu_i \tilde{\lambda}_i} A(\lambda_i, \tilde{\lambda}_i)\,. \tag{2.7}$$

The transformation of an MHV amplitude is very simple, because it depends explicitly only on the holomorphic $\langle ij\rangle$ spinorial products, while the $\tilde{\lambda}_i$ dependence is hidden in an

overall δ–function over the momenta. This factor can be written as:

$$\delta^4(\sum_i^n p_i) = \int d^4x \, \exp[\, i(\sum_i^n p_i) \cdot x] = \int d^4x \, \exp\Big[i \sum_{i=1}^n (\lambda_i)_\alpha x^{\alpha\beta} (\tilde{\lambda}_i)_\beta\Big] \,, \tag{2.8}$$

where we have used the Gordon identity [1] for p_i, remembering that

$$x_{\alpha\beta} \equiv \gamma^\mu_{\alpha\beta} x_\mu \,. \tag{2.9}$$

Therefore, the transformed MHV amplitude is:

$$\begin{aligned} A_n^{\rm MHV}(\lambda_i, \mu_i) &= \int \prod_{i=1}^n d\tilde{\lambda}_i \exp[i\mu_i \tilde{\lambda}_i] \int d^4x \; A_n^{\rm MHV}(\lambda_i, \tilde{\lambda}_i) \exp[i \sum_{i=1}^n \lambda_i x \tilde{\lambda}_i] \\ &= \int d^4x \; A_n^{\rm MHV}(\lambda_i, \tilde{\lambda}_i) \int \prod_{i=1}^n d\tilde{\lambda}_i \exp[i(\mu_i + x\lambda_i)\tilde{\lambda}_i] \\ &= A_n^{\rm MHV}(\lambda_i, \tilde{\lambda}_i) \int d^4x \prod_{i=1}^n \delta(\mu_i + x\lambda_i) \,. \end{aligned} \tag{2.10}$$

This equation shows that an MHV amplitude is supported by a line in twistor space. In Fig. 2.1 (a) this is shown graphically.

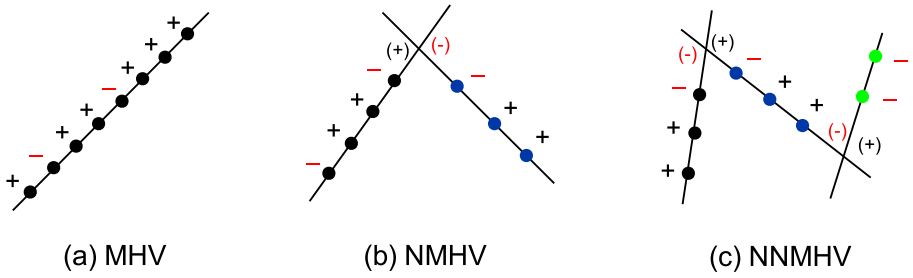

Figure 2.1: Tree amplitudes for n–gluon in twistor space: (a) MHV, (b) NMHV, (c) NNMHV [33].

Transforming next–to–maximally violating amplitudes (NMHV) and the following to twistor space is not that simple. Amplitudes with three or more negative gluons have been calculated and they are very complicated. Therefore, it is easier to guess which kind of curve $C(\lambda_i, \mu_i)$ supports the transformed amplitude and to pull it back to the original spinor space. Since $\mu_i = \partial/\partial\tilde{\lambda}_i$, $C(\lambda_i, \mu_i)$ becomes a differential operator and we only need to apply it on the unchanged amplitude and verify if it gives zero. Such a method has been applied to amplitudes with three or more negative helicity gluons. In NMHV amplitudes the support is an intersection of two lines (2.1 (b)), while NNMHV is the intersection of three lines (2.1 (c)). The number of lines is in general one less than the number of

[1] $[i|\gamma^\mu|i\rangle = \langle i|\gamma^\mu|i] = 2k_i^\mu$

negative helicity gluons. Thus, we see that the twistor space unveils a beautiful feature of the amplitude that, as often happens in physics, allows us to guess that an important, fundamental structure is still to be discovered. Unfortunately, it turns out that it is not going to help in calculating numerically the amplitude.

This purpose has been achieved by Cachazo, Svrcek and Witten himself [34] that found an alternative method to Feynman rules that allows to calculate these amplitudes and at the same time clarifies the results in twistor space shown in Fig. 2.1. They found that the tree level amplitudes with any number of negative helicity external gluons can be written in terms of MHV amplitudes.

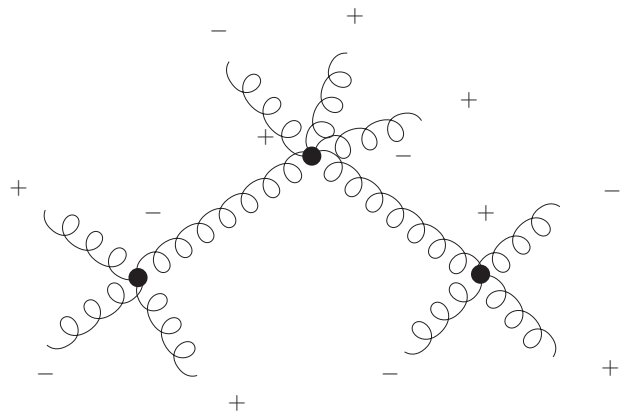

Figure 2.2: Example of CSW construction for an amplitude with four negative helicity gluons.

In Fig. 2.2 the four negative gluons example is shown. As an implication of this result, it follows that amplitudes with no negative gluons or only one must vanish, since otherwise there would not be vertices at all. This statement has been proven with arguments from supersymmetry.

One loop amplitudes are more complicated in QCD as well as in twistor space [35, 36]. Anyway, it was found that supersymmetric QCD with $\mathcal{N} = 4$ has a simpler structure. In this theory, bubble and triangle diagrams vanish and only scalar box diagrams need to be calculated. The integrals are well known and the coefficients enclose the infrared behaviour that is strictly connected with tree level contribution of the amplitudes that are being calculated. Thus, infrared relationships allow us to find new representations of the tree level amplitudes. This is exactly what Britto, Cachazo, Feng and Witten used to prove BCFW recursion relations [37]. The idea behind these relations is to use the known behaviour of the amplitude in its poles to construct the amplitude itself. The tool used is complex analysis with its richness of theorems and properties to be exploited. The amplitude can be seen as depending on a complex variable z and the desired object is

simply this amplitude evaluated at $z = 0$. By the residue theorem, the latter is connected to the sum of the residues of the function in its poles. Since an amplitude is a rational function of spinorial products, singularities arise as multiparticle poles, that is when a propagator goes on–shell and the residue becomes the splitting of the function in a left and a right amplitude with respect to the propagator. Each of these amplitudes has less legs than the original. For a detailed explanation of BCFW recursion relations, see Appendix A. These types of recursion relations, unlike the currents recursion relations of Berends and Giele, deal with on–shell amplitudes, that is all their external legs are physical, since the propagator itself goes on–shell in the pole. BCFW have been shown also to be very useful if applied to massive scalars by Badger, Glover, Khoze and Svrček [38] (BGKS relations) and to fermions and vector bosons [39]. In the last years, efforts have been made to include scalar bosons in the multiparticle amplitudes [40–43], due to the prospect of finding the Higgs particle in the LHC, finding out both numerical and analytical calculations.

2.3 Color ordering

Let us now describe the color decomposition of the amplitudes, which is the first step to obtain simpler expressions for multiparton processes. The group symmetry of QCD is $SU(3)$, but we will generalize our analysis to $SU(N)$. For the purpose of this chapter, we choose the generators of $SU(N)$ with the following normalization:

$$\mathrm{Tr}(T^a T^b) = \delta^{ab} \tag{2.11}$$

so that the structure constants f^{abc} now satisfy the following relationship:

$$\left[T^a, T^b\right] = i\sqrt{2} f^{abc} T^c \,. \tag{2.12}$$

In QCD, we have three kinds of vertices involving gluons: quark–quark–gluon, three gluons and four gluons, as can be seen in Fig. 2.3. We see that, in the first vertex, T^a matrices are present with color indices contracted with the fermions ones, while in the gluons–only vertices there are the f^{abc} constants and the contractions $f^{abe} f^{cde}$. We want to express all in terms of the group generators to make the color structure evident, thus we use:

$$f^{abc} = -\frac{i}{\sqrt{2}} \mathrm{Tr}(T^a [T^b, T^c]) = -\frac{i}{\sqrt{2}} \left(\mathrm{Tr}(T^a T^b T^c) - \mathrm{Tr}(T^a T^c T^b) \right) \tag{2.13}$$

that follows from (2.11) and (2.12). For the fundamental representation of $SU(N)$ we have the following relationship that allows us to reduce the number of T^a matrices:

$$(T^a)_{i_1}^{\ j_1} (T^a)_{i_2}^{\ j_2} = \delta_{i_1}^{\ j_2} \delta_{i_2}^{\ j_1} - \frac{1}{N} \delta_{i_1}^{\ j_1} \delta_{i_2}^{\ j_2} \,. \tag{2.14}$$

Managing these transformations, every n–gluon amplitude $\mathcal{A}_n^{\mathrm{tree}}$ at tree–level can be decomposed in the sum of traces of T^a matrices times a Dirac amplitude:

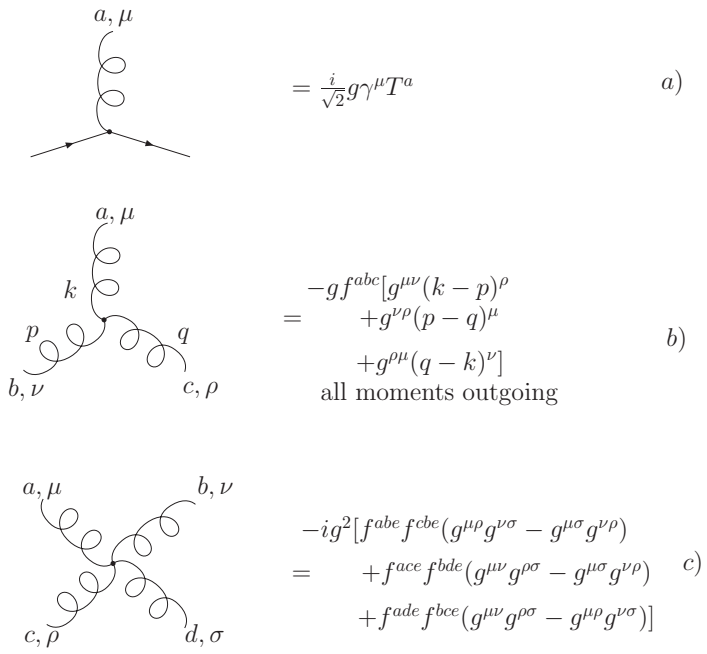

Figure 2.3: Feynman rules for QCD.

$$\mathcal{A}_n^{\text{tree}}(gg\dots g) = \sum_{\text{perm}} \text{Tr}(T^{a_{\sigma_1}} \cdots T^{a_{\sigma_n}}) A_n^{\text{tree}}(\sigma(1^{\lambda_1}), \dots, \sigma(n^{\lambda_n})) \tag{2.15}$$

where the sum is made over all the permutations of the a_i indices modulo cyclic permutations (they preserve the trace); λ_i is the helicity of the ith particle and A_n^{tree} is a Dirac amplitude that contains all the kinematic information but not the color. These new amplitudes can be calculated with color–ordered Feynman rules that do not contain f^{abc} nor T^a anymore, that are shown in Fig. 2.4. The first and the second one simply arise from removing respectively the T^a and the f^{abc} factor that originates the trace. The third one is due to the separation of the 4–gluon vertex in terms carrying each one a pair of structure constants, i.e. the sum of $\text{Tr}(T^a T^b T^c T^d)$. Rearranging the traces and grouping the cyclically identical terms, all the terms have the form:

$$\text{Tr}(T^a T^b T^c T^d) \left(g^{\mu\nu} g^{\rho\sigma} - \frac{1}{2}(g^{\mu\sigma} g^{\nu\rho} + g^{\mu\nu} g^{\rho\sigma}) \right) . \tag{2.16}$$

Each of them represents a four gluon vertex with a particular order of color indices and momenta and Feynman rule:

$$g^{\mu\nu} g^{\rho\sigma} - \frac{1}{2}(g^{\mu\sigma} g^{\nu\rho} + g^{\mu\nu} g^{\rho\sigma}) . \tag{2.17}$$

This clarifies also why in (2.15) the sum is over the permutation of a_i indices, since each of them is strictly connected with a particular momentum ordering.

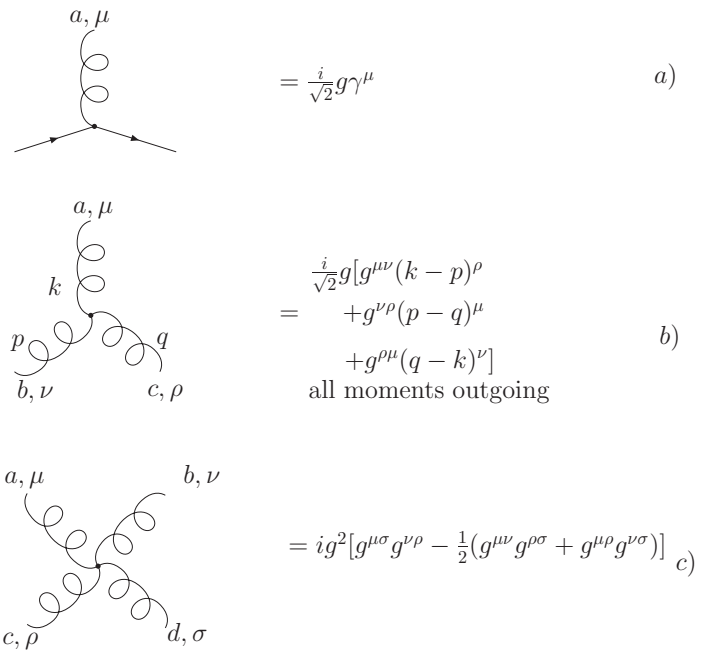

Figure 2.4: Color ordered Feynman rules.

The following relationship holds [23], where $\{a\}$ and $\{b\}$ are two permutations of the gluon color indices:

$$\sum_{a(b)_{\sigma_i}=1}^{N^2-1} \mathrm{Tr}(T^{a_{\sigma_1}} \cdots T^{a_{\sigma_n}}) \left[\mathrm{Tr}(T^{b_{\sigma_1}} \cdots T^{b_{\sigma_n}})\right]^* = N^{n-2}(N^2-1)(\ \delta_{\{a\}\{b\}} + \mathcal{O}(N^{-2})\ ) \quad (2.18)$$

so that the color structures in equation (2.15) are orthogonal at the leading order in the N expansion. This means that the whole squared amplitude is the incoherent sum of the single partial amplitudes:

$$\sum_{\text{colors}} \mathcal{A}_n^{\text{tree}\,*} \mathcal{A}_n^{\text{tree}} = N^{n-2}(N^2-1) \sum_{\text{perm}} \{|A^{\text{tree}}(1,2,\ldots,n)|^2 + \mathcal{O}(N^{-2})\}\,. \quad (2.19)$$

If the amplitude presents a pair of external quarks, like in Fig. 2.5, the color ordering leads to the following expression:

$$\mathcal{A}_n^{\text{tree}}(q\bar{q}gg\ldots g) = \sum_{\text{perm}} T^{a_{\sigma_3}} \cdots T^{a_{\sigma_n}} A_n^{\text{tree}}(1_{\bar{q}}^{\lambda_1}, 2_q^{\lambda_2}, \sigma(3^{\lambda_3}), \ldots, \sigma(n^{\lambda_n}))\,. \quad (2.20)$$

In summary, the color–ordered amplitudes are simpler than the usual ones, because only a certain order of momenta appears, therefore the poles or the branch cuts (if we have loops) can involve only certain invariants. For instance, in a five gluon amplitude we can have poles only in s_{ij} with $j = i+1$, obviously modulo 5.

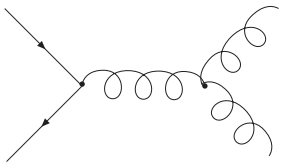

Figure 2.5: $q\bar{q}gg$ scattering.

2.4 Spinor helicity formalism

The spinor helicity formalism is a useful way to calculate amplitudes, because it makes possible to automatize the calculations and to find compact expressions in which the collinear limit of the amplitudes becomes evident.

In this approach amplitudes are calculated with the external particles having an assigned helicity [23]. To obtain the total cross section we have only to sum the squares of all the possible helicity amplitudes, because they do not interfere. With a fixed helicity it is possible to choose a parametrization for polarization vectors, using gauge invariance, that is useful to simplify the calculation. This formalism deals with massless fermions and gauge bosons. In the massless limit, the Dirac equation for positive and negative energy solutions is the same:

$$\begin{aligned} \not{k} u(k) &= 0, \\ \not{k} v(k) &= 0, \end{aligned} \tag{2.21}$$

and the chirality projector $(1 \pm \gamma_5)/2$ is the same as the helicity projector for $u(k)$, while it gets a minus sign for $v(k)$. Definite helicity solutions are:

$$u(k)_\pm = \frac{1 \pm \gamma_5}{2} u(k) \qquad v(k)_\pm = \frac{1 \mp \gamma_5}{2} v(k), \tag{2.22}$$

therefore it is possible to choose $u(k)_\pm = v(k)_\mp$.

Let us define the unit blocks of this formalism. The spinors are:

$$\begin{aligned} |i\rangle \equiv |k_i\rangle \equiv u_+(k_i) = v_-(k_i), \qquad & \langle i| \equiv \langle k_i| \equiv \overline{u_-(k_i)} = \overline{v_+(k_i)} \\ |i] \equiv |k_i] \equiv u_-(k_i) = v_+(k_i), \qquad & [i| \equiv [k_i| \equiv \overline{u_+(k_i)} = \overline{v_-(k_i)}\,. \end{aligned} \tag{2.23}$$

Thus, the spinor products are:

$$\langle ij \rangle = \overline{u_-(k_i)} u_+(k_j), \qquad [ij] = \overline{u_+(k_i)} u_-(k_j). \tag{2.24}$$

From (2.24) we see that

$$\langle ij \rangle^* = -[ij], \tag{2.25}$$

therefore the two quantities only differ by a complex phase.

It is possible to use spinors to construct a representation of the polarization vectors of massless gauge bosons of definite helicity, too:

$$\varepsilon_\mu^+(k;q) = \frac{\langle q|\gamma_\mu|k]}{\sqrt{2}\langle qk\rangle} \quad , \quad \varepsilon_\mu^-(k;q) = -\frac{[q|\gamma_\mu|k\rangle}{\sqrt{2}[qk]}. \tag{2.26}$$

Here k is the boson's momentum and q is an arbitrary reference momentum, whose choice reflects the gauge freedom. We can see that the expression (2.26) really satisfies the massless gauge bosons properties. It has transverse polarization:

$$\varepsilon^\pm(k;q)\cdot k = 0\,, \tag{2.27}$$

because $\not{k}|k^\pm\rangle = 0$ and it does create states with helicity ± 1. The normalization of these vectors is the usual one:

$$(\varepsilon^r)^*\cdot\varepsilon^{r'} = -\delta^{rr'}\,, \tag{2.28}$$

where $r, r' = +, -$. The choice of the reference momentum is really arbitrary, because the difference between two polarization vectors with different q is a longitudinal object that does not contribute to the dynamics:

$$\begin{aligned}\varepsilon_\mu^+(\tilde{q}) - \varepsilon_\mu^+(q) &= \frac{\langle\tilde{q}|\gamma_\mu|k]}{\sqrt{2}\langle\tilde{q}k\rangle} - \frac{\langle q|\gamma_\mu|k]}{\sqrt{2}\langle qk\rangle} = \frac{\langle qk\rangle\langle\tilde{q}|\gamma_\mu|k] - \langle\tilde{q}k\rangle\langle q|\gamma_\mu|k]}{\sqrt{2}\langle\tilde{q}k\rangle\langle qk\rangle} = \\ &= -\frac{\langle\tilde{q}|\gamma_\mu\not{k} + \not{k}\gamma_\mu|q\rangle}{\sqrt{2}\langle\tilde{q}k\rangle\langle qk\rangle} = -k_\mu\times\frac{\sqrt{2}\langle\tilde{q}q\rangle}{\langle\tilde{q}k\rangle\langle qk\rangle}\,.\end{aligned} \tag{2.29}$$

The freedom of choice of q can be used to simplify the expressions in the calculations, since ε has some interesting properties:

$$\begin{aligned}\varepsilon^\pm(k_i;q)\cdot q &= 0\\ \varepsilon^+(k_i;q)\cdot\varepsilon^+(k_j;q) &= \varepsilon^-(k_i;q)\cdot\varepsilon^-(k_j;q) = 0\\ \varepsilon^+(k_i;k_j)\cdot\varepsilon^-(k_j;q) &= \varepsilon^+(k_i;q)\cdot\varepsilon^-(k_j;k_i) = 0\\ \not{\varepsilon}^+(k_i;k_j)|j\rangle &= \not{\varepsilon}^-(k_i;k_j)|j] = 0\\ [j|\varepsilon^-(k_i;k_j) &= \langle j|\not{\varepsilon}^+(k_i;k_j) = 0\,.\end{aligned} \tag{2.30}$$

In our calculations, we will often use for helicity-like gluons identical gauge momenta and equal to the external momentum of one of the gluons of opposite helicity.

Chapter 3

Recursion relations with heavy particles

3.1 Introduction

At the LHC, the high energy reached will lead to various processes where heavy particles will be produced. Therefore, scattering amplitudes where particles masses are not neglected are needed for phenomenological applications. However, when massive fermions, scalars or boson vectors are incorporated to a pure gluon amplitude, calculations become more difficult and huge results are found, due to the new couplings to be taken into account. In this chapter we will deal with these calculations, managing to get to simpler and easier to handle results. In particular, we will focus on amplitudes with colored, massive scalar–antiscalar pairs.

Colored scalars have a great importance for two main reasons. The first one is that it is possible to relate scalar and quark amplitudes, by means of the Supersymmetric Ward Identities [44]. Indeed, we can think about QCD at tree level as a supersymmetric theory [23,45]. If we consider pure gluon processes, we do not have loops at tree level, therefore no fermions exist that can circulate. We can then replace them with supersymmetric particles like gluinos for instance. At the level of partial amplitudes, in processes with quarks, we have no means of distinguishing a quark from a gluino, once we have extracted the color factor. This allow us to use indistinctly one or the other. Thanks to commutation properties between supersymmetric charges and fields, it is possible to find the following relationships between amplitudes with quarks and amplitudes with scalars:

$$\begin{aligned} A^n(1_q^+, 2^+, ..., n-1^+, n_{\bar{q}}^-) &= \frac{\langle \ell_n q\rangle}{\langle \ell_1 q\rangle} A^n(1_s^+, 2^+, ..., n-1^+, n_{\bar{s}}^-)\,, \\ A^n(1_q^+, 2^+, ..., j^-, ..., n-1^+, n_{\bar{q}}^-) &= \frac{\langle \ell_n j\rangle}{\langle \ell_1 j\rangle} A^n(1_s^+, 2^+, ..., j^-, ..., n-1^+, n_{\bar{s}}^-)\,, \end{aligned} \tag{3.1}$$

where ℓ_i is the auxiliary massless momentum for massive particles defined in Appendix A as:

$$\ell_i := p_i - \frac{p_i^2}{2p_k \cdot p_i} p_k\,, \tag{3.2}$$

where p_i is the momentum of the massive particle, and p_k a light–like vector. Eqs. (3.1) hold in SUSY at every order in perturbation theory. At tree level, these amplitudes are identical to the QCD ones so that, in principle, we can deal with the most comfortable amplitude, choosing between scalars and fermions. Since scalars are spinless, working with them is easier: their helicity is zero and this prevents the complications due to polarization, such as the double choice of the helicity of the internal propagator in the BCFW recursion relations. The second motivation for the choice of scalars involves one–loop calculations. Although QCD amplitudes are not the same as the SUSY ones at one loop, a decomposition of them in terms of supersymmetric pieces is still possible and useful [46]. For a generic helicity configuration the partial amplitude depends on the number of particles with different spins that can enter the loop, according to the following relationship:

$$A_{n;1} = A^g_{n;1} + \frac{n_f}{N_c} A^f_{n;1} + \frac{n_f}{N_c} A^s_{n;1}, \tag{3.3}$$

where the superscripts refer to the spin of the particles (gluons, fermions or complex scalars). Some relationships among these amplitudes hold for specific helicity configurations, for example:

$$A_{n;1}(1^{\pm}, 2^+, \ldots, n^+) = (1 + \frac{n_s}{N_c} - \frac{n_f}{N_c}) A^s_{n;1}, \tag{3.4}$$

where the factor $1/N_c$ is generated in the conversion from fundamental to adjoint representations in the loop. String theory inspired a method for decomposing QCD amplitudes in supersymmetric and non–supersymmetric parts. For a n–gluon one loop amplitude the gluonic and fermionic contributions can be written as:

$$\begin{aligned} A^f_{n;1} &= A^{\mathcal{N}=1}_{n;1} - A^s_{n;1}\,, \\ A^g_{n;1} &= A^{\mathcal{N}=4}_{n;1} - 4A^{\mathcal{N}=1}_{n;1} + A^s_{n;1} \end{aligned} \tag{3.5}$$

and

$$\begin{aligned} A^{\mathcal{N}=1}_{n;1} &= A^f_{n;1} + A^s_{n;1}\,, \\ A^{\mathcal{N}=4}_{n;1} &= A^g_{n;1} + 4A^f_{n;1} + 3A^s_{n;1}. \end{aligned} \tag{3.6}$$

$A^{\mathcal{N}=1}_{n;1}$ indicates the contribution of a supersymmetric chiral multiplet formed by a scalar and a fermion. On the contrary, $A^{\mathcal{N}=4}_{n;1}$ is the contribution of a supersymmetric vector multiplet that contains one gluon, four fermions and three complex scalars. In Eq. (3.5) the one–loop gluon term receives as unique non–supersymmetric contribution a scalar one, that can be found in terms of tree level amplitudes, by means of the Optical Theorem and the Cutkosky rules [46].

3.2 $A_n(1_s; 2^+, ..., n-1^+; n_{\bar{s}})$

3.2.1 Introduction

To begin with, we consider a n-gluon amplitude with two massive colored scalars. The authors of [47] have considered amplitudes with a pair of massive scalars and n gluons of

positive helicity. They make an ansatz for such an amplitude and then they prove it by verifying that BGKS recursion relations are satisfied. Once this result has been obtained, it can be used to construct the amplitude with one–negative helicity gluon in any position, by means of recursion relations. Indeed, the amplitude with n all-positive gluons is one piece of the decomposition of the one-negative amplitude over its singularities. The other piece is the unknown amplitude with $n-1$ legs, from which the recursion relation is build. The expressions thus found are large and have complicated denominators that are dangerous when numerical computations are performed, since they can produce zeros. Actually, these denominators are spurious, because in the amplitudes calculated with Feynman diagrams only multiparticle poles can be generated, as they occur when a propagator goes on–shell. Therefore, there must be a way of eliminating them.

In our first calculation [48] we managed to find a very compact expression for the all–positive helicity amplitude with colored massive scalars, through recursion relations. As we mentioned in Section 2.2, recursion relations are based on off–shell currents, that is amplitudes where one leg is off–shell. The building blocks of our calculation are then the gluon and the scalar–gluon off–shell currents and we combine them with BCFW recursion relations.

3.2.2 Off–shell gluon current

To construct a n–leg current we have to take into account all the possible vertices that can be present. In the case of gluonic amplitudes, we deal with the three–gluon and four–gluon vertices shown in Fig. 2.4. The current with n external legs is the sum of all the possible ways to connect currents with a lower number of legs by these two vertices, as it is shown in Fig. 3.1.

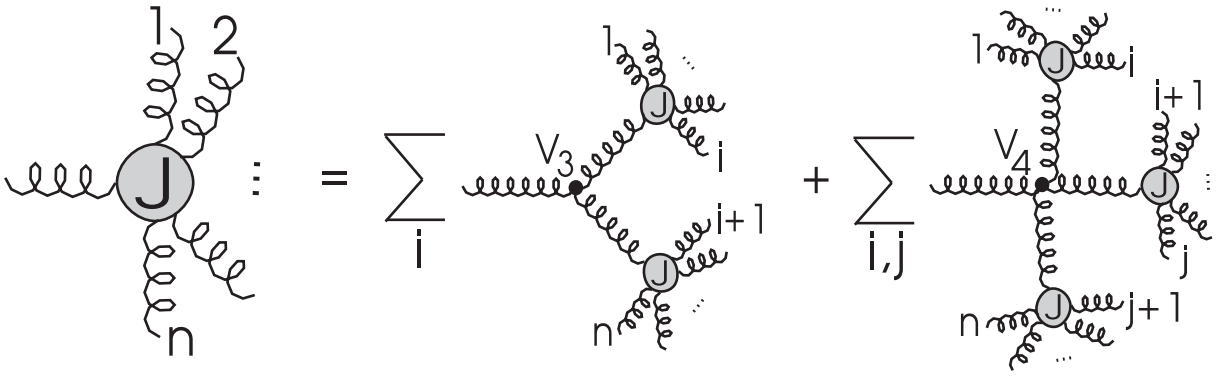

Figure 3.1: The recursion relation for the off–shell gluon current $J^{\mu}(1,2,\ldots,n)$ [45].

The current is then given by [45]:

$$J^\mu(1,2,\ldots,n) = \frac{-i}{p_{1,n}^2}\left[\sum_{i=1}^{n-1} V_3^{\mu\nu\rho}(p_{1,i},p_{i+1,n})\; J_\nu(1,\ldots,i)\; J_\rho(i+1,\ldots,n)\right.$$
$$\left. + \sum_{j=i+1}^{n-1}\sum_{i=1}^{n-2} V_4^{\mu\nu\rho\sigma}(p_{1,i},p_{i+1,j},p_{j+1,n})\; J_\nu(1,\ldots,i)\; J_\rho(i+1,\ldots,j)\; J_\sigma(j+1,\ldots,n)\right]. \tag{3.7}$$

There are special helicity configurations whose recursion relations (3.7) have been resolved, such as the all–positive helicity case [29]. If the same reference momentum ξ for all the gluons is chosen, the current has this shape:

$$J^\mu(1^+,2^+,\ldots,n^+) \;= \frac{\langle\xi|\gamma^\mu \not{p}_{1,n}|\xi\rangle}{\sqrt{2}\langle\xi 1\rangle\langle 12\rangle\cdots\langle n\xi\rangle}\,. \tag{3.8}$$

In order to extract amplitudes from the off–shell currents, what we have to do is to replace the $(n+1)$th gluon propagator with the polarization vector, so that the amplitude can be written in terms of the current J^μ as:

$$A_{n+1}(1,2,\ldots,n+1) = ip_{1,n}^2\varepsilon_\mu(p_{n+1})J^\mu(1,2,\ldots,n)\Big|_{p_{1,n}^2=0} \tag{3.9}$$

where we call $\sum_{i=1}^k p_i \equiv p_{1,k}$ and we remember that the gluon propagator is $-i/p_{1,n}^2$ [23,45]. Passing from amplitudes to currents, the momentum conservation is preserved, but in the current the $(n+1)$th particle is now off–shell, that is p_{n+1}^2 is not zero. For this reason currents are not physical objects and can depend on the gauge choice for the remaining gluons. In the all–positive helicity case (3.8), J^μ has no poles in $p_{1,n}^2$, therefore, once we multiply by $p_{1,n}^2$ and impose the on–shell constraint $p_{n+1}^2 = p_{1,n}^2 = 0$, the amplitude $A(1^+,\ldots,n+1^+)$ vanishes.

3.2.3 Off–shell scalar–gluon currents and amplitudes

The Lagrangian that generates the scalar–gluon coupling is the scalar QCD:

$$\mathcal{L}_{\text{scalar QCD}} = -\frac{1}{4}G_{\mu\nu}^a G_a^{\mu\nu} + D_\mu^\dagger\Phi^\dagger D^\mu\Phi - m^2\Phi^\dagger\Phi\,, \tag{3.10}$$

where

$$D_\mu = \partial_\mu - igA_\mu^a\frac{T_a}{\sqrt{2}}\,.$$

The possible interactions are shown in Fig. 3.2.

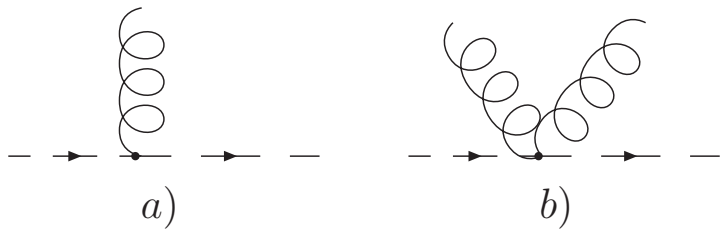

Figure 3.2: Scalar QCD vertices.

The a) vertex reads:

$$ig\frac{T^a}{\sqrt{2}}(p_s^\mu - p_{\bar{s}}^\mu)\,, \tag{3.11}$$

thus getting the color ordered Feynman rule:

$$\frac{i}{\sqrt{2}}(p_s^\mu - p_{\bar{s}}^\mu). \tag{3.12}$$

The two scalars–two gluons coupling of Fig. 3.2 b) can be set to zero by a convenient gauge choice. Indeed, it is proportional to the scalar product of the two polarization vectors $\varepsilon(p_1)\cdot\varepsilon(p_2)$, which is zero for gluons of the same helicity if the gauge momenta are chosen to be the same for both polarization vectors (Eq. 2.30). On the other hand, for gluons that have opposite polarizations, $\varepsilon(p_1)\cdot\varepsilon(p_2)$ vanishes if the gauge momentum of the first boson is set equal to the momentum of the other one.

Once we know the interaction among the involved fields, we can construct the current $S(1_s;\ldots,n-1)$, with the anti–scalar off–shell. By definition

$$S(1_s) = 1\,. \tag{3.13}$$

For the one–gluon current $S(1_s;2)$ we need to add the gluon–scalar vertex. From momentum conservation, the momentum of the antiscalar can be written in terms of the others $p_{\bar{s}} = -p_s - p_g$, thus:

$$(p_s - p_{\bar{s}})\cdot\varepsilon(p_g) = (2p_s - p_g)\cdot\varepsilon(p_g) = 2p_s\cdot\varepsilon(p_g), \tag{3.14}$$

where we have taken into account that $\varepsilon(k)\cdot k = 0$. The current with one gluon is obtained multiplying the vertex by the scalar propagator i/y_{12}:

$$S(1_s;2^+) = S(1_s)i\sqrt{2}p_1\cdot\varepsilon^*(p_2)\frac{i}{y_{12}} = -\frac{\sqrt{2}}{y_{12}}p_1\cdot J(2^+), \tag{3.15}$$

where we have called p_1 the momentum of the scalar and we have defined $y_{1,j} = (p_1 + \ldots + p_j)^2 - m^2$. With two gluons we have two ways of building the current, as shown in Fig. 3.3. Thus, in terms of the currents just built, we have:

$$S(1_s;2^+,3^+) = -\frac{\sqrt{2}}{y_{1,3}}\Big(S(1_s)\;p_1\cdot J(2^+,3^+) + S(1_s;2^+)\;p_{12}\cdot J(3^+)\Big). \tag{3.16}$$

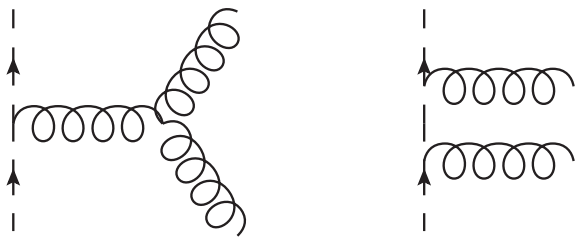

Figure 3.3: The two graphs for $S(1_s; 2^+, 3^+)$.

In the second term we have from momentum conservation: $p_{\bar{s}} = -p_{12} - p_3$ and, once we contract with $J(3^+)$, we are left with $2p_{12} \cdot J(3^+)$. The $1/y_{1,3}$ term comes from the scalar propagator, since we are building off–shell currents. Going on with this procedure we arrive at the recursion relation for the current :

$$S(1_s; 2^+, \dots, n-1^+) = -\frac{\sqrt{2}}{y_{1,n-1}} \sum_{k=1}^{n-2} S(1_s; 2^+, \dots, k^+) p_{1,k} \cdot J(k+1^+, \dots, n-1^+). \quad (3.17)$$

Let us underline how the $p_{1,k}$ momentum is created. The vertex with the momenta conservation would give a momentum $2p^\mu_{1,k} + p^\mu_{k+1,n-1}$ that is contracted with the gluon current giving:

$$\frac{\langle\xi|(2\not{p}_{1,k} + \not{p}_{k+1,n-1})\not{p}_{k+1,n-1}|\xi\rangle}{\sqrt{2}\langle\xi\, k{+}1\rangle\langle\langle k{+}1, n{-}1\rangle\rangle\langle n{-}1\,\xi\rangle} = \sqrt{2}\frac{\langle\xi|\not{p}_{1,k}\not{p}_{k+1,n-1}|\xi\rangle}{\langle\xi\, k{+}1\rangle\langle\langle k{+}1, n{-}1\rangle\rangle\langle n{-}1\,\xi\rangle}\,, \quad (3.18)$$

where $\langle\langle i, j\rangle\rangle \equiv \langle i\, i{+}1\rangle \dots \langle j{-}1\, j\rangle$. We have seen that the on–shell amplitude is obtained from the current divided by the propagator by putting the anti–scalar momentum on–shell, that is $p_n^2 = p_{1,n-1}^2 = m^2$, i.e. $y_{1,n-1} = 0$:

$$A_n(1_s; 2^+, \dots, n-1^+; n_{\bar{s}}) = S(1_s; 2^+, \dots, n-1^+)\frac{y_{1,n-1}}{i}\Big|_{y_{1,n-1}=0}. \quad (3.19)$$

Looking at Eq. (3.19), we are led to divide the current into a part that contains a factor $1/y_{1,n-1}$ and another that does not. Thus, the latter goes to zero once the momentum goes on–shell. We observe that the term of the sum in (3.17) for $k = n-2$ can be written as:

$$-\frac{1}{y_{1,n-1}\langle n{-}1\,\xi\rangle}\, S(1_s; 2^+, \dots, n-2^+)\langle\xi|\not{p}_{1,n-2}\not{p}_{n-1}|\xi\rangle. \quad (3.20)$$

The following relationship holds for every k, due to the Schouten identity and a few tricks of spinorial helicity formalism:

$$\begin{aligned}\langle\xi|\not{p}_{1,k}\not{p}_{k+1,n-1}|\xi\rangle &= \frac{1}{\langle k\, k{+}1\rangle}\Big(\langle\xi\, k{+}1\rangle\langle k|y_{1,k-1} + \not{p}_{1,k-1}\not{p}_{k,n-1}|\xi\rangle + \\ &+ \langle k\xi\rangle\langle k{+}1|y_{1,k} + \not{p}_{1,k}\not{p}_{k+1,n-1}|\xi\rangle\Big). \end{aligned} \quad (3.21)$$

Applying Eq. (3.21), Eq. (3.20) becomes:

$$-\frac{S(1_s;2^+,\ldots,n-2^+)}{y_{1,n-1}\langle n{-}1\,\xi\rangle\langle n{-}2\,n{-}1\rangle} \quad\times\quad \Big[\langle\xi n{-}1\rangle\langle n{-}2|y_{1,n-3}+\not{p}_{1,n-3}\not{p}_{n-2,n-1}|\xi\rangle + \\ -\langle\xi n{-}2\rangle\langle n{-}1|y_{1,n-2}+\not{p}_{1,n-2}\not{p}_{n-1}|\xi\rangle\Big]. \tag{3.22}$$

With the following relationship:

$$y_{1,n-1}=y_{1,n-2}+\not{p}_{1,n-2}\not{p}_{n-1}+\not{p}_{n-1}\not{p}_{1,n-2} \tag{3.23}$$

the second term of Eq. (3.22) is transformed into:

$$\frac{\langle\xi\,n{-}2\rangle}{\langle n{-}2\,n{-}1\rangle\langle\xi\,n{-}1\rangle}\,S(1_s;2^+,\ldots,n-2^+), \tag{3.24}$$

i.e. $y_{1,n-1}$ in the denominator disappears. Applying the transformation (3.21) to all the terms of the current, we do not find any other term in which $y_{1,n-1}$ disappears, thus we can write, for every n:

$$\begin{aligned} S(1_s;2^+,\ldots,n-1^+) &= \frac{\langle n{-}2\,\xi\rangle}{\langle n{-}2\,n{-}1\rangle\langle n{-}1\,\xi\rangle}\,S(1_s;2^+,\ldots,n-2^+) \\ &+ \frac{i}{y_{1,n-1}}\,A_n(1_s;2^+,\ldots,n-1^+;n_{\bar{s}})\,. \end{aligned} \tag{3.25}$$

Let us find the first results for the amplitudes. In order to do this, we will use the following transformations in the calculation:

$$\langle\xi|\not{p}_1\not{p}_{2,n-1}|\xi\rangle=\frac{1}{y_{12}}\left(m^2\langle\xi 2\rangle[2|\not{p}_{3,n-1}|\xi\rangle+\langle\xi|\not{p}_1|2]\langle 2|\not{p}_1\not{p}_{2,n-1}|\xi\rangle\right)\,, \tag{3.26}$$

and then

$$[2|\not{p}_{3,n-1}|\xi\rangle=\frac{1}{y_{1,3}}\left([2|\not{p}_1\not{p}_{23}\not{p}_{4,n-1}|\xi\rangle-[32]\langle 3|y_{12}+\not{p}_{12}\not{p}_{3,n-1}|\xi\rangle\right)\,. \tag{3.27}$$

The well known $n=3$ on–shell amplitude can be obtained putting Eq. (3.15) in Eq. (3.19):

$$A_3(1_s;2^+;3_{\bar{s}})=i\,\frac{\langle\xi|\not{p}_1|2]}{\langle\xi 2\rangle}\,. \tag{3.28}$$

The following result is $S(1_s;2^+,3^+)$. By developing Eq. (3.16), we find:

$$S(1_s;2^+,3^+)=-\frac{\langle\xi|\not{p}_1\not{p}_{23}|\xi\rangle}{y_{1,3}\langle\xi 2\rangle\langle 23\rangle\langle 3\xi\rangle}+\frac{[2|\not{p}_1|\xi\rangle}{y_{1,3}y_{12}\langle\xi 2\rangle}\frac{\langle\xi|\not{p}_{12}\not{p}_3|\xi\rangle}{\langle\xi 3\rangle\langle 3\xi\rangle} \tag{3.29}$$

Then we apply the transformation (3.21) for $k=n{-}2=2$ and Eq. (3.23), and subsequently the transformation (3.26) finding thus:

$$S(1_s;2^+,3^+)=-m^2\frac{[23]}{y_{1,3}y_{12}\langle 23\rangle}-\frac{\langle\xi|\not{p}_1|2]}{\langle\xi 3\rangle\langle 23\rangle y_{12}} \tag{3.30}$$

and the amplitude:

$$A_4(1_s;2^+,3^+;4_{\bar{s}}) = i\frac{m^2[23]}{y_{12}\langle 23\rangle}. \tag{3.31}$$

For the following term $n=5$ the same substitutions are used, plus Eq. (3.27), thus finding:

$$A_5(1_s;2^+,3^+,4^+;5_{\bar{s}}) = i\,\frac{m^2[2|\not{p}_1\not{p}_{23}|4]}{y_{12}\,y_{1,3}\langle\langle 2,4\rangle\rangle}\ . \tag{3.32}$$

The $n=6$ amplitude is the first that presents two terms. Here we are going to summarize the steps to follow in order to find a compact result. The strategy is to perform the above substitutions in the general expression for the amplitude and then to analyze the result. Looking at Eq. (3.25) and comparing it with Eq. (3.17), we can write the generic amplitude A_n as:

$$\begin{aligned} A_n = \frac{y_{1,n-1}}{i}\Big(&-\frac{\sqrt{2}}{y_{1,n-1}}\sum_{k=1}^{n-3} S(1_s;2^+,\dots,k^+)p_{1,k}\cdot J(k+1^+,\dots,n-1^+) + \\ &-\frac{\langle n-2|y_{1,n-3}+\not{p}_{1,n-3}\not{p}_{n-2,n-1}|\xi\rangle}{y_{1,n-1}\langle n{-}1\,\xi\rangle\langle n{-}2\,n{-}1\rangle}S(1_s;2^+,\dots,n-2^+)\Big)\,. \end{aligned} \tag{3.33}$$

It is useful to further separate the sum, isolating the $k=1$ term. Replacing Eq. (3.26) and Eq. (3.27) in this term and Eq. (3.21) in the other terms of the sum, we obtain the following expression:

$$\begin{aligned} A_n = \ &-\ \frac{m^2[2|\not{p}_1\not{p}_{23}\not{p}_{4,n-1}|\xi\rangle}{iy_{12}y_{1,3}\langle n{-}1\,\xi\rangle\langle\langle 2,n{-}1\rangle\rangle} - \frac{1}{iy_{12}\langle n{-}1\,\xi\rangle\langle\xi 2\rangle\langle\langle 2,n{-}1\rangle\rangle}\Big[\frac{m^2\langle\xi 2\rangle}{y_{1,3}}\langle 3|y_{12}+\not{p}_{12}\not{p}_{3,n-1}|\xi\rangle + \\ &+\ \langle\xi|\not{p}_1|2]\langle 2|\not{p}_1\not{p}_{2,n-1}|\xi\rangle\Big] - \frac{1}{i\langle n{-}1\,\xi\rangle}\sum_{k=2}^{n-3} S(1_s;2^+,\dots,k^+)\times \\ &\times\ \frac{\langle\xi\,k{+}1\rangle\langle k|y_{1,k-1}+\not{p}_{1,k-1}\not{p}_{k,n-1}|\xi\rangle + \langle k\xi\rangle\langle k{+}1|y_{1,k}+\not{p}_{1,k}\not{p}_{k+1,n-1}|\xi\rangle}{\langle k\,k{+}1\rangle\langle\xi\,k{+}1\rangle\langle\langle k{+}1,n{-}1\rangle\rangle} + \\ &-\ \frac{1}{i\langle n{-}1\,\xi\rangle}\,S(1_s;2^+,\dots,n-2^+)\,\frac{\langle n-2|y_{1,n-3}+\not{p}_{1,n-3}\not{p}_{n-2,n-1}|\xi\rangle}{\langle n{-}2\,n{-}1\rangle}\,. \end{aligned} \tag{3.34}$$

Now we perform the transformation

$$[2|\not{p}_1\not{p}_{23}\not{p}_{4,n-1}|\xi\rangle = \sum_{i=4}^{n-1}[2|\not{p}_1\not{p}_{23}|i]\langle i\,\xi\rangle \tag{3.35}$$

on the first term and then we use Eq. (3.23) to replace the terms that contain a sum such as $y_{1,\ell}+\not{p}_{1,\ell}\not{p}_{\ell+1,n-1}$ in the following way:

$$\langle\ell+1|y_{1,\ell}+\not{p}_{1,\ell}\not{p}_{\ell+1,n-1}|\xi\rangle = y_{1,\ell+1}\langle\ell{+}1\,\xi\rangle + \sum_{i=\ell+2}^{n-1}\langle\ell{+}1|\not{p}_{1,\ell}|i]\langle i\xi\rangle\,. \tag{3.36}$$

The result that is obtained is very compact and can be written as:

$$A_n(1_s;2^+,\ldots,n-1^+;n_s) = i\,\frac{m^2}{y_{12}\,y_{1,3}\,\langle\langle 2,n{-}1\rangle\rangle}\Bigg\{[2|\not{p}_1\not{p}_{23}|n-1] + \\ +\sum_{j=1}^{n-5}[2|\not{p}_1\not{p}_{23}|w_1]\,\frac{\langle w_1|\not{p}_{1,w_1-1}|w_2]}{-y_{1,w_1}}\cdots\frac{\langle w_j|\not{p}_{1,w_j-1}|n-1]}{-y_{1,w_j}}\Bigg\}\,, \tag{3.37}$$

where $4 \le w_1 \le n-2$ and $w_i < w_{i+1}$ and all the possible values of w_i must be taken.

It can be seen that in this result the number of terms grows as 2^{n-5} and each of them is proportional to m^2, contrarily to what found in [47], thus making the result much simpler. It is useful to verify that Eq. (3.37) satisfies the BGKS recursion relations. As suggested in [47], we perform a shift in the four-momenta of the (2,3) gluons:

$$\hat{p}_2^\mu = p_2^\mu + \frac{z}{2}[2|\gamma^\mu|3\rangle\,, \\ \hat{p}_3^\mu = p_3^\mu - \frac{z}{2}[2|\gamma^\mu|3\rangle\,. \tag{3.38}$$

This shift corresponds to the following shift of the spinors:

$$|\hat{2}\rangle = |2\rangle + z|3\rangle\,,\quad |\hat{2}] = |2]\,, \\ |\hat{3}] = |3] - z|2]\,,\quad |\hat{3}\rangle = |3\rangle\,. \tag{3.39}$$

The graphs that in principle appear in the recursion relation are shown in Fig. 3.4.

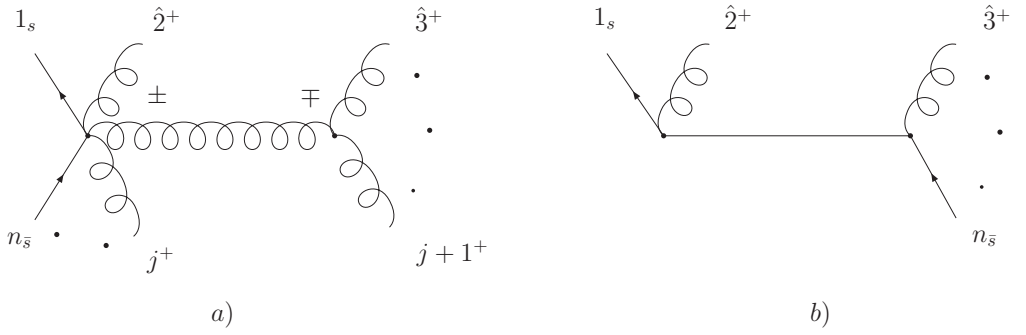

Figure 3.4: The recursion relation for A_n with the shift $\langle 2,3]$.

Graph a) is zero for both the helicities of the internal propagator, because the amplitude on the right vanishes for every value of j. Thus, the only term that contributes to the recursion relation is graph b), where only the scalar and the first gluon are factorized in the left side:

$$A_n(1_s;2^+,\ldots,n-1^+;n_{\bar{s}}) = A_3(1_s;\hat{2}^+;-\hat{p}_{12\bar{s}})\,\frac{i}{y_{12}}\,A_{n-1}(\hat{p}_{12s};\hat{3}^+,\ldots,n-1^+;n_{\bar{s}})\,. \tag{3.40}$$

Thus, choosing $\xi = \hat{3}$ in the left amplitude and taking into account that $\hat{p}_{1,k} = p_{1,k}$ if $k \geq 3$, Eq. (3.37) becomes:

$$A_n(1_s;2^+,\ldots,n-1^+;n_{\bar{s}}) = \\ i\,\frac{m^2\,[2|\not{p}_1\,\hat{\not{p}}_3\,\hat{\not{p}}_{12}\,\hat{\not{p}}_{34}}{y_{12}\,y_{1,3}\,y_{1,4}\,\langle\langle 2,n{-}1\rangle\rangle}\left\{|n-1] + \sum_{j=1}^{n-6}\,|w_1]\,\frac{\langle w_1|\not{p}_{1,w_1-1}|w_2]}{-y_{1,w_1}}\cdots\frac{\langle w_j|\not{p}_{1,w_j-1}|n-1]}{-y_{1,w_j}}\right\}, \tag{3.41}$$

where $w_k \in [5,\ldots,n-2]$. Replacing $z = -y_{12}/[2|\not{p}_1|3\rangle$ for the channel under consideration, we find the following relationship:

$$[2|\not{p}_1\,\hat{\not{p}}_3\,\hat{\not{p}}_{12}\,\hat{\not{p}}_{34} = [2|\not{p}_1\not{p}_{23}\,(y_{1,4} - \not{p}_4\,\not{p}_{1,3})\ . \tag{3.42}$$

With the help of this relationship it is easy to demonstrate that (3.41) reproduces the on-shell amplitude (3.37). The first term in the rhs of (3.42) generates all the terms that do not contain the $1/y_{1,4}$ propagator, while the second term initiates the spinorial chains for which $w_1 = 4$. This fact also explains why the number of terms contributing to the amplitude doubles each time that we add one extra gluon. On the other hand, it is worth to notice that we can bring the first term of the rhs of (3.42) into the form

$$[2|\not{p}_1\not{p}_{23} = [2|(y_{1,3} - \not{p}_3\not{p}_{12})\ , \tag{3.43}$$

thus obtaining:

$$A_n(1_s;2^+,\ldots,n-1^+;n_{\bar{s}}) = i\,\frac{m^2\,[2|(y_{1,3}-\not{p}_3\not{p}_{12})\,(y_{1,4}-\not{p}_4\,\not{p}_{1,3})}{y_{12}\,y_{1,3}\,y_{1,4}\,\langle\langle 2,n{-}1\rangle\rangle}\left\{|n-1] + \right. \\ \left. + \sum_{j=1}^{n-6}\,|w_1]\,\frac{\langle w_1|\not{p}_{1,w_1-1}|w_2]}{-y_{1,w_1}}\cdots\frac{\langle w_j|\not{p}_{1,w_j-1}|n-1]}{-y_{1,w_j}}\right\}, \tag{3.44}$$

This suggests that we can regroup all the terms in the sum into a single one. Our final result for the amplitude with all gluons of positive helicity becomes thus:

$$\begin{aligned} A_n(1_s;2^+,\ldots,n-1^+;n_{\bar{s}}) &= i\,m^2\,\frac{[2|\prod_{k=3}^{n-2}(y_{1,k}-\not{p}_k\not{p}_{1,k-1})|n-1]}{y_{12}\,y_{1,3}\cdots y_{1,n-2}\,\langle\langle 2,n{-}1\rangle\rangle} = \\ &= i\,m^2\,\frac{[2|\Phi_{3,j}|n-1]}{y_{12}\langle\langle 2,n{-}1\rangle\rangle}\ , \end{aligned} \tag{3.45}$$

where

$$\Phi_{3,j} \equiv \prod_{k=3}^{j}\left(1 - \frac{\not{p}_k\not{p}_{1,k-1}}{y_{1,k}}\right). \tag{3.46}$$

Result (3.45), reported in Ref. [48], is extremely compact, compared, for instance, to the previous expression given in Ref. [47]. This makes it very useful in successive calculations, and as a tool to verify other results (see, e. g., Ref. [44]).

3.3 Amplitudes with a self–dual ϕ scalar

3.3.1 Introduction

Once we have obtained the form of the amplitude (3.45), it is interesting to investigate how things change if a self–dual colorless complex ϕ scalar is added.

One of the principal aims of LHC is to discover the Higgs boson, the particle predicted by the Standard Model to be the responsible of particles having a mass. The principal production channel will be the $gg \to H$ process, via a heavy–quark loop [49]. Since loops with other quarks are suppressed by a factor of the order of m_q^2/m_t^2, we can take into account only the top contribution. NLO corrections to $gg \to H$ are important, since they increase the cross section by around 100%, but at the same time they are complicated since two–loops calculations are needed. However, in the large m_t mass limit we can deal with the effective vertex Hgg. This limit can be performed when the Higgs mass is lighter than the top pair production threshold, that is $m_H < 2m_t$. Thus, the NLO corrections involve only 1–loop diagrams and they are simpler to calculate. The production of the Higgs boson via gluon fusion is interesting also as a background of the vector–boson fusion $qq \to H + 2$ jets (VBF). This process is useful to measure the Higgs coupling with the vector bosons W and Z, as it is shown in Fig. 3.5. NLO corrections to this process are very small, therefore it is necessary to know its background in order to separate the interested signal [50]. Calculations of Higgs production together with many partons (gluons or fermions) is thus mandatory for LHC physics.

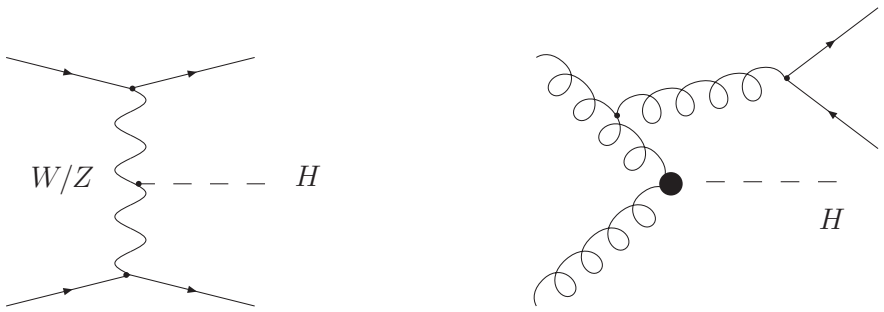

Figure 3.5: Higgs + 2 jets production via VBF (left) and via gluon fusion (right).

Currently, the mass of the Higgs seems to be not too large. The global electroweak fit gives an upper limit of 182 GeV [2]. In this case, we can use the effective vertex that is generated from integrating out the top mass in the gluon fusion.

The effective Lagrangian which we start from, in order to find the effective vertex, is [49]:

$$\mathcal{L}_{H,A}^{\text{int}} = \frac{C}{2}\Big[H\ \text{Tr}G_{\mu\nu}G^{\mu\nu} + iA\ \text{Tr}G_{\mu\nu}\,{}^*G^{\mu\nu}\Big], \tag{3.47}$$

where two Higgs fields are introduced. H is a scalar field, while A is a pseudoscalar one. It is useful to define two complex auxiliary fields ϕ and $\phi^\dagger$, since the Lagrangian is simpler if we use them. The ϕ field is such that the scalar Higgs is the real part of it:

$$H = \phi + \phi^\dagger \ , \quad A = \frac{1}{i}(\phi - \phi^\dagger) \ . \tag{3.48}$$

Introducing the selfdual (SD) and anti–selfdual (ASD) gluon fields strengths

$$G^{\mu\nu}_{SD} = \frac{1}{2}(G^{\mu\nu} + {}^*G^{\mu\nu}) \ , \quad G^{\mu\nu}_{ASD} = \frac{1}{2}(G^{\mu\nu} - {}^*G^{\mu\nu}) \ , \quad {}^*G^{\mu\nu} \equiv \tfrac{i}{2}\epsilon^{\mu\nu\rho\sigma}G_{\rho\sigma} \tag{3.49}$$

the Lagrangian becomes:

$$\mathcal{L}^{\rm int}_{\phi,\phi^\dagger} \ = \ C\Big[\phi \ {\rm Tr}G_{SD\,\mu\nu}G^{\mu\nu}_{SD} + \phi^\dagger \ {\rm Tr}G_{ASD\,\mu\nu}G^{\mu\nu}_{ASD}\Big]. \tag{3.50}$$

The amplitudes in terms of the new fields ϕ and $\phi^\dagger$ are simpler and to recover the result for the Higgs we only need to sum the two amplitudes. The effective vertices found are:

$$\begin{aligned} V^{\phi gg}_{\mu\nu} \ &= \ -2i(g_{\mu\nu}p_1\cdot p_2 - p_2^\mu p_1^\nu - i\varepsilon_{\mu\nu\rho\sigma}p_1^\rho p_2^\sigma) \\ V^{\phi ggg}_{\mu\nu\rho} \ &= \ -\sqrt{2}i\Big(g_{\mu\nu}(p_1{-}p_2)_\rho + g_{\nu\rho}(p_2{-}p_3)_\mu + g_{\rho\mu}(p_3{-}p_1)_\nu + i\varepsilon_{\mu\nu\rho\alpha}(p_1{+}p_2{+}p_3)^\alpha\Big) \ . \end{aligned} \tag{3.51}$$

Let us review the results found so far. The all–positive and one–negative amplitudes are:

$$A_n(\phi, 1^\pm, 2^+, \ldots, n^+) = 0 \tag{3.52}$$

and, if a fermion–antifermion pair is added,

$$A_n(\phi, 1^-_f, 2^+, \ldots, j^+_f, \ldots, n^+) = 0 \, , \tag{3.53}$$

for both massless and massive quarks [51]. We have no null results when the helicity of one gluon becomes negative. For the gluon case, the MHV–like amplitude is:

$$A_n(\phi, 1^+, 2^+, \ldots, i^-, \ldots, j^-, \ldots, n^+) \ = \ \frac{\langle ij\rangle^4}{\langle 12\rangle\cdots\langle n1\rangle} \, . \tag{3.54}$$

When quarks are present, in the massless case it holds:

$$A(\phi, 1^+_f, 2^+, \ldots, j^-_f, \ldots, m^-, \ldots, n^+) \ = \ \frac{\langle jm\rangle^3\langle 1m\rangle}{\langle 12\rangle\langle 23\rangle\cdots\langle n1\rangle} \, . \tag{3.55}$$

In Eqs. (3.54) and (3.55) there is a $2i$ factor of difference with respect to our notation. It is important to notice that these amplitudes are the same in form as pure QCD. What is different is the conservation of the momenta that now include the one carried by ϕ. However, the $V^{\phi gg}$ vertex creates an amplitude that does not exist in QCD, that is the one for $n = 2$:

$$A(\phi, 1^-, 2^-) = -\langle 12\rangle^2. \tag{3.56}$$

3.3.2 Calculation of amplitudes by Feynman diagrams

Our objective is to consider amplitudes with massive particles. We will focus our attention on amplitudes with a massive colored scalar–antiscalar pair and a generic number of gluons, starting from the one–negative helicity gluon placed next to the antiscalar.

$A_3(\phi; 1_s; 2^-; 3_{\bar{s}})$

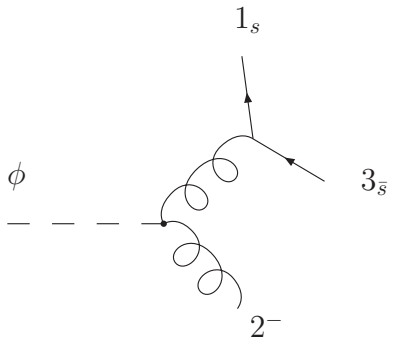

Figure 3.6: $n = 3$ amplitude with massive scalars.

The first amplitude that we calculate is the $n = 3$ one. Here the only possible vertex is $V^{\phi gg}$ (Eq. (3.51)). After a few manipulations, the amplitude results to be:

$$A_3(\phi; 1_s; 2^-; 3_{\bar{s}}) = -2i\frac{\langle 2|\not{p}_1\not{p}_3|2\rangle}{s_{13}}\,. \tag{3.57}$$

$A_4(\phi; 1_s; 2^+, 3^-; 4_{\bar{s}})$

The $n = 4$ amplitude receives contributions from both the two–gluon and the three–gluon couplings with the ϕ. The four possible contributions are shown in Fig. 3.7. However, choosing the gauge $\xi_2 = p_3$, $\xi_3 = p_2$, we are only left with two of them, that is a) and b). In both of them, the purely gluonic current and the effective vertex are the same, that is:

$$\begin{aligned} J_\rho(3^-) &= \frac{[\xi_3|\gamma_\rho|3\rangle}{\sqrt{2}[3\xi_3]}\,, \\ V^{\phi gg}_{\sigma\rho} &= (-2i)2\Big(g_{\sigma\rho}p_{124}\cdot p_3 - p_{3\sigma}p_{124\rho}\Big). \end{aligned} \tag{3.58}$$

We find the result:

$$A_4(\phi; 1_s; 2^+, 3^-; 4_{\bar{s}}) = \frac{-2i}{y_{12}s_{14}}\Big(\frac{\langle 3|\not{p}_1\not{p}_4|3\rangle\langle 3|\not{p}_1|2]}{\langle 23\rangle} - \frac{m^2}{s_{124}}\langle 3|\not{p}_{14}|2]^2\Big). \tag{3.59}$$

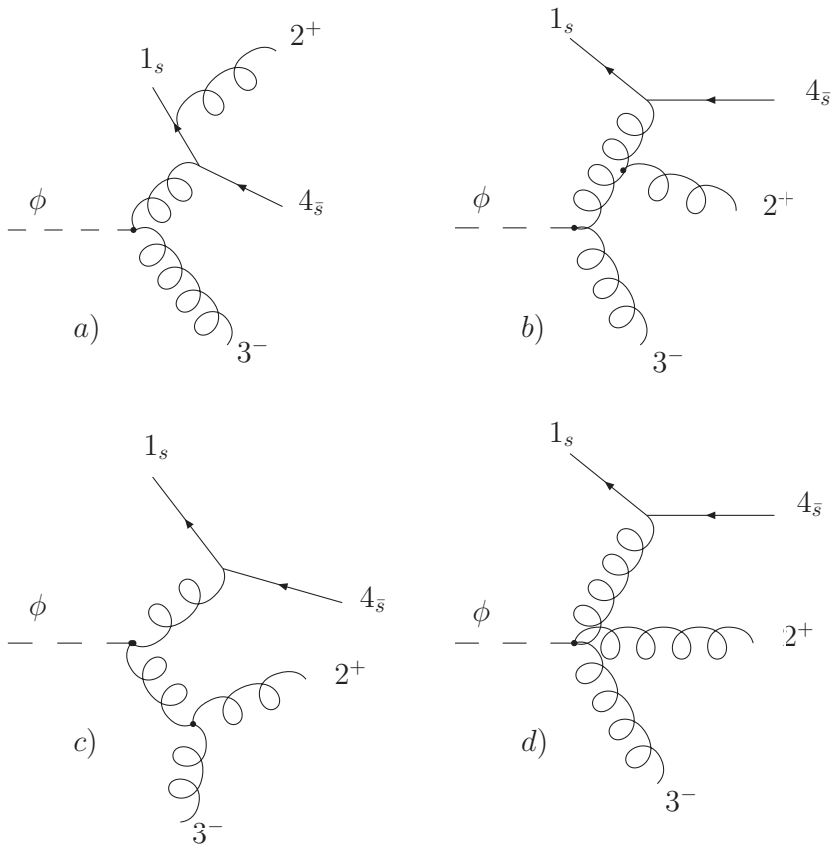

Figure 3.7: $n = 4$ amplitude with massive scalars: all the possible Feynman diagrams.

We note that this result has the correct massless limit

$$\lim_{m\to 0} A_4(\phi; 1_s; 2^+, 3^-; 4_{\bar{s}}) = -2i\frac{\langle 13\rangle^2\langle 34\rangle^2}{\langle\langle 1,4\rangle\rangle\langle 41\rangle} \tag{3.60}$$

up to a multiplicative factor. Let us remember in general the massless results in the case of scalars. From supersymmetry we have seen how to obtain relationships between amplitudes with a different content of particles. From Eq. (3.1) and Eq. (3.55) we obtain, up to a multiplicative factor,

$$A_n(1_s; 2^+ \ldots, m^-, \ldots; n_{\bar{s}}) = \frac{\langle m1\rangle^2\langle m\, n\rangle^2}{\langle\langle 1,n\rangle\rangle\langle n1\rangle}\,. \tag{3.61}$$

3.3.3 Calculation of amplitudes throguh recursion relations.

The calculations made in the previous subsection, obtained using the effective vertex, show that this method is quite complicated when the number of gluons grows. An alternative

method is the employment of BCFW recursion relations, which allows to save calculations by exploiting the $n-1$ results to get the n one. Thus, BCFW recursion relations seem to be the best tool for extending the calculations of the previous section to a generic number of gluons.

To start, we make the choice of analyzing an amplitude where the negative helicity gluon is placed in the last position, next to the antiscalar n. Let us first examine a shift like $\langle n{-}2\, n{-}1]$. The diagrams that appear are shown in Fig. 3.8.

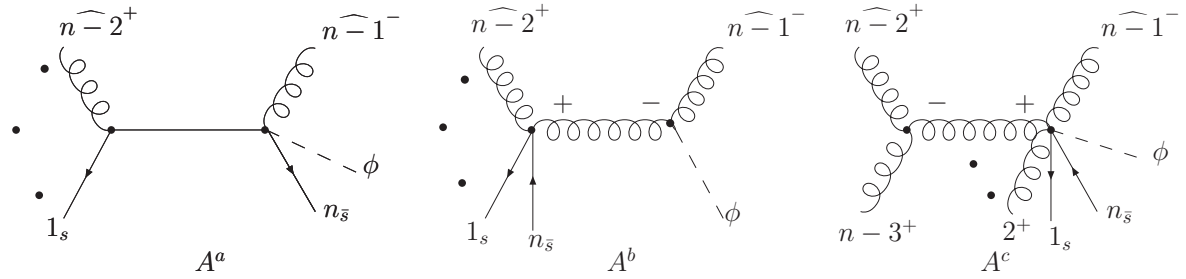

Figure 3.8: BCFW recursion relation for n amplitude, $\langle n{-}2\, n{-}1]$ shift.

We notice that in the right part of the third diagram there is exactly the same amplitude that we are going to calculate, with a gluon less. Of course this is quite annoying, because it would force us to construct the amplitude iteratively, as seen in [47], with huge calculations. The ideal situation would be performing a shift that allows automatically only known amplitudes, for example making the factorizations with the unwanted diagrams vanishing. Such a shift has been found and a result for $A_n(1_q; 2^+, \ldots, n-1^-; n_{\bar{q}})$ has been calculated by Schwinn and Weinzierl [52]. Their idea is to perform a shift on a massive fermion and on the negative helicity gluon. Thus, a factorization with the two fermions in different amplitudes cannot exist and the negative helicity gluon can never stay together with the fermion. This implies that the unknown amplitude cannot take part in the relations and only amplitudes with all positive gluons, for which we have shown a very compact form in Section 3.2, are present. The recursion relation reads:

$$A_n(1_q^{\lambda_1}, 2^-, 3^+, \ldots, n-1^+, n_{\bar{q}}^{\lambda_n}) = \sum_{j=3}^{n-1} A_{n-j+2}(\hat{1}_q^{\lambda_1}, \hat{P}_{2,j}^+ \ldots, j^+, j+1^+, \ldots, n-1^+, n_{\bar{q}}^{\lambda_n}) \frac{i}{P_{2,j}^2} A_j(\hat{P}_{2,j}^-, \hat{2}^-, 3^+, \ldots, j^+) \tag{3.62}$$

leading to the result

$$A_n(1_q^{\lambda_1}, 2^-, 3^+, \ldots, n-1^+, n_{\bar{q}}^{\lambda_n}) = 2^{n/2-1} i \frac{\langle \ell_n 2\rangle}{\langle \ell_1 2\rangle} \frac{1}{\langle 23\rangle \ldots \langle n{-}2\, n{-}1\rangle} \times \sum_{j=3}^{n-1} \frac{\langle 2|\not{p}_1 \not{p}_{2,j}|2\rangle^2}{p_{2,j}^2 \langle 2|\not{p}_1 \not{p}_{2,j}|j\rangle} \left(\delta_{j,n-1} + \delta_{j\neq n-1} \frac{m^2 \langle 2|\not{p}_{2,j} \Phi_{j+1,n-2}|n-1]\langle j\, j{+}1\rangle}{y_{1,j} \langle 2|\not{p}_1 \not{p}_{2,j}|j+1\rangle} \right) \tag{3.63}$$

with the notation

$$\Phi_{k,n-2} = \prod_{j=k}^{n-2} \left(1 - \frac{\not{p}_j \not{p}_{1,j}}{y_{1,j}} \right). \tag{3.64}$$

This result, however, presents some spurious denominators that can create problems when a numerical calculation is performed. These denominators have no physical meaning, because in the original Feynman diagrams only propagators can generate denominators, therefore there must be a way to eliminate them. Our purpose is to make the result simpler, so that denominators can be simplified. Unlike [52], we develop our analysis with colored scalars instead of quarks and a ϕ boson added. Moreover, our negative helicity gluon is $n-1$ instead of 2.

3.3.4 Canceling spurious poles

Performing the shift on the momenta p_n and p_{n-1}, we find only one kind of diagram different from zero, that is the one where the quark and the antiquark are factorized in the same amplitude together with a number $j-1$ of gluons. It is useful to consider separately the first diagram, where the left amplitude is a three–point one and the last, with $j = n-2$, as we show in Fig. 3.9. The shifted momenta, according to the shift on a massive particle

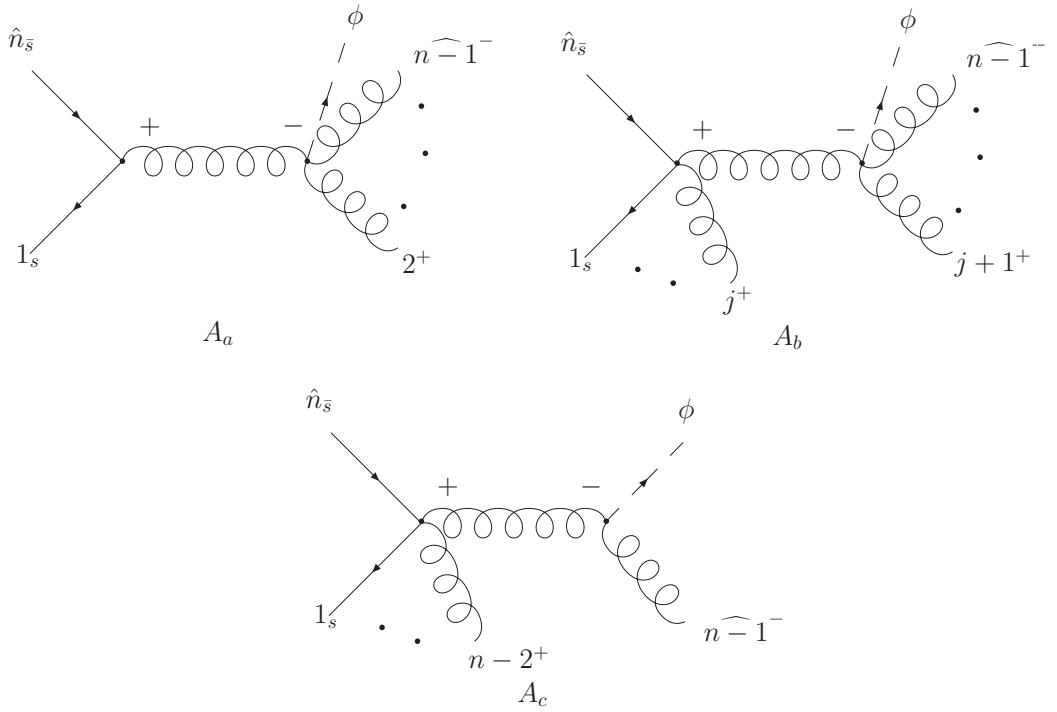

Figure 3.9: BCFW recursion relation for n amplitude, shift on p_n and p_{n-1}.

shown in Appendix A, are:

$$\begin{aligned}\hat{p}_n^\mu &= p_n^\mu - \frac{z}{2}\langle n-1|\gamma^\mu|\ell_n], \\ \hat{p}_{n-1}^\mu &= p_{n-1}^\mu + \frac{z}{2}\langle n-1|\gamma^\mu|\ell_n],\end{aligned} \tag{3.65}$$

where

$$\ell_n^\mu \equiv p_n^\mu - \frac{m^2}{2p_n\cdot p_{n-1}}p_{n-1}^\mu. \tag{3.66}$$

The recursion relation for A_a is:

$$A_a = A_L(1_s; -\hat{P}_{1n}^+; \hat{n}_{\bar{s}})\frac{i}{P_{1n}^2}A_R(\phi; \widehat{n-1}^-, \hat{P}_{1n}^-, 2^+, \ldots, n-2^+), \tag{3.67}$$

and the evaluation gives, up to a factor 2 that we will drop hereafter:

$$A_a = i\frac{\langle\xi|\not{p}_1| - \hat{P}_{1n}]}{\langle\xi - \hat{P}_{1n}\rangle}\,\frac{i}{P_{1n}^2}\,i\frac{\langle n{-}1\,\hat{P}_{1n}\rangle^3}{\langle\langle 2, n{-}1\rangle\rangle}. \tag{3.68}$$

Choosing the gauge $\xi = p_{n-1}$ and using some tricks of spinor properties, we obtain:

$$A_a = i\frac{\langle n-1|\not{p}_{1n}\not{p}_1|n-1\rangle}{P_{1n}^2\langle\langle 2, n{-}1\rangle\rangle}\,\frac{\langle n-1|\not{p}_n\not{p}_{1n}|n-1\rangle}{\langle n-1|\not{p}_n\not{p}_{1n}|2\rangle} = -i\frac{\langle n-1|\not{p}_1\not{p}_n|n-1\rangle^2}{s_{1n}\langle\langle 2, n{-}1\rangle\rangle\langle 2|\not{p}_1\not{p}_n|n-1\rangle}\,. \tag{3.69}$$

The second graph is given by:

$$A_b^j = im^2\frac{[2|\prod_{k=3}^j(y_{1,k} - \not{p}_k\not{p}_{1,k-1})| - \hat{p}_{nj}]}{y_{12}\cdots y_{1,j}\langle\langle 2, j\rangle\rangle\langle j\ - \hat{p}_{nj}\rangle}\frac{i}{p_{nj}^2}i\frac{\langle n{-}1\,\hat{p}_{nj}\rangle^3}{\langle\langle j{+}1, n{-}1\rangle\rangle\langle\hat{p}_{nj}\,j{+}1\rangle}\,, \tag{3.70}$$

where $p_{nj} \equiv p_{1,j} + p_n$. Using the same tricks as above, we get to the following result:

$$A_b^j = -im^2\frac{[2|\Phi_{3,j}\,\not{p}_{nj}|n-1\rangle}{\langle\langle 2, n{-}1\rangle\rangle s_{nj}}\frac{\langle j\,j{+}1\rangle\langle n-1|\not{p}_{nj}\not{p}_n|n-1\rangle^2}{\langle j|\not{p}_{nj}\not{p}_n|n-1\rangle\langle j+1|\not{p}_{nj}\not{p}_n|n-1\rangle}. \tag{3.71}$$

We see that the third graph in Fig. 3.9 is simply $A_c \equiv A_b^{n-2}$. This graph does not exist in pure QCD, but it appears now, since $A(\phi; -, -) \neq 0$, thus the sum over j runs from $j = 2$ to $j = n - 2$. Moreover, we can include A_a in the sum, too, as A_a^1. Putting together these results and grouping common factors, we arrive to the quite compact expression:

$$A = \frac{-i}{\langle\langle 2, n{-}1\rangle\rangle}\sum_{j=1}^{n-2}\frac{\langle n-1|\not{p}_n\not{p}_{nj}|n-1\rangle^2}{s_{nj}\langle n-1|\not{p}_n\not{p}_{nj}|j+1\rangle}\Big\{ - \delta_{j1} + \delta_{j\neq 1}m^2\frac{[2|\Phi_{3,j}\,\not{p}_{nj}|n-1\rangle\langle j\,j{+}1\rangle}{y_{12}\langle n-1|\not{p}_n\not{p}_{nj}|j\rangle}\Big\}. \tag{3.72}$$

We can easily check that the massless limit is the know one:

$$\lim_{m^2\to 0} A = -i\frac{\langle n{-}1\, n\rangle^2\langle n{-}1\, n\rangle^2}{\langle\langle 1,n\rangle\rangle\langle n1\rangle}. \tag{3.73}$$

Still, in this expression spurious denominators do hold over. The way of getting rid of them is to rearrange Eq. (3.72). The generic jth term for $j \geq 3$ can be manipulated in a quite laborious way in order to be divided in the sum of three parts:

$$\begin{aligned}
&\frac{\langle n-1|\not{p}_n\not{p}_{nj}|n-1\rangle^2\langle j\, j{+}1\rangle}{s_{nj}\langle n-1|\not{p}_n\not{p}_{nj}|j+1\rangle\langle n-1|\not{p}_n\not{p}_{nj}|j\rangle}[2|\Phi_{3,j}\,\not{p}_{nj}|n-1\rangle = \\
= \;& \frac{\langle n-1|\not{p}_n\not{p}_{nj}|n-1\rangle}{s_{nj}}\frac{\langle n{-}1\, j{+}1\rangle}{\langle n-1|\not{p}_n\not{p}_{nj}|j+1\rangle}[2|\Phi_{3,j}\,\not{p}_{nj}|n-1\rangle + \\
&+\frac{\langle n-1|\not{p}_n\not{p}_{nj}|n-1\rangle}{s_{nj}}\frac{\langle j\, n{-}1\rangle}{\langle n-1|\not{p}_n\not{p}_{nj}|j\rangle}[2|\Phi_{3,j-1}\,\not{p}_{nj-1}|n-1\rangle + \\
&+\frac{\langle n-1|\not{p}_n\not{p}_{nj}|n-1\rangle}{s_{nj}y_{1j}}[2|\Phi_{3,j-1}\,\not{p}_j|n{-}1\rangle \equiv a_j + b_j^1 + b_j^2
\end{aligned} \tag{3.74}$$

In this way, we can pass from one two–terms denominator to three single ones. Thus, we have the following kind of sum:

$$\ldots + a_j + b_j^1 + b_j^2 + a_{j+1} + b_{j+1}^1 + b_{j+1}^2 + \ldots \tag{3.75}$$

and we are going to sum every a_j term with the b_{j+1}^1 as it is graphically shown in (3.76):

$$\underbrace{\ldots + a_j + \underbrace{b_j^1 + b_j^2 + a_{j+1}} + b_{j+1}^1}_{\qquad\qquad\qquad\qquad} + \ldots. \tag{3.76}$$

The reason why we do this kind of grouping is that these terms have the same denominator and the same productory multiplied and the guess is that the sum of the numerators can give a quantity that cancels such a denominator. Actually, this happens and, after a bit more technicalities, the final result is found:

$$\begin{aligned}
A_n(\phi; 1_s, 2^+, \ldots, n-2^+, n-1^-, n_{\bar{s}}) = \frac{-i}{y_{12}\,\langle\langle 2, n{-}1\rangle\rangle}\Bigg\{ &\frac{[2|\not{p}_1|n-1\rangle\langle n-1|\not{p}_1\not{p}_n|n-1\rangle}{s_{n1}} \\
+ \sum_{j=2}^{n-2}\frac{m^2}{s_{n,j}}[2|\Phi_{3,j-1}&\left(\frac{\not{p}_j|n-1\rangle\langle n-1|\not{p}_n}{y_{1,j}} + \frac{\not{p}_{n,j-1}|n-1\rangle\langle n-1|\not{p}_j}{s_{n,j-1}}\right)\not{p}_{n,j}|n-1\rangle\Bigg\}.
\end{aligned} \tag{3.77}$$

This is a very compact form where all the spurious denominators have disappeared.

Chapter 4

The top quark

4.1 Introduction

The top quark was discovered in 1995 by the CDF and D0 experiments at the Tevatron $p\bar{p}$ collider, hosted at Fermilab [53, 54]. It was introduced as the weak isospin partner of the b quark, since the b quark detection in 1977 [55], for two principal reasons [56]. In the first place, its existence explains the absence of flavour changing neutral currents, through the GIM mechanism that was already introduced for the c quark. A second motivation, and more fundamental, is that the existence of three quark families, as well as three lepton families, guarantees the absence of anomalies in the electroweak theory, thus allowing it to be renormalizable. The weak isospin of the b quark was measured to be $-1/2$, so that the top quark had to be "up-type". Constraints on the top quark mass were set during the next years, thanks to electroweak precision data. Electroweak one-loop corrections Δr can be related to the W- and the Z-boson masses through:

$$m_W^2 = \frac{\pi \alpha_{\text{e.m.}}}{\sqrt{2} G_F} \frac{1}{\left(1 - \frac{m_W^2}{m_Z^2}\right)(1 - \Delta r)}\,, \tag{4.1}$$

where G_F is the Fermi electroweak constant and $\alpha_{\text{e.m.}} = \frac{e^2}{4\pi}$. The loop contributions coming from the top quark depend quadratically on the top quark mass, while those coming from the Higgs boson have a logarithmic dependence on the Higgs boson mass. This means that electroweak data can set stronger constraints on the top quark mass than on the Higgs mass. In Fig. 4.1 the top quark and the Higgs boson electroweak loop corrections to the W and Z boson self energies are showed. Eventually, the top quark was discovered exactly in the mass range predicted.

In the SM, the top quark is the heaviest known elementary particle, being as heavy as a gold atom. The most recent measurements at the Tevatron give the world average [57]:

$$m_t = 173.1 \pm 0.6_{\text{stat.}} \pm 1.7_{\text{syst.}}\ \text{GeV}\,. \tag{4.2}$$

This means that the top quark behaves differently from the other quarks [58]. Its lifetime is very short, so that the top quark decays before hadronizing. This way, some of its

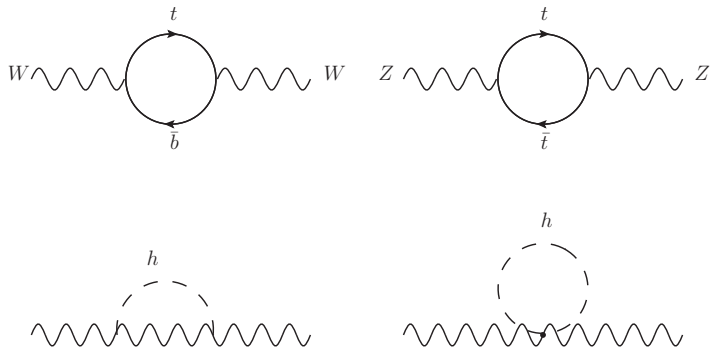

Figure 4.1: Electroweak loop contributions to the W and Z boson self energies originating from the top quark (up) and from the Higgs boson (down).

properties, such as, for example, the spin, are transferred directly to the decay products. The top does not get to be depolarized by the strong interactions, thus its spin can be studied in the angular distribution of the decay products. The space the top quark can fly before decaying is about 0.1 fm, less than the typical hadronic size. In this range, the QCD strength is still weak and the top quark behaves like a free particle. Due to the very short top quark life-time, in principle, any theoretical analysis should take into account both the production and the decay. Nevertheless, the decay width of the top quark is very narrow compared with its mass, being $\Gamma_t/m_t \simeq 0.008$, so it is possible to factorize the two processes with good approximation to an on-shell production and subsequent decay.

The top quark mass is heavy compared to the masses of the other quarks and it is of the same order of the Higgs boson vacuum expectation value. This fact suggests that the top quark could play an important role in the electroweak symmetry breaking (EWSB) and clarify the nature of this mechanism [59]. In the SM the particle responsible of the EWSB is the Higgs boson, that has not been observed yet. Other models have been developed where different particles plays the same role, for instance, a bound state of top quarks in technicolor and topcolor models, where top condensation is present. These models predict the existence of heavy gauge bosons coupling to top quarks. Also, extra-dimensional models such as Randall-Sundrum and ADD take into consideration the hierarchy problem, that is, why the weak scale is so different from the Planck scale. In these models, the existence of TeV gravitons is predicted, that couple to a $t\bar{t}$ pair. This changes the differential cross section distribution of top quark pair production from the SM prediction. For a review of new top dynamics in the EWSB, see, for example, [60].

4.2 Pair production

At the typical energies of hadron colliders, perturbative QCD can be used to describe the physics of the top quark. The $t\bar{t}$ pair production at the LHC is given at the tree level by

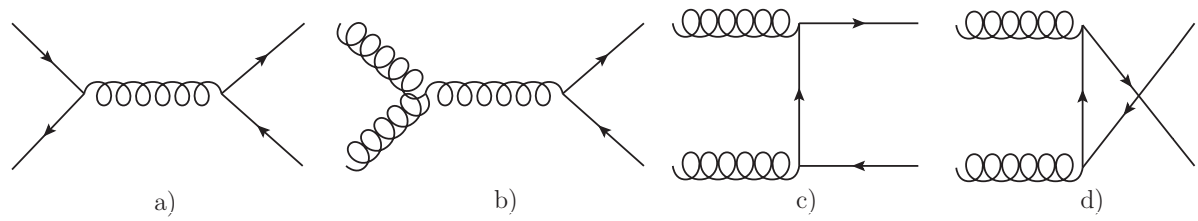

Figure 4.2: Graphs that contribute to the tree level QCD cross section in the quark-antiquark production.

the Feynman diagrams shown in Fig. 4.2, where in the SM the intermediate particle can be either a photon, a Z^0 or a gluon in events such as a) and a gluon in events of b) kind. Electromagnetic contributions to the cross section are usually negligible compared to the QCD ones. The factorization theorem tells us that at every order in perturbation theory the cross section is given by the convolution among the perturbative hard subprocess cross section and the parton distribution functions (PDFs) of the deep inelastic scattering:

$$d\sigma^{p_1 p_2 \to t\bar{t}X} = \int_0^1 dx_1 dx_2 \sum_{a,b} f_{a/p_1}(x_1, \mu_F^2) f_{b/p_2}(x_2, \mu_F^2) d\hat{\sigma}^{ab \to t\bar{t}X} . \tag{4.3}$$

The parton distribution function f_{a/p_1} represents the probability density distribution for the momentum fraction x_1 of the parton a inside the proton p_1. It is evaluated at a certain factorization scale μ_F, necessary in order to absorb the infinite quantities that arise from the collinear singularities. The partonic cross section can be written as:

$$\hat{\sigma}^{ab \to t\bar{t}X} = [\hat{\sigma}_0 + \alpha_S(\mu_R^2)\hat{\sigma}_1 + \ldots]^{ab \to t\bar{t}X} , \tag{4.4}$$

where μ_R^2 is the renormalization scale. At all orders in perturbation theory, $\sigma^{p_1 p_2 \to t\bar{t}X}$ does not depend on these scales, because the dependence of the subprocess cross section compensates the scale dependence of the PDFs. However, at a fixed order, this cancellation is not exact and an appropriate choice of the scales has to be made in order to minimize the fixed order dependence. Often, values of μ_R similar to the typical momentum scales of the scattering process and also $\mu_R = \mu_F$ are chosen. This avoids large logarithms [61]. The sum in Eq. (4.3) is over all the possible partonic subprocesses. The evolution of the parton distribution functions as a function of Q^2 is given by the DGLAP equations [62], while the dependence on the momentum fraction can only be extracted from fitting data.

4.3 Top quark decay

The t quark decays almost exclusively to a b quark, by emitting a W^+ boson: its branching ratio is $B(t \to bW^+) = 0.998$. While the b quark can be detected as a jet, the W gauge boson can decay either leptonically, to a lepton and a neutrino, or hadronically,

to a quark and an antiquark. The hadronic decay is roughly three times more probable than the leptonic one, since the quarks appear in three colors. Thus, there are different possible signals in $t\bar{t}$ production, depending on the decay mode of the two W bosons, as shown in Fig. 4.3. The all-hadronic mode (c), that is, where both W's decay hadronically, has the largest branching ratio, but it is also the most difficult experimentally, because all the signals are jets. The dilepton channel (b), where both the gauge bosons decay leptonically, has a low branching ratio and two neutrinos in the final state, which makes the reconstruction of the $t\bar{t}$ invariant mass impossible. The semi-leptonic channel (a), where one W boson decays hadronically and the other one leptonically, has a significant branching ratio and a lower background than the totally hadronic mode, and it is thus considered the best channel for discovering heavy resonances decaying to $t\bar{t}$ [63]. To identify the decay in this channel, one needs to detect an isolated charged lepton, missing transverse momentum and at least four jets [64].

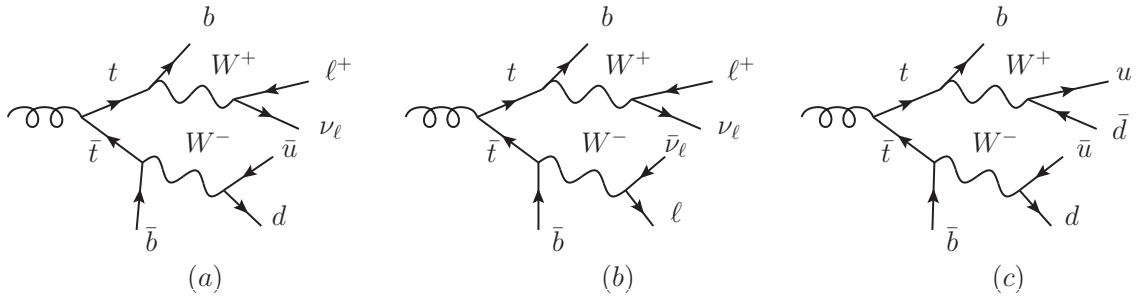

Figure 4.3: Semi-leptonic (a), leptonic (b) and totally hadronic (c) decay of a $t\bar{t}$ quark pair.

4.4 Heavy colored resonances

In beyond the Standard Model scenarios, more particles besides the SM gauge bosons can be involved in top quark pair production. Indeed, several models predict the existence of heavy colored resonances decaying to top quarks that might be observed at the LHC, like axigluons in chiral color models [65–67], colorons [68] or Kaluza Klein excitations in extra dimensional models [69–74]. Their existence modifies the $q\bar{q} \to t\bar{t}$ production cross-section, while gluon-gluon fusion to top quarks stays, at first order, unaltered, because a pair of gluons do not couple to a single extra resonance in this kind of models. For example, the asymmetric chiral color model [66] allows the existence of three axigluon vertices, which are forbidden in the usual chiral color model by parity [65], but exclude gluon-gluon-axigluon vertices as well. Models in extra warped dimensions, where KK modes can be single produced, have been constructed [72], but in the conventional and more extended extra dimensional models, a single KK gauge field does not couple to two SM gauge bosons at leading order by orthonormality of field profiles [69]. The new interaction between quarks

and the extra resonance reads:

$$\mathcal{L}_{\text{res.}} \equiv i g_s \bar{\psi}_q \gamma^\mu (g_V^q + g_A^q \gamma_5) R_\mu^a T_a \psi_q \,, \tag{4.5}$$

where, in the most general case, each quark with flavor q can couple with different strength to the colored massive resonance R^a. The kinetic term for the resonance field takes the form $-\frac{1}{4} R_a^{\mu\nu} R^a_{\mu\nu}$, where, as usual, $R^a_{\mu\nu} = \partial_\mu R^a_\nu - \partial_\nu R^a_\mu + g_s f^{abc} R^b_\mu R^c_\nu$.

Detecting such resonances with masses in the TeV region is not an easy task, because the top quarks are very energetic. This means that they are very boosted, thus their decay products are highly collimated. On one side, this makes the identification of the jets difficult, due to a high level of overlapping. On the other side, it is easier to misinterpret a b quark as a light quark, since the two vertices that are the characteristic signal of the b quark are very close to each other and they could be detected as a single jet [64].

The natural signature of these resonances is a peak in the invariant mass distribution of the top-antitop quark pair located at the mass of the new resonance. Colored resonances are fairly broad: $\Gamma_G/m_G = \mathcal{O}(\alpha_s) \sim 10\%$. Present lower bounds on their mass are about 1 TeV. The latest exclusion limit by CDF [76] at 95% C.L. is 260 GeV$< m_G <$ 1.250 TeV for axigluons and flavor-universal colorons (with $\cot\theta = 1$ mixing of the two $SU(3)$).

However, asymmetries can be an alternative way of revealing these resonances. Some of those exotic gauge bosons, such as the axigluons, might generate already at tree-level a charge asymmetry through the interference with the $q\bar{q} \to t\bar{t}$ SM amplitude [77–80]. In principle, one could guess that a charge asymmetry can be generated without introducing any resonance, and considering instead CP violating models where chromoelectric or chromomagnetic dipoles [81] are generated. In these models, the Lagrangian reads:

$$\mathcal{L} = -\frac{i}{2} d_{M(E)}) \bar{\psi}_t \sigma^{\mu\nu} (\gamma_5) \psi_t F_{\mu\nu}, \tag{4.6}$$

where $d_{M(E)}$ is the magnetic(electric) dipole moment and the γ_5 matrix is present in the chromoelectric case and is not in the chromomagnetic case. From (4.6) a gluon-gluon-quark-antiquark vertex is generated in addition to the $gq\bar{q}$:

$$d_{M(E)} f_{abc} \bar{\psi}_t \sigma^{\mu\nu} (\gamma_5) A^b_\mu A^c_\nu T^a \psi_t. \tag{4.7}$$

A charge asymmetry in theories with (chromo)electric(magnetic) dipole moments can be generated only for polarized beams and if the decay products are analyzed. Direct calculation for the charge asymmetry under consideration resulted in zero.

Let us now review briefly the basic features of the most representative models of heavy colored resonances decaying to top-antitop quark pair.

4.4.1 Top color models and colorons

These models extend the SM to an enlarged gauge group called topcolor group $SU(3)_h \otimes SU(3)_\ell$ that breaks to $SU(3)_{\text{color}}$ [82]. In top color models the third generation of quarks transforms under $SU(3)_h$ and the light quarks transform under $SU(3)_\ell$ [65, 67], while,

in coloron models, all quarks transform in the same way under both $SU(3)$ [68]. With the symmetry breaking, the particle spectrum is enriched with massive color-octet gauge bosons, called topgluons, that couple purely vectorially to the top quarks. In the top color case, these bosons couple preferentially with the top and bottom quarks, while in flavor universal coloron models they have the same coupling strength with all the flavours. Depending on the strength of the coupling, a condensate of two heavy quarks can be generated also.

A more complete formulation of the ideas that base these models is topcolor-assisted technicolor. Here the symmetry group is:

$$G_{TC} \otimes SU(3)_h \otimes SU(3)_\ell \otimes SU(2)_W \otimes U(1)_h \otimes U(1)_\ell \,, \tag{4.8}$$

which breaks to the low energy

$$G_{TC} \otimes SU(3)_{\text{color}} \otimes U(1)_{\text{e.m.}} \,, \tag{4.9}$$

where G_{TC} is the technicolor gauge group. The third generation of quarks couple preferentially to $SU(3)_h \otimes U(1)_h$, while the first and second ones to $SU(3)_\ell \otimes U(1)_\ell$. The symmetry breaking provides a mass for the coloron and the Z' which are the bosons responsible of carrying new interactions for the third generation doublet.

4.4.2 Chiral color models and axigluons

Another possible extension of the SM gauge group at higher energy is the gauge group $SU(3)_L \otimes SU(3)_R \otimes SU(2)_L \otimes U(1)_Y$ [67]. The chiral color group $SU(3)_L \otimes SU(3)_R$ is broken to the diagonal subgroup $SU(3)_{\text{color}}$. Originally, the scale at which both symmetry breakings occur, by the Higgs mechanism, has been proposed to be the same, around few hundreds GeV. A variety of new particles are predicted, according to the different models, but there is one important model-independent prediction: besides the W and the Z bosons, another color-octet massive gauge boson, electrically neutral, appears, with a mass similar to the electroweak gauge bosons and it is called axigluon. Indeed, its coupling with fermions is purely axial and the coupling strength is the same as QCD. In axigluon models a charge asymmetry is generated already at the tree level. In [77] a first analysis has been performed pointing out that the forward-backward asymmetry is more sensitive to larger values of the axigluon mass than the invariant mass distribution of the top quark pair.

4.4.3 Extra dimensional models

Extra dimensional models address the hierarchy problem, one of the still open questions in particle physics today, namely why the Planck unification scale and the electroweak scale are so different. Indeed, we have:

$$\frac{M_{\text{EW}}}{M_{\text{Pl.}}} \simeq 10^{-20} \,, \tag{4.10}$$

a very low number. Anyway, there are proposed models where the Planck scale is not the fundamental scale of gravity [70, 83].

The first in developing the idea of extra dimensions have been Kaluza and Klein [84] in the second decade of the last century. A five-dimensional space was proposed, where besides the four familiar dimensions of space-time, a new dimension was added, curled up in a circle. The size of this new dimension is very small, of the same order of magnitude as the Planck length scale, thus has not visible effects on the observable physics. The ground state of this space-time is thus $M^4 \times S^1$, where M^4 is the usual four dimensional Minkowski space and S^1 the circle. Small oscillations around the ground state generate a spectrum of massive excitations, called the Kaluza-Klein (KK) tower [85]. Their masses are inversely proportional to the S^1 radius. Also, a finite number of massless modes is found, among which is the spin-2 graviton. This theory has been neglected for a long time since it seemed not to have any realistic implementation, and has been studied only as a mathematical structure itself. Nevertheless, some of its phenomenological implications appear in subsequent models.

For instance, Arkani-Hamed, Dimopoulos and Dvali (ADD) [83] introduced n new compact dimensions in addition to the usual 4-dimension space-time. SM ordinary fields are confined to a 4-dimensional subspace, called 3-brane and are not influenced by these additional dimensions, which are compactified. Gravity, on the other hand, can propagate freely through the whole space (bulk). Kaluza-Klein gravitons are generated that couple with SM fields and can thus be detected. In these models, the Planck scale is related to another scale M, the fundamental one, through the volume of the compactified dimensions V_n:

$$M_{\mathrm{Pl.}} = V_n M^{2+n} \,. \tag{4.11}$$

The original suppression factor $1/M_{\mathrm{Pl.}}$ changes to $1/M$, that can be of the order of around TeV^{-1}, if the compactification volume is large enough. This factor allows these models to undergo phenomenological analyses. Indeed, upper bounds have already been set, getting $M \gtrsim 1$ TeV.

The ADD model, while eliminating the hierarchy problem between the Planck and the electroweak scale, however, introduces a new one between the compactification volume and M_{EW}. To solve this problem, Randall and Sundrum [70] proposed a new extra dimensional model (RS model), where there is no need to introduce a new scale. They proposed a 5-dimensional, non factorizable space, where the 4-dimensional metric is multiplied by an exponential factor depending on the compactification radius:

$$e^{-2kr_c\phi}\eta_{\mu\nu}dx^\mu dx^\nu + r_c^2 d\phi^2 \,. \tag{4.12}$$

Here, ϕ is the new extra dimension, that ranges from 0 to π and whose size is given by r_c, while k is a factor of the size of the Planck scale. To generate a large hierarchy a large r_c is not needed, due to the fact that the function is an exponential, thus varies very rapidly on r_c. The ratio between the 5-dimensional Planck scale and the inverse of the compactification radius is just $kr_c \simeq 50$, compared to the $(M_{\mathrm{Pl.}}/M)^{2/n} = (M_{\mathrm{Pl.}}/\mathrm{TeV})^{2/n}$ of

the ADD model. The Kaluza-Klein gravitons in the Randall-Sundrum model are predicted to have a mass around the TeV and couple with the SM fields with a suppression factor of the order of the TeV as well, thus the coupling is enhanced compared to the ADD model. Thus, these states could be generated as resonances and decay at a rate that can be observed at the LHC. In the original model, the SM fields can only propagate in the 4-dimensional space. However, models have followed, where they are allowed to live in the whole bulk [73]. This feature has various interesting implications like the suppression of flavour-changing neutral currents, the explanation of the fermion mass hierarchy or the gauge coupling unification. A consequence of these models is the existence of Kaluza-Klein excitations of the SM gauge bosons. In particular, KK gluons should have the largest coupling of all and thus be the first to be detected at the LHC. For masses above the $t\bar{t}$ threshold, the KK gluon decays mainly to a top-antitop quark pair, with a branching ratio depending on the model, while the couplings with the light quarks are suppressed in most bulk RS models.

4.5 The top quark charge asymmetry at hadron coliders

4.5.1 The charge asymmetry in QCD

QCD at tree level predicts that top-antitop quark pair production at hadron colliders is charge symmetric, namely the differential charge asymmetry, defined as:

$$A(\cos\theta) = \frac{N_t(\cos\theta) - N_{\bar{t}}(\cos\theta)}{N_t(\cos\theta) + N_{\bar{t}}(\cos\theta)} \tag{4.13}$$

vanishes for every value of θ. In (4.13), $N_{t(\bar{t})}(\cos\theta)$ is the number of top (antitop) quarks produced at a certain angle θ. Nevertheless, an asymmetry is generated at $\mathcal{O}(\alpha_s^3)$. The corrections to the cross section at this order, that generate such an asymmetry, are represented in Figs. 4.4 and 4.5. The asymmetry is given by two different kinds of contribution [86]: on one side, the radiative corrections given by the interference of final-state with initial-state bremsstrahlung (Fig. 4.4 $(d + f) \otimes (e + g)$) and the interference of the double virtual gluon exchange with the Born amplitude (Fig. 4.4 $a \otimes (b + c)$). On the other side, interferences between the different graphs of gluon-quark processes, whose amplitudes are shown in Fig. 4.5. In [86] it has been calculated that qg originated processes generate a contribution to the asymmetry much smaller than $q\bar{q}$, so it is possible to neglect them as far as the charge asymmetry is concerned. Finally, the gluon-gluon initiated process is obviously symmetric. The charge asymmetry coming from the real hard radiation has opposite sign compared to the soft and virtual corrections and the latter is always larger than the former. The soft gluon radiation generates an infrared singularity that is canceled exactly by the one emerging in the double gluon exchange. On the other hand, ultraviolet singularities are absent in the antisymmetric part of the double gluon exchange, as well as collinear singularities in the limit $m_q \to 0$, where m_q is the mass of the incoming light quark. This can be understood because such singularities could be canceled only by terms proportional to the lower order, but the lower order is symmetric.

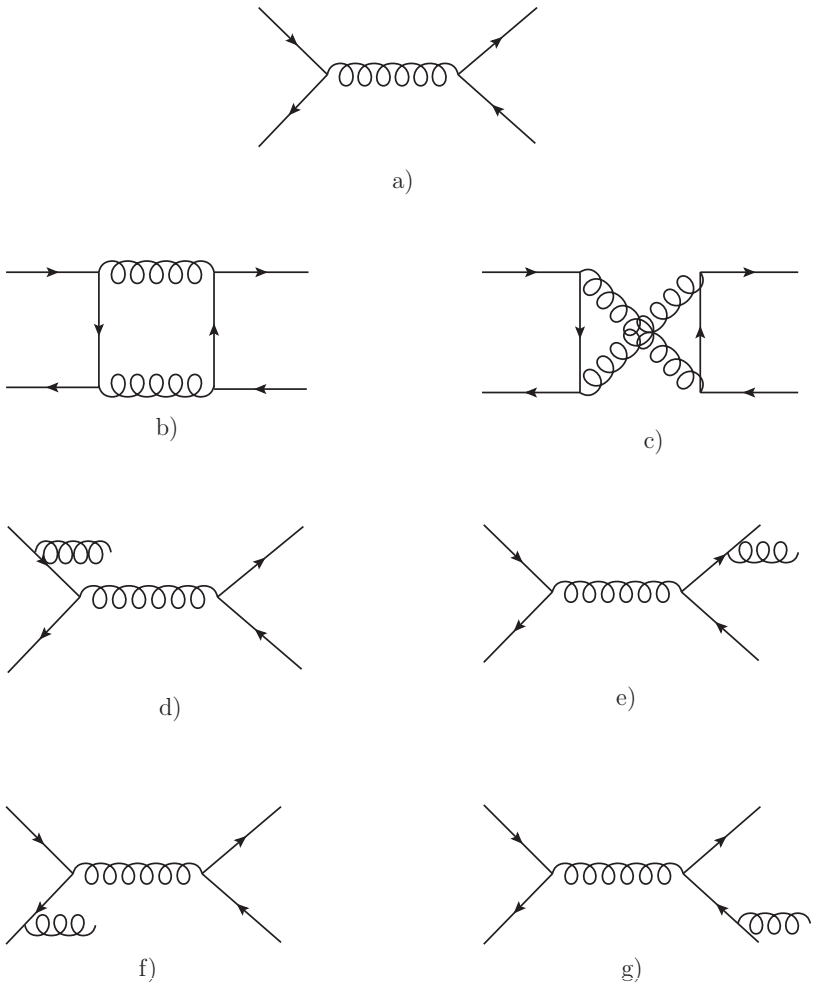

Figure 4.4: Graphs originated by $q\bar{q}$ that contribute to the QCD charge asymmetry in quark-antiquark production.

The way a charge asymmetry arises in QCD is analogous to what happens in Quantum Electrodynamics [87]. In a $e^+e^- \to \mu^+\mu^-$ annihilation, the cross section receives charge asymmetric contributions at $\mathcal{O}(\alpha^3_{\text{e.m.}})$ from the same amplitudes as the ones shown in Fig. 4.4 (where the gluon is replaced by a photon and the light and top quarks are replaced by electrons and muons respectively). The photon has charge conjugation $C = -1$. In the $a \otimes (b + c)$ and $(d + f) \otimes (e + g)$ interferences, an odd number of photons appears and a minus sign under charge conjugation results, thus leading to an asymmetry in the μ^+ and μ^- production. In QCD, the gluon has not a definite sign under charge conjugation and the above products of amplitudes contain both C-even and C-odd components.

The $a \otimes b$, $d \otimes e$ and $f \otimes e$ contributions (1) are related to the $a \otimes c$, $d \otimes g$ and $f \otimes g$ (2) respectively by:

$$\sigma_{(1)}(t, \bar{t}) = -\sigma_{(2)}(\bar{t}, t)\,, \tag{4.14}$$

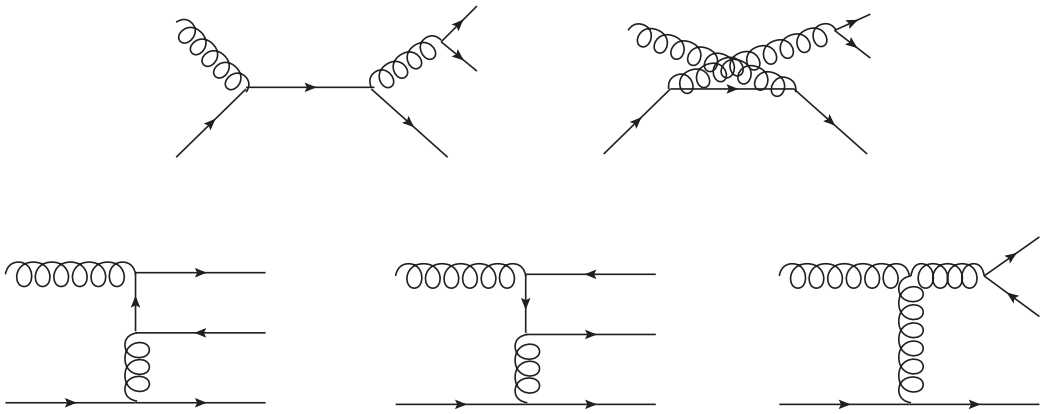

Figure 4.5: Graphs originated by qg that contribute to the QCD charge asymmetry in quark-antiquark production.

without taking into account the color factors. The color factors are:

$$\begin{aligned} C_1 &\propto d^2 + f^2 \\ C_2 &\propto d^2 - f^2 \,, \end{aligned} \tag{4.15}$$

where $d^2 \equiv d_{abc}d^{abc}$ and $f^2 \equiv f_{abc}f^{abc}$, so the asymmetry just selects the d^2 factor. This means that only color-singlet quark-antiquark configurations produce the asymmetry.

4.5.2 Experimental measurements and theoretical predictions

At partonic level, the top quark is emitted preferentially in the direction of the light incoming quark [86], so the partonic central asymmetry integrated in the forward region

$$\hat{A} = \frac{d\sigma_t(\cos\hat{\theta} \geq 0) - d\sigma_{\bar{t}}(\cos\hat{\theta} \geq 0)}{d\sigma_t(\cos\hat{\theta} \geq 0) + d\sigma_{\bar{t}}(\cos\hat{\theta} \geq 0)} \tag{4.16}$$

is positive. It can be seen that Eq. (4.16) is equivalent to the forward-backward asymmetry, defined as:

$$\hat{A}_{\mathrm{FB}} = \frac{d\sigma_t(\cos\hat{\theta} \geq 0) - d\sigma_t(\cos\hat{\theta} \leq 0)}{d\sigma_t(\cos\hat{\theta} \geq 0) + d\sigma_t(\cos\hat{\theta} \leq 0)} \,. \tag{4.17}$$

QCD is CP invariant, so, after performing a charge conjugation followed by a parity transformation, the physics should not change. As shown in Fig. 4.6, this implies the condition $d\sigma_t(\cos\theta) = d\sigma_{\bar{t}}(\cos(\pi - \theta))$.

The forward–backward asymmetry of top quarks has already been measured at the Tevatron proton-antiproton collider [88–90], at a center-of-mass energy of $\sqrt{s} = 1.96$ TeV.

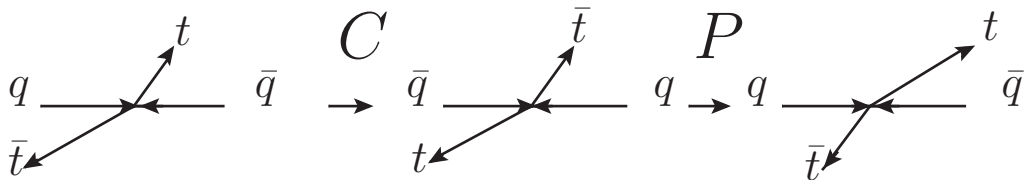

Figure 4.6: CP transformation of $q\bar{q} \to t\bar{t}$.

The CDF analyses provide the measurement in the lepton plus jets channel. The most recent value for the forward-backward asymmetry in the laboratory frame is [90]:

$$A_{\rm FB}^{p\bar{p}} = \frac{N_t(\cos\theta > 0) - N_t(\cos\theta < 0)}{N_t(\cos\theta > 0) + N_t(\cos\theta < 0)} = 0.193 \pm 0.065_{\rm stat.} \pm 0.024_{\rm syst.}\,, \tag{4.18}$$

where θ is the angle between the top quark and the proton beam. This value has been extracted with a luminosity of 3.2 fb^{-1} and has to be compared with the one year old result: $A^{p\bar{p}} = 0.17 \pm 0.07_{\rm stat.} \pm 0.04_{\rm syst.}$, with 1.9 fb^{-1} [88]. The uncertainty of both measurements is still large, but systematic errors have been improved considerably from one measurement to another, and statistical errors have decreased accordingly. Moreover, it turns out to be quite interesting that the uncertainty is still statistically dominated, and hence significant improvements should be expected in the near future.

The total charge asymmetry generated at the Tevatron by QCD at NLO has been calculated to be [77, 78]:

$$A = \frac{N_t(y \geq 0) - N_{\bar{t}}(y \geq 0)}{N_t(y \geq 0) + N_{\bar{t}}(y \geq 0)} = 0.051(6)\,, \tag{4.19}$$

In Eq. (4.19), y is the quark rapidity in the laboratory frame, defined as:

$$y = \frac{1}{2} \ln \frac{E + p_z}{E - p_z}\,, \tag{4.20}$$

where p_z is the momentum of the parton relative to the beam axis. The range of the rapidity is $(-\infty, \infty)$: $y = 0$ if $p_z = 0$, that corresponds to a $\pi/2$ angle with the beam and $y = \pm\infty$ for $p_z = \pm|p| = \pm E$ in the relativistic limit where the masses are set to zero. In a realistic analysis, a maximum value for the rapidity is taken not greater than a few units. It is worth to notice that the rapidity is positive in the forward direction, that is for $\theta \in (0, \pi/2)$ and negative in the backward direction, for $\theta \in (\pi/2, \pi)$.

The expressions for the different contributions to the differential cross section are listed in Appendix B.1. The value reported in Eq. (4.19) has been calculated using the LO for both the numerator and the denominator. However, the NLO corrections to the cross section are quite large, around 30% or even more [91], so, from a conservative point of view, an uncertainty of around 30% should be assigned to the asymmetry. Nevertheless,

the dominant corrections from collinear emission are expected to cancel [86]. The error is calculated taking into account different PDF sets and renormalization and factorization scales, as well as the error on the top quark mass. Prediction (4.19) for the inclusive charge asymmetry is robust with respect to the higher-order perturbative corrections generated by threshold resummation [92]. The forward–backward asymmetry of the exclusive process $p\bar{p} \to t\bar{t}+$ jet receives, however, large higher order corrections and is almost completely washed out at the Tevatron [93].

Comparing the theoretical prediction (4.19) with the experimental result (4.18), a discrepancy emerges of about two sigmas, that opens a window to the presence of new physics. Although it is too early to claim new physics there, because the statistical error of the measurement is rather large, it is possible to put constraints to some general parameters that appear in models with new physics. As expected, this result has boosted a renovated interest in looking for new models that would account for this effect [94–102].

4.5.3 The top quark charge asymmetry beyond the SM

As said in Section 4.4, there are models where the presence of a heavy colored resonance generates a charge asymmetry, that could, in principle, explain the discrepancy of the Tevatron measurements with the SM. This is, for instance, the case of the axigluon which has only axial-vector coupling with both light and top quarks.

We have studied, in a model independent way, heavy color-octet boson resonances decaying to $t\bar{t}$ with arbitrary vector and axial-vector couplings to quarks. In Appendix B.2 we list the differential cross sections in the presence of such a resonance. We have calculated the charge asymmetry generated in this toy model in the scenario of the current hadron colliders, namely the Tevatron and the LHC, in order to give reliable predictions about the possibility of measuring it in the next years. In Chapter 5 we present an analysis performed with the Tevatron parameters, that is reported in papers [103] and [104]. In Chapter 6 we evaluate the top quark charge asymmetry in a given finite interval of rapidities together with its statistical significance, according to the paper [104].

In the most popular models of warped extra dimensions, the Kaluza-Klein excitations of the gluon couple identically to the left-handed and the right-handed light quarks, and these couplings are different only for the third generation. A charge asymmetry cannot be generated in this kind of models by the production mechanism. An asymmetry will arise, however, in the decay products of the top quark. The polarization asymmetry from the angular distribution of the positron from the top quark decay has been investigated for example in [71]. However, the production of top quark pairs together with one jet can generate an asymmetry also in this kind of models. This motivates our study of $t\bar{t}$ + jet processes, reported in [105] and discussed in Chapter 6.

Chapter 5

Analysis at the Tevatron

5.1 Introduction

The Tevatron, located at the Fermi National Accelerator Laboratories, near Chicago, USA, is a proton-antiproton high energy collider. It has reached a center-of-mass energy of $\sqrt{s} = 1.96$ TeV and has been the world's highest energy machine before the LHC. The Tevatron has been running since 1985 and has hosted various experiments, among them CDF and D0 which discovered the top quark in 1995.

Figure 5.1: Air view of the Tevatron.

The maximum instantaneous luminosity $\mathscr{L}$ reached at the Tevatron has been 2.9×10^{32} cm^{-2} s^{-1} [106], where $\mathscr{L}$ is defined as the number of particles in the beam per unit area per unit time. The number of interactions of a physics process per unit of time dN/dt is given by the product of its total cross section and the instantaneous luminosity:

$$\frac{dN}{dt} = \mathscr{L}\sigma\,. \tag{5.1}$$

The instantaneous luminosity depends strongly on time, so often it is useful to use the integrated luminosity $\mathcal{L}$:

$$\mathcal{L} = \int \mathscr{L}\, dt\,, \tag{5.2}$$

that is related to the number of particles of the beam over a finite period of time. At the moment, the Tevatron has recorded 8 fb^{-1} of integrated luminosity and has analyzed about $3-4$ fb^{-1}.

5.2 Top quark charge asymmetries

At the Tevatron, most of the processes is initiated by $q\bar{q}$ collisions that generate a charge asymmetry, as we have seen in Chapter 4. Gluon-gluon fusion, which represents only 15% of all the events at the Tevatron, remains charge symmetric. Due to CP invariance, the charge asymmetry is equivalent to a forward–backward asymmetry.

The CDF analyses provide two different measurements in the lepton plus jets channel. The first measurement is made in the laboratory frame, and the most recent value is [90]:

$$A_{\rm FB}^{p\bar{p}} = \frac{N_t(\cos\theta > 0) - N_t(\cos\theta < 0)}{N_t(\cos\theta > 0) + N_t(\cos\theta < 0)} = 0.193 \pm 0.065_{\rm stat.} \pm 0.024_{\rm syst.}\,, \tag{5.3}$$

as shown in Section 4.5.2. The second measurement exploits the Lorentz invariance of the difference between the t and $\bar{t}$ rapidities, $\Delta y = y_t - y_{\bar{t}}$. Indeed, at LO it is related to the top quark production angle $\theta_{t\bar{t}}$ in the $t\bar{t}$ rest frame by [90]:

$$\Delta y = 2\tanh^{-1}\left(\beta\cos\theta_{t\bar{t}}\right)\ , \tag{5.4}$$

where $\beta = \sqrt{1-4m_t^2/\hat{s}}$ is the top quark velocity. So, the region $\Delta y \geq 0$ corresponds to $\cos\theta_{t\bar{t}} \geq 0$. Its value, with 1.9 fb^{-1} of data, is [88]:

$$A_{\rm FB}^{t\bar{t}} = \frac{N_{\rm ev.}(\Delta y > 0) - N_{\rm ev.}(\Delta y < 0)}{N_{\rm ev.}(\Delta y > 0) + N_{\rm ev.}(\Delta y < 0)} = 0.24 \pm 0.13_{\rm stat.} \pm 0.04_{\rm syst.}\ . \tag{5.5}$$

The corresponding theoretical predictions are [77]:

$$\mathcal{A} = \frac{N_t(y \geq 0) - N_{\bar{t}}(y \geq 0)}{N_t(y \geq 0) + N_{\bar{t}}(y \geq 0)} = 0.051(6)\ , \tag{5.6}$$

for the inclusive charge asymmetry, or forward–backward asymmetry ($\mathcal{A} = A_{\rm FB}^{p\bar{p}}$), and

$$\mathcal{A}_Y = \frac{\displaystyle\int dY (N_{\rm ev.}(y_t > y_{\bar{t}}) - N_{\rm ev.}(y_t < y_{\bar{t}}))}{\displaystyle\int dY (N_{\rm ev.}(y_t > y_{\bar{t}}) + N_{\rm ev.}(y_t < y_{\bar{t}}))} = 0.078(9)\ , \tag{5.7}$$

for the integrated pair asymmetry, which is defined through the average rapidity $Y = \frac{1}{2}(y_t + y_{\bar{t}})$. The differential pair asymmetry is almost flat in the average rapidity, and amounts to about 7% for any value of Y. The corresponding integrated asymmetry is equivalent to the integrated forward–backward asymmetry in the $t\bar{t}$ rest frame: $\mathcal{A}_Y = A_{\rm FB}^{t\bar{t}}$ and this is the reason why the pair asymmetry is larger than the forward–backward asymmetry. Indeed, events where both t and $\bar{t}$ are produced with positive or negative rapidities in the laboratory frame do not contribute to the integrated forward–backward asymmetry, while they do contribute to the pair asymmetry, because in the partonic frame t and $\bar{t}$ are always back-to-back, as shown in Fig. 5.2. The experimental measurements of the top quark asymmetry in Eq. (5.3) and Eq. (5.5), although still statistically dominated, disagree with the corresponding theoretical predictions in Eq. (5.6) and Eq. (5.7), respectively, by about 2σ. Thus, there is space for arguing the presence of new physics to account for this discrepancy.

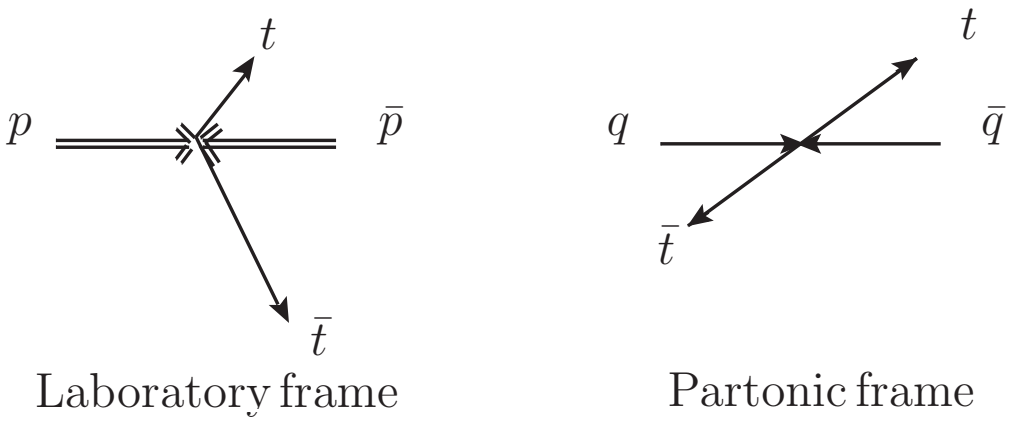

Figure 5.2: The forward–backward asymmetry is larger in the partonic frame than in the laboratory frame.

We shall consider in the following the production of heavy color-octet boson resonances decaying to top-antitop quark pairs with a non-vanishing axial-vector coupling to quarks. We shall not stick here to a particular model, but will analyze the most general scenario where the heavy resonance interacts with quarks with arbitrary vector g_V and axial-vector g_A strength relative to the strong coupling g_s. We also assume that there is no direct coupling of a single resonance to an even number of gluons, and therefore the production of top quarks is driven by $q\bar{q}$ events. This choice is motivated by different implementations of models predicting the existence of extra color-octet gauge bosons, as seen in the previous chapter. The Born differential cross section for $q\bar{q}$ annihilation in the presence of a color-octet vector resonance is given in Eq. (B.17) of Appendix B.2, that we report here for

convenience:

$$\begin{aligned}\frac{d\sigma^{q\bar{q}\to Q\bar{Q}}}{d\cos\hat{\theta}} &= \alpha_s^2\,\frac{T_F C_F}{N_c}\,\frac{\pi\beta}{2\hat{s}}\Bigg(1+c^2+4m^2+\\ &+ 2\hat{s}\,\mathrm{Re}\{G(\hat{s})\}\left[g_V^q\,g_V^t\,(1+c^2+4m^2)+2\,g_A^q\,g_A^t\,c\right]+\\ &+ \hat{s}^2\,|G(\hat{s})|^2\Bigg[\left((g_V^q)^2+(g_A^q)^2\right)\Bigg((g_V^t)^2(1+c^2+4m^2)+\\ &+ (g_A^t)^2(1+c^2-4m^2)\Bigg)+8\,g_V^q\,g_A^q\,g_V^t\,g_A^t\,c\Bigg]\Bigg)\,. \end{aligned} \tag{5.8}$$

The charge asymmetry is built up from the two contributions of (5.8) that are odd in the polar angle. The first one arises from the interference with the gluon amplitude, and is proportional to the product of the axial-vector couplings of the light and the top quarks. This contribution, provided that the product of the couplings is positive, is negative in the forward direction for invariant masses of the top-antitop quark pair below the resonance mass, and changes sign above. The second contribution, arising from the squared amplitude of the heavy resonance, although always positive for positive couplings, is suppressed with respect to the contribution of the interference term by two powers of the resonance mass. For large values of the couplings, however, the squared amplitude of the resonance might compensate the interference contribution, then leading to a positive forward–backward asymmetry, because it is enhanced by the product of the vector couplings. Indeed, for

$$\hat{s}=\bar{s}\equiv\frac{m_G^2}{1+2\,g_V^q\,g_V^t}\,, \tag{5.9}$$

the two odd terms cancel to each other, and above that value the contribution to the forward–backward asymmetry becomes positive.

To simplify our analysis we consider that the vector and axial-vector couplings, which are normalized to the strong coupling α_s, are flavour independent: $g_V^q = g_V^t = g_V$, and $g_A^q = g_A^t = g_A$, where q labels the coupling of the excited gluon to light quarks, and t to top quarks. The axigluon of chiral color theories [65, 75], for example, is given by $g_V = 0$ and $g_A = 1$. We study how the production cross section and the charge asymmetry vary depending on the vector and axial-vector couplings, which we take in the range $[0, 2]$. Within this range the perturbative expansion is still reliable. Moreover, in the flavour independent scenario the sign of the couplings is not relevant, since they always appear as squared.

Results for the difference between the production cross section in the presence of the resonance and the SM prediction in the (g_V, g_A) plane are presented in Fig. 5.3 for different values of the resonance mass between 1 and 2 TeV. In our analysis, we use the MRST 2004 parton distribution functions [107], and we set the renormalization and factorization scales to $\mu = m_t$, with $m_t = 170.9 \pm 1.1_{\,\mathrm{stat.}} \pm 1.5_{\,\mathrm{syst.}}$ GeV [108]. For comparison, we also overwrite in Fig. 5.3 the 1, 2 and 3 sigma contours obtained from the experimental measurement

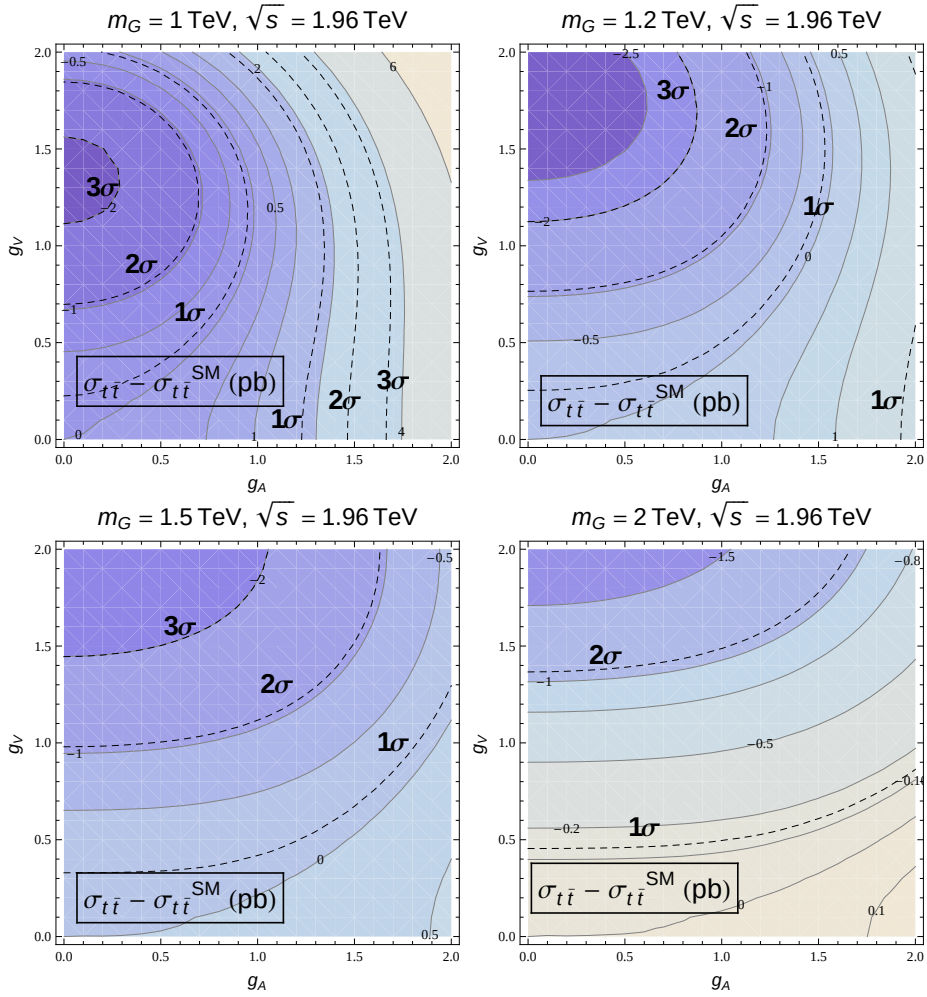

Figure 5.3: Top quark cross-section at the Tevatron in the bidimensional g_V-g_A plane for different values of the resonance mass.

$\sigma_{t\bar{t}}^{\text{exp.}} = 7.5 \pm 0.48$ (pb) [109], and the SM prediction $\sigma_{t\bar{t}}^{\text{NLO}} = 6.7 \pm 0.8$ (pb) [110]. The difference between the cross sections is thus:

$$\sigma_{t\bar{t}}^{\text{exp.}} - \sigma_{t\bar{t}}^{\text{NLO}} = 0.8 \pm 0.93 \text{ pb} \tag{5.10}$$

where the standard deviation has been calculated by summing the squared errors. Similar plots are presented in Figs. 5.4 and 5.5 for the forward–backward asymmetry and the pair asymmetry, respectively. The sigma contours are calculated from the difference between the experimental measurement in Eq. (5.3) and the theoretical prediction in Eq. (5.6) for the forward–backward asymmetry, and between Eq. (5.5) and Eq. (5.7) for the pair asymmetry. At 90% C.L. the plots of the production cross section and the asymmetries exclude complementary regions of the parameter space. While the production cross section excludes the corner with large vector couplings g_V and low axial-vector coupling g_A, the

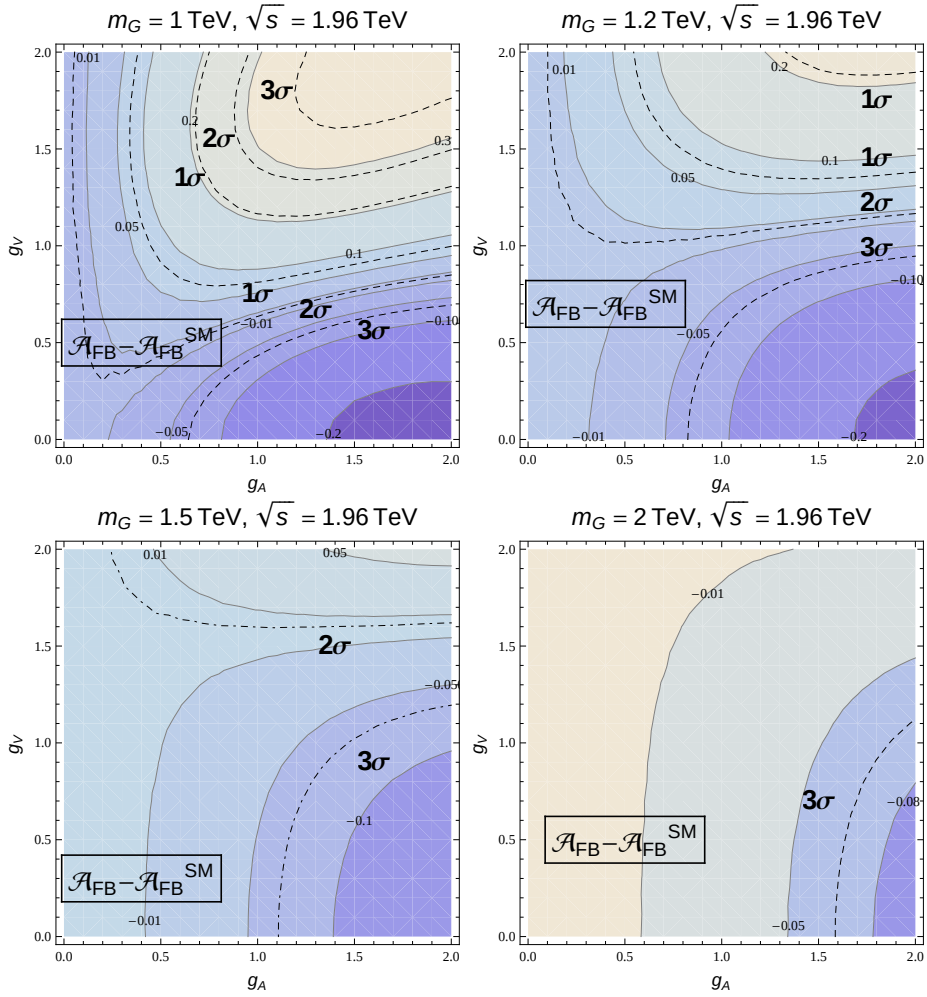

Figure 5.4: Forward–backward asymmetry at the Tevatron in the bidimensional g_V-g_A plane for different values of the resonance mass.

forward–backward and the pair asymmetry exclude the corners with higher axial-vector couplings and either low or high vector couplings. This is not surprising, because the terms of the differential cross section in Eq. (5.8) that are even in the polar angle contribute exclusively to the integrated cross section, while the odd terms contribute to the charge asymmetry only, and they are proportional to different combinations of the vector and axial-vector couplings. The exclusion regions are, as expected, smaller for higher values of the resonance mass, because a high mass suppresses all the contributions beyond the SM.

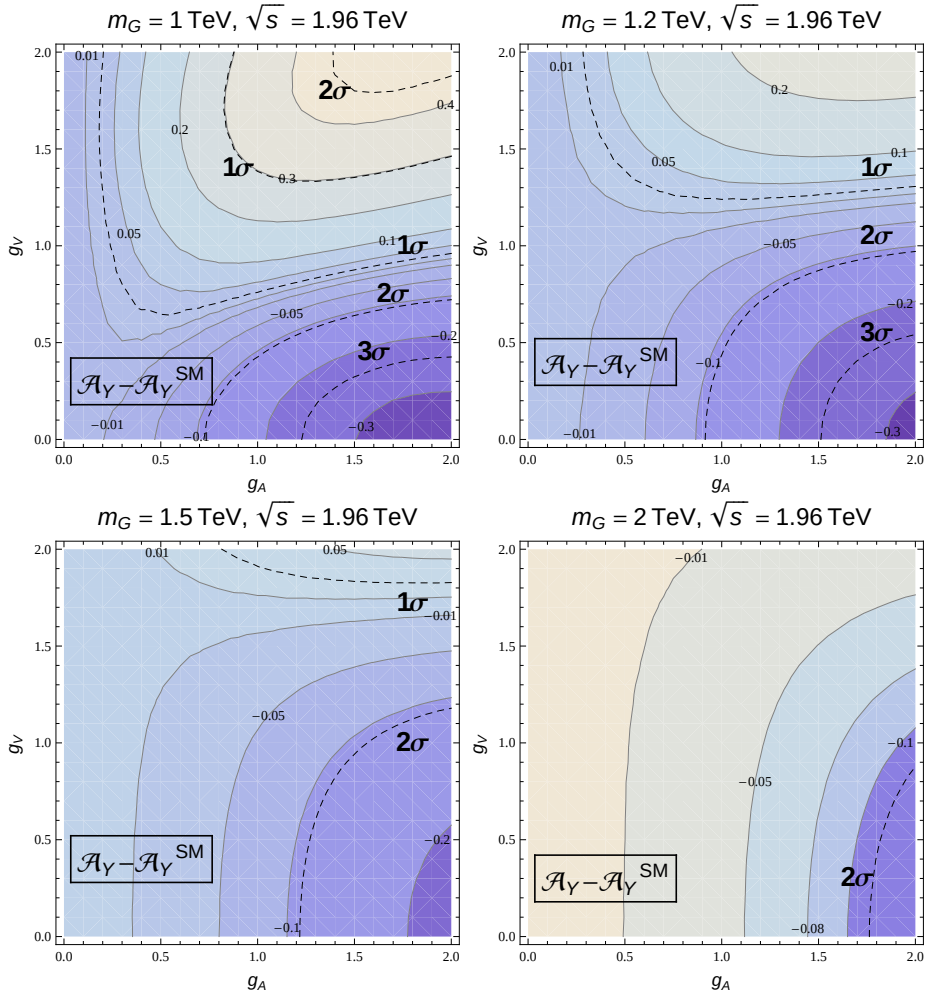

Figure 5.5: Pair asymmetry at the Tevatron in the bidimensional g_V-g_A plane for different values of the resonance mass.

5.3 Constraining heavy colored resonances

So far, we have considered sigma contours on the total cross section and the asymmetries in order to constrain the parameter plane (g_A, g_V). Comparing Eq. (5.6) with Eq. (5.3), we can deduce that heavy resonances giving rise to a vanishing or negative charge asymmetry are disfavored at 2σ. This is the case of colorons ($g_A = 0$) and normal axigluons ($g_V = 0, g_A = 1$), as we show in Fig. 5.6. At 3σ one can also exclude, for instance, axigluon masses below 1.4 TeV.

We explore whether it is still possible to reconcile this kind of resonances, such as the axigluon, with the measurement of the charge asymmetry. A positive asymmetry can be generated if the term from the squared amplitude of the massive color-octet in Eq. (5.8), which is proportional to $8 g_V^q g_A^q g_V^t g_A^t c$, dominates over the term of the interference, that is

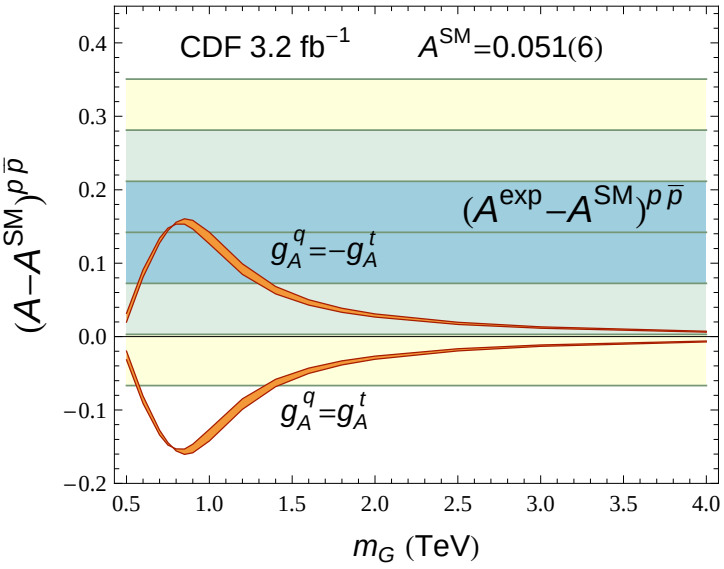

Figure 5.6: Comparison of the axigluon contribution to the top quark charge asymmetry with the 1σ, 2σ, and 3σ contours as a function of the axigluon mass. We also consider the case $g_A^q = -g_A^t = 1$.

proportional to $2g_A^q g_A^t c$. This is possible if the vector couplings are large enough, as can be seen in Fig. 5.4. However, although the total cross section might still be compatible with the SM prediction in that case, because the contribution of the excited gluon is suppressed by powers of its mass, the top-antitop quark invariant mass distribution might be enhanced considerably, due to the factor

$$\left((g_V^q)^2 + (g_A^q)^2\right)\left((g_V^t)^2 + (g_A^t)^2\right) \ , \tag{5.11}$$

particularly for high values of the top-antitop quark invariant mass.

In [59], the differential distribution in the invariant top-antitop quark mass is presented. The measurement is done with 2.7 fb^{-1} of integrated luminosity and the histogram is shown in Fig. 5.7. The invariant mass is divided in nine bins and the last one

$$\begin{aligned} \frac{d\sigma}{dM_{t\bar{t}}}(0.8-1.4 \text{ TeV}) &= 0.068 \pm 0.032_{\text{stat.}} \pm 0.015_{\text{syst.}} \pm 0.004_{\text{lumi.}} = \\ &= 0.068 \pm 0.036 \text{ (fb GeV}^{-1}) \end{aligned} \tag{5.12}$$

is the most sensible to extra contributions beyond the SM at the TeV scale.

As done before with the total cross section, we now subtract the experimental value of the top-antitop quark invariant mass distribution in the interval 800 GeV$< M_{t\bar{t}} <$ 1.4 TeV (Eq. (5.12)) and the theoretical QCD prediction. As a first approximation, we take $\sigma_{\text{NLO}}^{\text{SM}} \simeq \sigma^{\text{exp}}$ with no error. Within 1σ the invariant mass distribution in that bin is

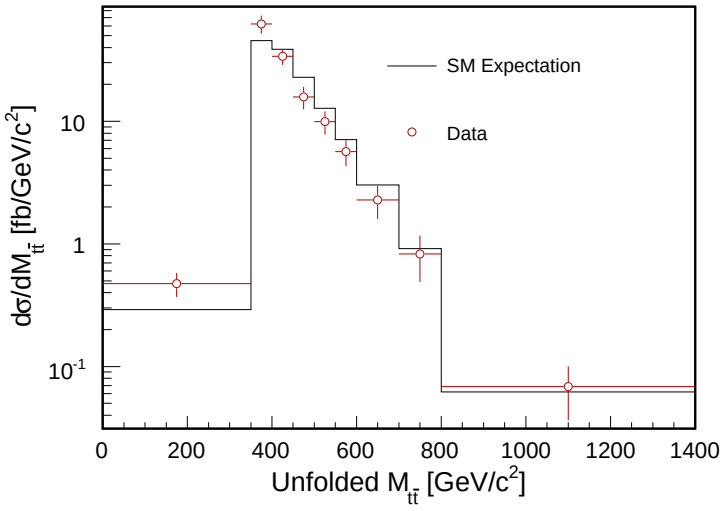

Figure 5.7: $d\sigma/dM_{t\bar{t}}$ measured at the Tevatron with 2.7 fb^{-1} [59].

thus enhanced by 50%. The charge asymmetry and the invariant mass distribution probe different combinations of the vector and axial-vector couplings; therefore, by combining both limits, one can constrain complementary regions of the parameter space.

Our results are shown in Fig. 5.8, where, for a given value of the mass of the color-octet resonance, we provide the allowed region at 95% C.L. in the $g_V - g_A$ plane. The solid lines are obtained from the charge asymmetry, while the dashed lines are derived from the last bin of the invariant mass distribution. The allowed regions are quite constrained; indeed at 90% C.L., we do not find any overlapping region for any value of the color-octet mass, and future experimental measurements with higher statistics can shrink significantly, or even exclude completely the allowed regions at 95% C.L.. With the most recent experimental values we find, in particular, that the asymmetric chiral color model ($g_V = \cot 2\theta, g_A = 1/\sin 2\theta$, or $g_V = \sqrt{g_A^2 - 1}$) is disfavored.

Another possibility to generate a positive charge asymmetry is to couple the third generation of quarks and the lighter quarks with axial-vector couplings of opposite sign: sign $(g_A^q) = -$sign (g_A^t). From Eq. (5.8) it is obvious that the actual sign of these couplings is irrelevant; only their relative sign is important because the asymmetric contributions to the differential cross section are proportional to their product. Chiral color models with nonuniversal flavor couplings were already considered in the pioneering works [65]. Our approach here is purely phenomenological, and building a realistic model in that scenario is beyond the scope of this work. The results for the axigluon case with $g_A^q = -g_A^t = 1$ are presented in Fig. 5.6. That scenario is compatible with the experimental data for any mass within 2σ. The most general case is shown in Fig. 5.9. From Fig. 5.9 and for $|g_A| < 2$, we find that, independently of the resonance mass, the region about

$$(|g_A| - 2.3)^2 + |g_V|^2 \gtrsim 1.8^2 \tag{5.13}$$

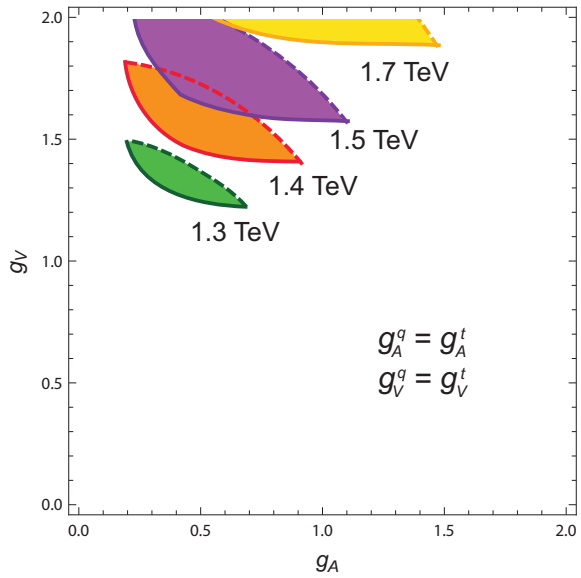

Figure 5.8: Contours at 95% C.L. as a function of the vector and axial-vector couplings for different values of the resonance mass for flavor-universal couplings.

is excluded at 90% C.L. Furthermore, for fixed values of the vector and axial-vector couplings, the charge asymmetry sets a lower limit on the mass of the color-octet, while an upper bound can be set thanks to the invariant mass distribution, e.g. for $|g_A| = 1$, we find that at 90% C.L.

$$1.33 \text{ TeV} < m_G < 2 \text{ TeV} \ . \tag{5.14}$$

Finally, we have also considered the case $g_V^q = -g_V^t$ and $g_A^q = -g_A^t$. Our results are presented in Fig. 5.10. Obviously, for $g_V = 0$, we obtain the same result as in Fig. 5.9.

5.4 Summary

In this chapter, we have analyzed the charge asymmetry in a top-antitop quark pair production at the Tevatron through the exchange of a color-octet heavy boson. We have first examined the case of flavour independent couplings, studying different observables. We have found that the total cross section on one side and the forward-backward asymmetry in the laboratory frame and the pair asymmetry on the other side, exclude complementary corners of the parameter space. This is reasonable, since the cross section and the asymmetries depend on different combination of the parameters. With the most recent measurement at the Tevatron, it becomes quite clear that a negative charge asymmetry is excluded within 2σ. Moreover, even if the total cross section remains unchanged in the presence of a heavy resonance, the differential distribution in the top-antitop quark invariant mass can be affected significantly, particularly for high values of the invariant mass.

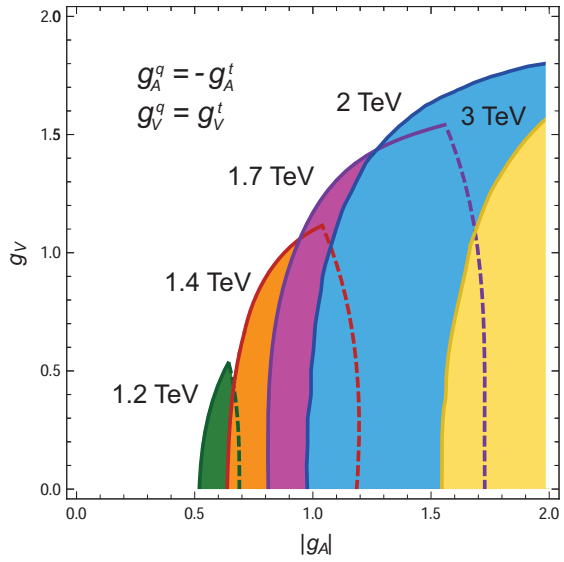

Figure 5.9: Contours at 90% C.L. as a function of the vector and axial-vector couplings for different values of the resonance mass and $g_A^q = -g_A^t$.

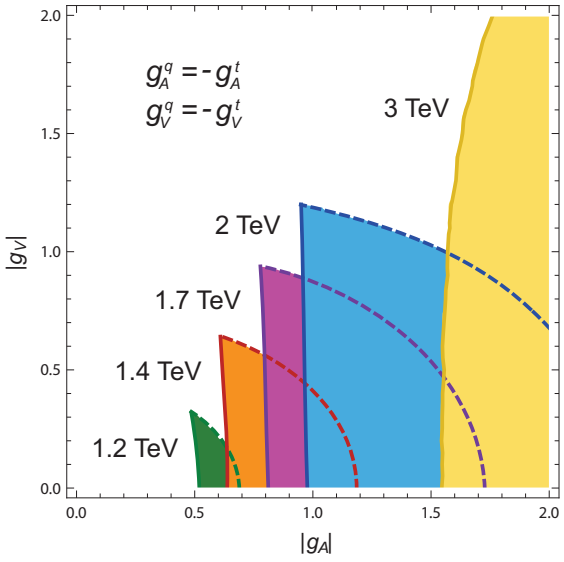

Figure 5.10: Contours at 90% C.L. as a function of the vector and axial-vector couplings for different values of the resonance mass and $g_V^q = -g_V^t$, $g_A^q = -g_A^t$.

For this reason, we have combined the measurement of the asymmetry and the last bin of the differential distribution of the top pair invariant mass to constrain the parameter space. We have found that in the flavor universal scenario the constraint is large, because the most recent measurements disfavor at 2σ vanishing or negative values of the charge asymmetry. In the flavor nonuniversal case, it is still possible to reconcile the experimental data with the existence of such resonances, and already a significant region of the parameter space can be excluded. Similar analyses have also been performed recently in warped extra dimensional models [98] and in the asymmetric chiral color model [96]. In view of the significant progress over the last year from the experimental side, we expect that new results from the Tevatron will further constrain efficiently the parameter space even before the start of the LHC, which is the natural place to discover those heavy resonances.

Chapter 6

Charge asymmetries at the LHC

6.1 Introduction

The LHC is the optimal environment to perform top quark measurements, due to its high center-of-mass energy (14 TeV at full activity). At the LHC a great amount of top-antitop quark pairs will be produced, thus allowing to develop analyses with high statistic. The full luminosity design is $\mathscr{L} = 10^{34}\,\mathrm{cm}^{-2}\,\mathrm{s}^{-1}$ (equivalent to $100\,\mathrm{fb}^{-1}$/year integrated luminosity). Since the production cross section of top-antitop quark pairs at the LHC is about 950 pb at 14 TeV [111], the LHC will produce millions of top-antitop quark pairs at full regime. This will allow not only to measure better some of the properties of the top quark, such as mass and cross section, but also to explore with unprecedented huge statistics the existence of new physics at the TeV energy scale in the top quark sector. After a successful start up, in September 2008, the machine went through a one-year stop and the energies initially scheduled had to be replanned. The first collisions have already been detected in December 2009, with a centre-of-mass energy of up to $\sqrt{s} \sim 2.36$ TeV , before the winter break and the first paper has already been published by the CMS collaboration [113]. The running schedule approved in January 2010 [112] plans an operation centre–of–mass energy of 7 TeV for the next 18 to 24 months, to which a one-year stop will follow. It is necessary in order to prepare and update the machine so that the 14 TeV full regime energy can be reached.

6.2 QCD induced charge asymmetry

Top quark production at the LHC is forward–backward symmetric in the laboratory frame as a consequence of the symmetric colliding proton-proton initial state. The charge asymmetry can be studied nevertheless by selecting appropriately chosen kinematic regions. The production cross section of top quarks is, however, dominated by gluon-gluon fusion, thus the charge asymmetry generated from the $q\bar{q}$ and gq ($g\bar{q}$) reactions is small in most of the kinematic phase-space. Indeed, while at the Tevatron the amount of top quarks produced through gg fusion is around 15% and through $q\bar{q}$ annihilation is the 85%, at the

LHC the situation is the opposite: gluon gluon fusion represents the 84% of the top quark production at 10 TeV and the 90% at 14 TeV.

Nonetheless, QCD predicts at the LHC a slight preference for centrally produced antitop quarks, with top quarks more abundant at very large positive and negative rapidities [86]. The difference between the single particle inclusive distributions of t and $\bar{t}$ quarks can be understood easily. Due to the proton composition in terms of quarks, production of $t\bar{t}(g)$ is dominated by initial quarks with large momentum fraction and antiquarks with small momentum fraction. QCD predicts that top (antitop) quarks are preferentially emitted in the direction of the incoming quarks (antiquarks) in the partonic rest frame as shown in Fig. 6.1 (left graphs). The boost into the laboratory frame "squeezes" the top quark mainly in the forward and backward directions, while antitop quarks are left more abundant in the central region (see Fig. 6.1 right graphs).

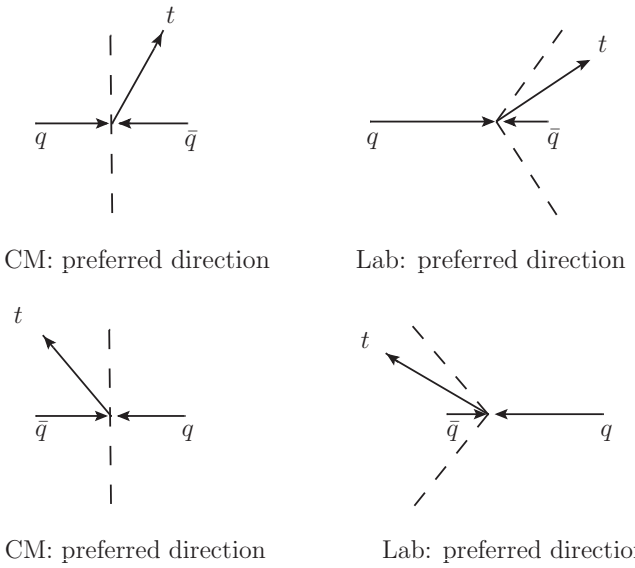

Figure 6.1: Boost from the center-of-mass quark–antiquark reference frame to the laboratory frame.

So, it is possible to select events in a given range of rapidity and define the integrated charge asymmetry in the central region as [77]:

$$A_C(y_C) = \frac{N_t(|y| \leq y_C) - N_{\bar{t}}(|y| \leq y_C)}{N_t(|y| \leq y_C) + N_{\bar{t}}(|y| \leq y_C)} \,. \tag{6.1}$$

The central asymmetry $A_C(y_C)$ obviously vanishes if the whole rapidity spectrum is integrated, while a non-vanishing asymmetry can be obtained over a finite interval of rapidity. It is worth noticing that this asymmetry does not arise from any CP violating effect, but it is due to a restriction in the phase space. According to what said above, a positive partonic asymmetry translates into a negative central asymmetry: an abundance of top quarks in

the forward direction in the partonic cross section means that more antitop quarks are left in the central region in the laboratory frame.

To enhance the asymmetry defined in Eq. (6.1), it is useful to perform a cut on the invariant mass of the top-antitop quark pair, $m_{t\bar{t}} > m_{t\bar{t}}^{\min}$, because that region of the phase space is more sensitive to the quark-antiquark induced events rather than the gluon-gluon ones. The reason is the behaviour of the parton distribution functions of the gluon and the light quarks: the gluon PDF is much higher than the quark ones for low momentum fractions, while decreases abruptly with the increasing of x, as shown in Fig. 6.2.

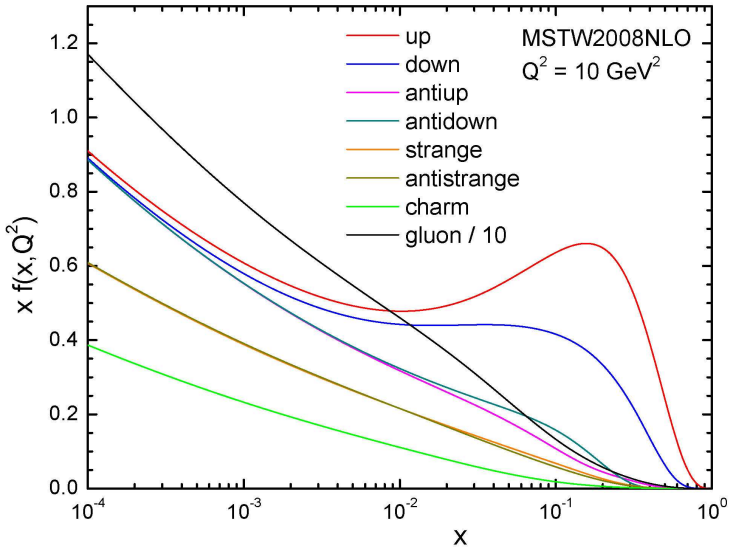

Figure 6.2: Parton distribution functions dependence on the momentum fraction x [114].

In Fig. 6.3 (left plots) we show the central charge asymmetry at $\sqrt{s} = 7$ TeV and 14 TeV as a function of the maximum rapidity y_C. Our aim is to determine the best value for the central rapidity. We have chosen two different values of the cut on the invariant mass of the top-antitop quark pair $m_{t\bar{t}} > 500$ GeV, and 1 TeV, in order to compare the size of the asymmetry in the two cases. As expected, the central charge asymmetry is negative, is larger for larger values of the cut $m_{t\bar{t}}^{\min}$, and vanishes for large values of y_C. In Fig. 6.3 (right plots) we also show the corresponding statistical significance $\mathcal{S}$ of the measurement. The statistical significance of an observable A is defined as the number of standard deviations σ_A of which A differs from zero:

$$\mathcal{S} = \frac{A}{\sigma_A}\,. \tag{6.2}$$

In a counting measure, the error of a measure N is $\sqrt{N}$, according to a Poisson statistic. Thus, using the error propagation and the definition of the asymmetry in Eq. (6.1), after

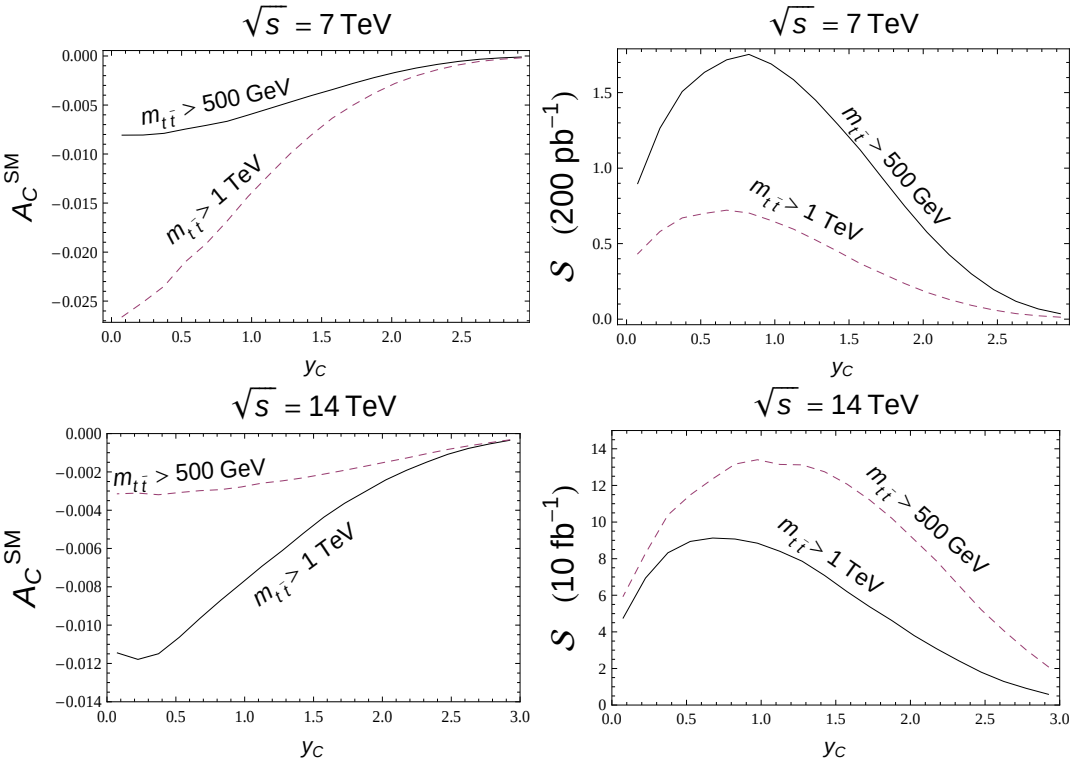

Figure 6.3: Central charge asymmetry at LHC as predicted by QCD, as a function of the maximum rapidity y_C (left plots), and corresponding statistical significance (right plots), for two different cuts on the top-antitop quark pair invariant mass.

a few algebraic manipulations, we find:

$$\sigma_{A_C} = \frac{1}{N_t + N_{\bar{t}}} \sqrt{1 - A_C^2}\,. \tag{6.3}$$

Since $N_t + N_{\bar{t}} = (\sigma_t + \sigma_{\bar{t}})L$ from the definition of luminosity, the expression for the statistical significance is:

$$\mathcal{S}^{\rm SM} \simeq A_C^{\rm SM} \sqrt{(\sigma_t + \sigma_{\bar{t}})^{\rm SM}\,\mathcal{L}} = \frac{N_t - N_{\bar{t}}}{\sqrt{N_t + N_{\bar{t}}}}\,, \tag{6.4}$$

where $\mathcal{L}$ denotes the total integrated luminosity for which we take $L = 200$ pb^{-1} at $\sqrt{s} = 7$ TeV and $L = 10$ fb^{-1} at $\sqrt{s} = 14$ TeV, according to the current schedule of the LHC. The maximum significance is reached for both running energies at $y_C = 1$ for $m_{t\bar{t}} > 500$ GeV, and $y_C = 0.7$ for $m_{t\bar{t}} > 1$ TeV. Surprisingly, although the size of the asymmetry is greater for the larger value of $m_{t\bar{t}}^{\rm min}$, its statistical significance is higher for the lower cut. This is a very interesting feature because softer top and antitop quarks should then be identified more easily than the very highly boosted ones.

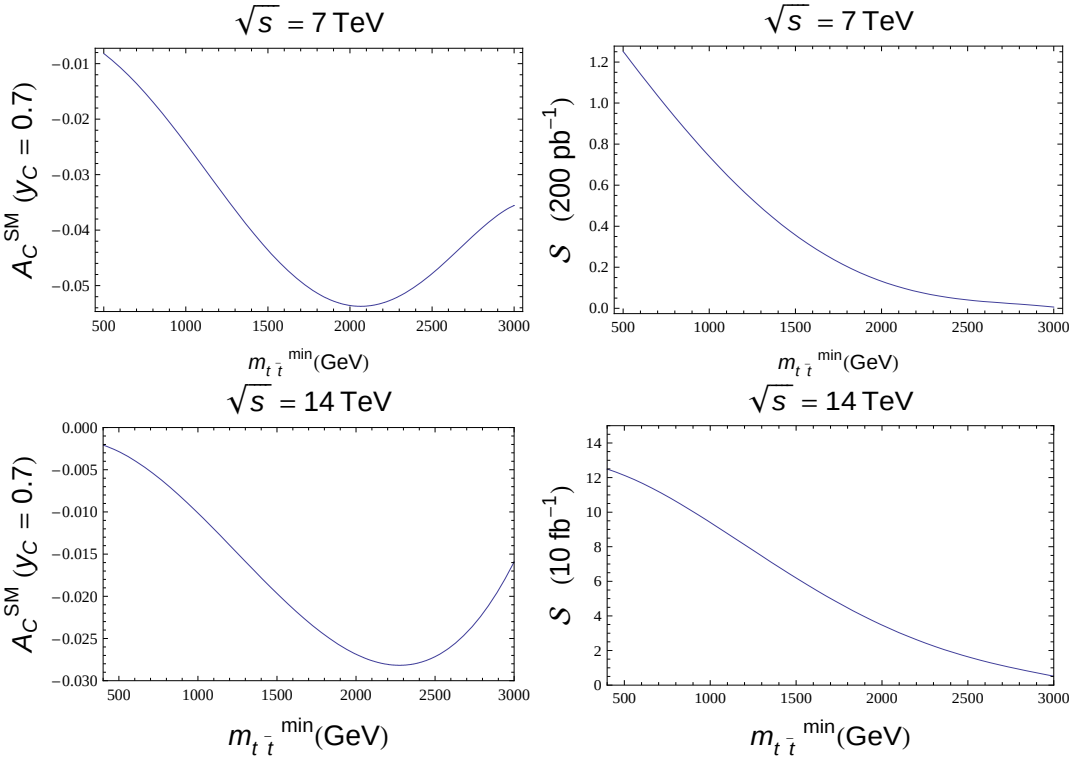

Figure 6.4: Central charge asymmetry and statistical significance at LHC from QCD, as a function of the cut $m_{t\bar{t}}^{\min}$, for 7 TeV and 14 TeV energy.

We now fix the value of the maximum rapidity at $y_C = 0.7$ and study the size of the asymmetry and its statistical significance as a function of $m_{t\bar{t}}^{\min}$. Our results are shown in Fig. 6.4 for $\sqrt{s} = 7$ TeV and $\mathcal{L} = 200$ pb^{-1} and $\sqrt{s} = 14$ TeV and $\mathcal{L} = 10$ fb^{-1}. In all cases, the asymmetry increases for larger values of $m_{t\bar{t}}^{\min}$, while the statistical significance is larger without introducing any selection cut. Note that the size of the asymmetry decreases again above $m_{t\bar{t}}^{\min} = 2.5$ TeV because in that region the $gq(\bar{q})$ events compensate the asymmetry generated by the $q\bar{q}$ events; their contributions are of opposite sign. We should point out that the values of the significance found here do not take into account experimental factors such as detector efficiencies. Moreover, top detection is carried out through the decay products. Since the semileptonic channel is considered the most suitable decay channel, top reconstruction is often performed only through it, in which case one expects to have the significance be reduced roughly to one third. Nevertheless, considering these caveat, we can conclude that, whereas with 200 pb^{-1} and 7 TeV of energy the significance is rather low, 10 fb^{-1} of data at the design energy of the LHC seems to be enough for a clear measurement of the QCD asymmetry.

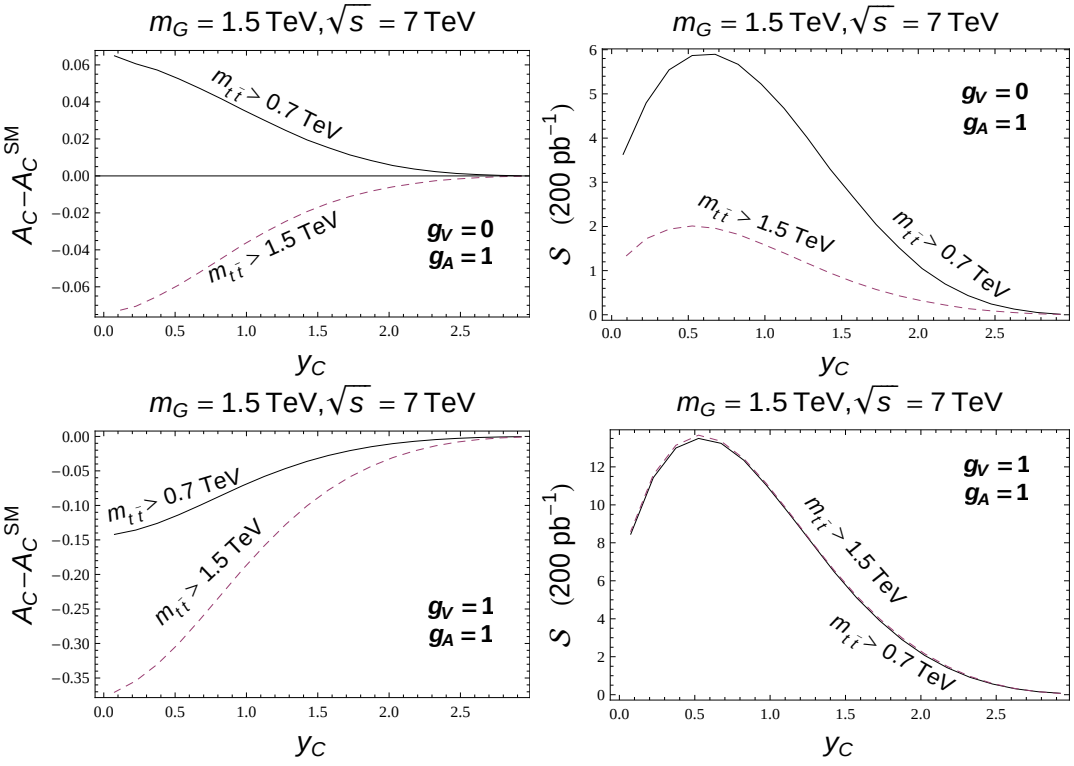

Figure 6.5: Central charge asymmetry (left plots) and statistical significance (right plots) at LHC as a function of the maximum rapidity, for 7 TeV energy and two different cuts on the top-antitop quark invariant mass. Two different sets of couplings are shown.

6.3 Charge asymmetry of color-octet resonances

Like for the Tevatron in Section 5.2, we study here the charge asymmetry produced at the LHC by the decay of a color-octet resonance to top quarks, in the scenario where the vector $g_V^{q(t)}$ and axial-vector $g_A^{q(t)}$ couplings are flavour independent. We evaluate the central asymmetry in Eq. (6.1), and its statistical significance

$$\mathcal{S}^{\rm G} = \frac{A_C^{\rm G+SM} - A_C^{\rm SM}}{\sqrt{1-(A_C^{\rm SM})^2}} \sqrt{(\sigma_t + \sigma_{\bar{t}})^{\rm SM}\, \mathcal{L}} \simeq \frac{(N_t - N_{\bar{t}})^{\rm G+SM}}{\sqrt{(N_t + N_{\bar{t}})^{\rm G+SM}}} \,, \tag{6.5}$$

for different values of the couplings and the kinematical cuts. In Eq. (6.5), the label G+SM on an observable means that such an observable is evaluated in a theoretical framework where the color-octet resonance is present. Eq. (6.5) is obtained assuming $(N_t + N_{\bar{t}})^{\rm SM} \simeq (N_t + N_{\bar{t}})^{\rm G+SM}$. As in the Tevatron analysis, we use here the MRST 2004 parton distribution functions, and again we set the renormalization and factorization scales to $\mu = m_t$, with the updated value $m_t = 173.9 \pm 0.6_{\,\rm stat.} \pm 1.1_{\,\rm syst.}$ GeV [57].

When a heavy color-octet boson resonance is produced, considerations similar to those in Section 5.2 lead to predict a positive central asymmetry for values of the cut in the

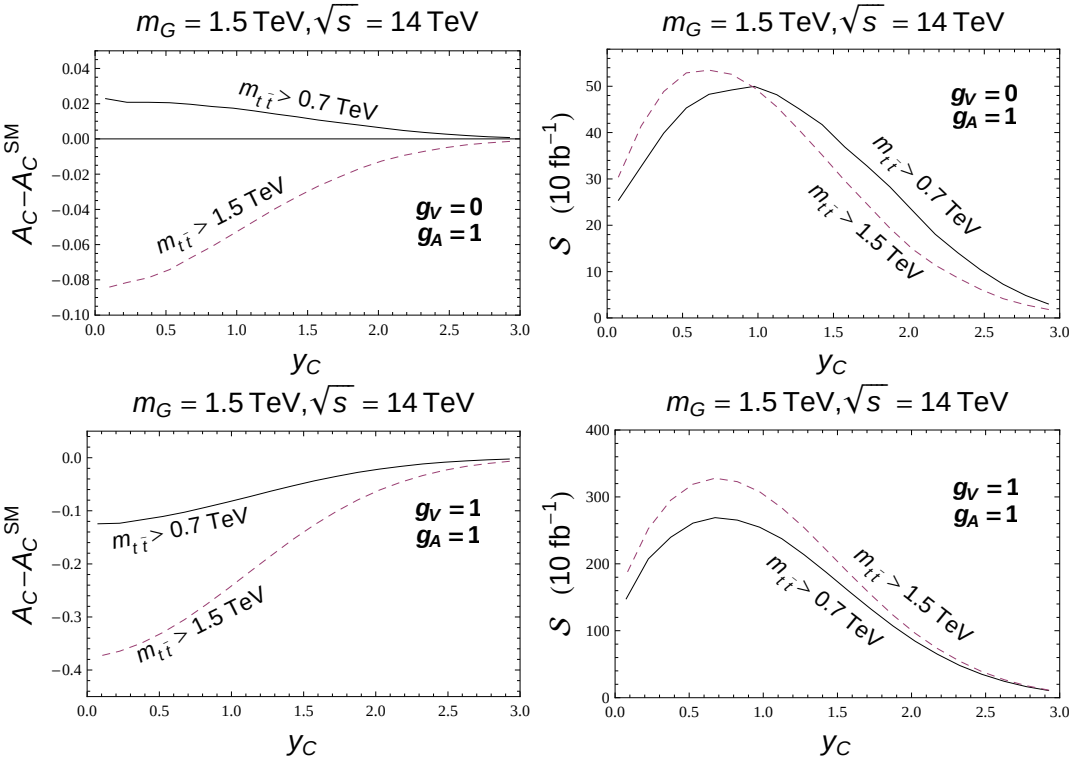

Figure 6.6: Central charge asymmetry (left plots) and statistical significance (right plots) at LHC as a function of the maximum rapidity, for 14 TeV energy and two different cuts on the top-antitop quark invariant mass. Two different sets of couplings are shown.

invariant mass of the top-antitop quark pair below the mass of the resonance and a negative asymmetry above. This is true as far as the interference term has a greater relevance than the squared amplitude of the exotic resonance. If this is the case, a higher number of antitop quarks will be emitted in the direction of the incoming quarks, and once the boost into the laboratory frame is performed (cf. discussion in Section 6.2), a higher number of top quark will be found in the central region, so that the central asymmetry is positive. Since for high values of the cut the sign of the interference term changes, the asymmetry will become negative, and then it has to vanish at a certain intermediate value of that cut, close and below the resonance mass.

In our first analysis we shall determine the value of the maximum rapidity y_C that maximizes the statistical significance. We fix the resonance mass at 1.5 TeV, and impose two different cuts on the invariant mass of the top-antitop quark pair, namely $m_{t\bar{t}} > 700$ GeV and $m_{t\bar{t}} > 1.5$ TeV. We choose two different combinations of the vector and axial-vector couplings g_V and g_A. In Figs. 6.5 and 6.6, we present the results obtained for the central asymmetry and the statistical significance for $g_V = 0$, $g_A = 1$ and $g_V = g_A = 1$ for two values of the centre-of-mass energy, 7 and 14 TeV, respectively. We notice that for the first choice of the parameters, namely $g_V = 0$, $g_A = 1$, the central asymmetry suffers

a change of sign by passing from the lower cut to the higher one. This means that it will vanish for a given value of the cut, thus making the statistical significance vanishing also.

By looking at the corresponding significance we find that $y_C = 0.7$ is a good choice in all cases. Thus, we use this value to find the best cut for the top-antitop quark pair invariant mass. In order to do that, we choose several values of the parameters and we study the trend of the significance as a function of $m_{t\bar{t}}^{\text{min.}}/m_G$. The results are shown in Figs. 6.7 and 6.9. For most values of the parameters, we find two maxima in the statistical significance as a function of $m_{t\bar{t}}^{\text{min.}}/m_G$. Starting from the threshold, where the asymmetry is small because the gluon-gluon fusion process dominates there, the size of the central asymmetry grows by increasing $m_{t\bar{t}}^{\text{min.}}$, as the quark-antiquark annihilation process becomes more and more important. Since the asymmetry induced by the excited gluon vanishes at a certain critical point, its statistical significance does as well, and reaches a maximum at an intermediate value between that critical point and the threshold. Above the critical point, the asymmetry becomes negative and its statistical significance increases again, until the event yield becomes too small. A second maximum in the statistical significance is generated there. For certain values of the vector couplings, however, the critical partonic invariant mass defined in Eq. (5.9) can be located at a rather low scale. In this case, the central asymmetry generated by the exotic resonance will be negative exclusively, and we find only one maximum in the statistical significance.

The optimal cuts depend, of course, on the values of the vector and axial-vector couplings, but either $m_{t\bar{t}}^{\text{min.}}/m_G = 0.5$ or $m_{t\bar{t}}^{\text{min.}}/m_G = 0.8$ provide a reasonable statistical significance for almost all the combinations of the couplings. This is an important result, because it means that a relatively low cut – at about half of the mass of the resonance or even below – is enough to have a good statistical significance, and a clear signal from the measurement of the charge asymmetry. Then, we have calculated the luminosity that would be needed in order to have a statistical significance equal to 5. According to the result on the significance, we expect to find a minimum for relatively low cuts. In Fig. 6.8 we show the results, selecting the part of the phase space where the minimum for the luminosity resides. It can be seen that the luminosity required is around few tens of pb^{-1}, depending on the value of the resonance mass. Again, we should mention that we have not considered experimental efficiencies, therefore this number should be seen only as a lower limit. In a realistic analysis, much higher luminosities will be required to perform that measurement. However, we are interested here in showing the position of the minimum as a function of $m_{t\bar{t}}^{\text{min}}$.

We now fix $m_{t\bar{t}}^{\text{min.}}/m_G = 0.5$ and $m_{t\bar{t}}^{\text{min.}}/m_G = 0.8$, and we study how the central asymmetry and its statistical significance vary as a function of the vector and the axial-vector couplings, for a given value of the resonance mass. These choices, for which we have found the best statistical significances, are of course arbitrary and are not necessarily the best for all the values of the vector and axial-vector couplings. For illustrative purposes are, however, good representatives. We have chosen $m_G = 1.5, 2$ and 3 TeV. The results are presented in Figures 6.10, 6.11, 6.12 and 6.13, 6.14, 6.15 in the (g_V, g_A) plane for $\sqrt{s} = 7$ TeV, and 14 TeV. It is possible to see that the pattern of the size of the asymmetry is quite similar independently of the value of the resonance mass; it depends mostly on the

ratio $m_{t\bar{t}}^{\text{min.}}/m_G$. A sizable asymmetry is found whatever the value of the resonance mass is. The statistical significance, as expected, decreases with the increasing of the resonance mass.

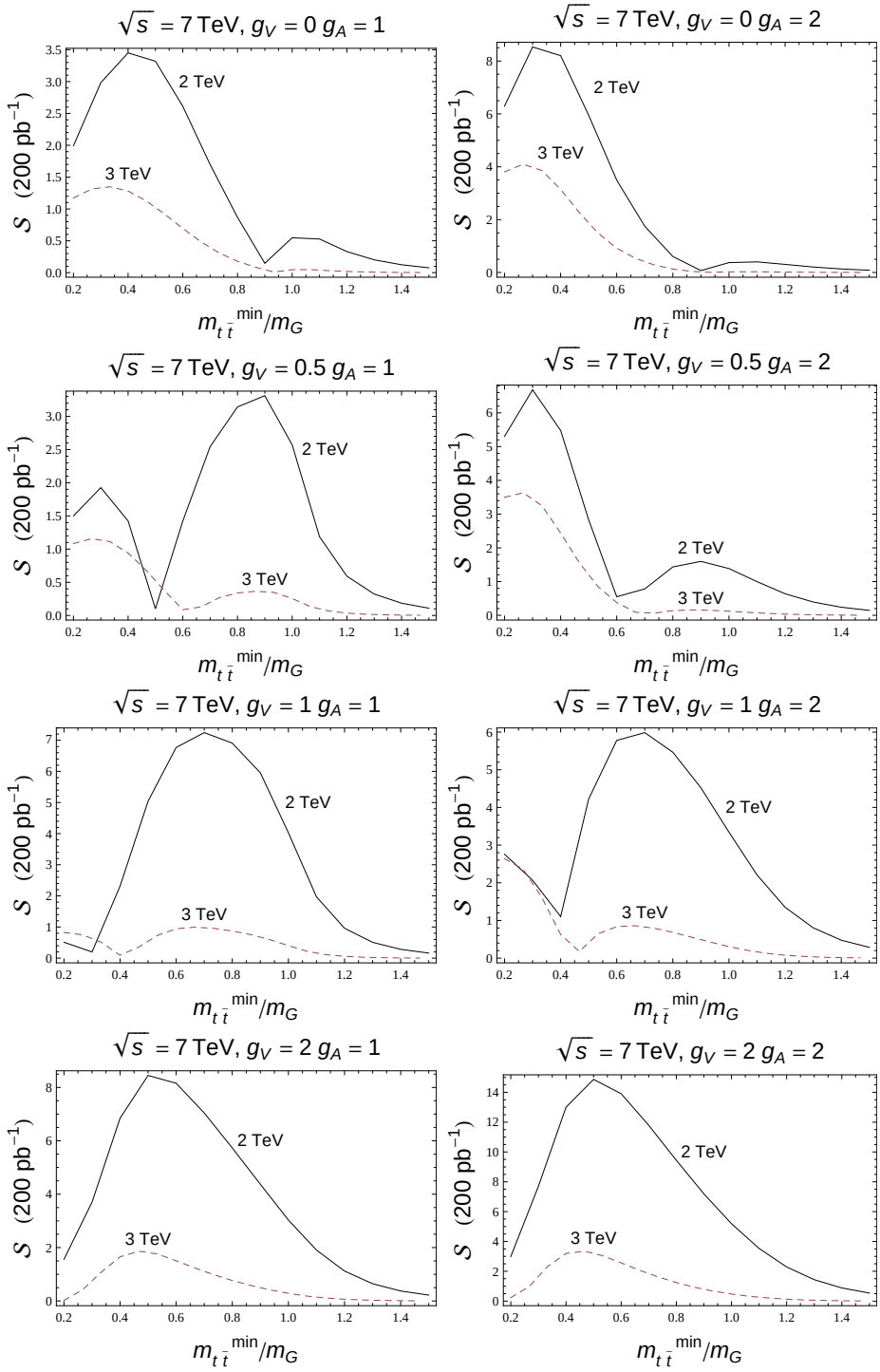

Figure 6.7: Statistical significance at LHC for 7 TeV energy and different sets of g_A, g_V as a function of the cut on the top-antitop quark pair invariant mass for $m_G = 2$ and 3 TeV. The luminosity is $\mathcal{L} = 200$ pb^{-1}

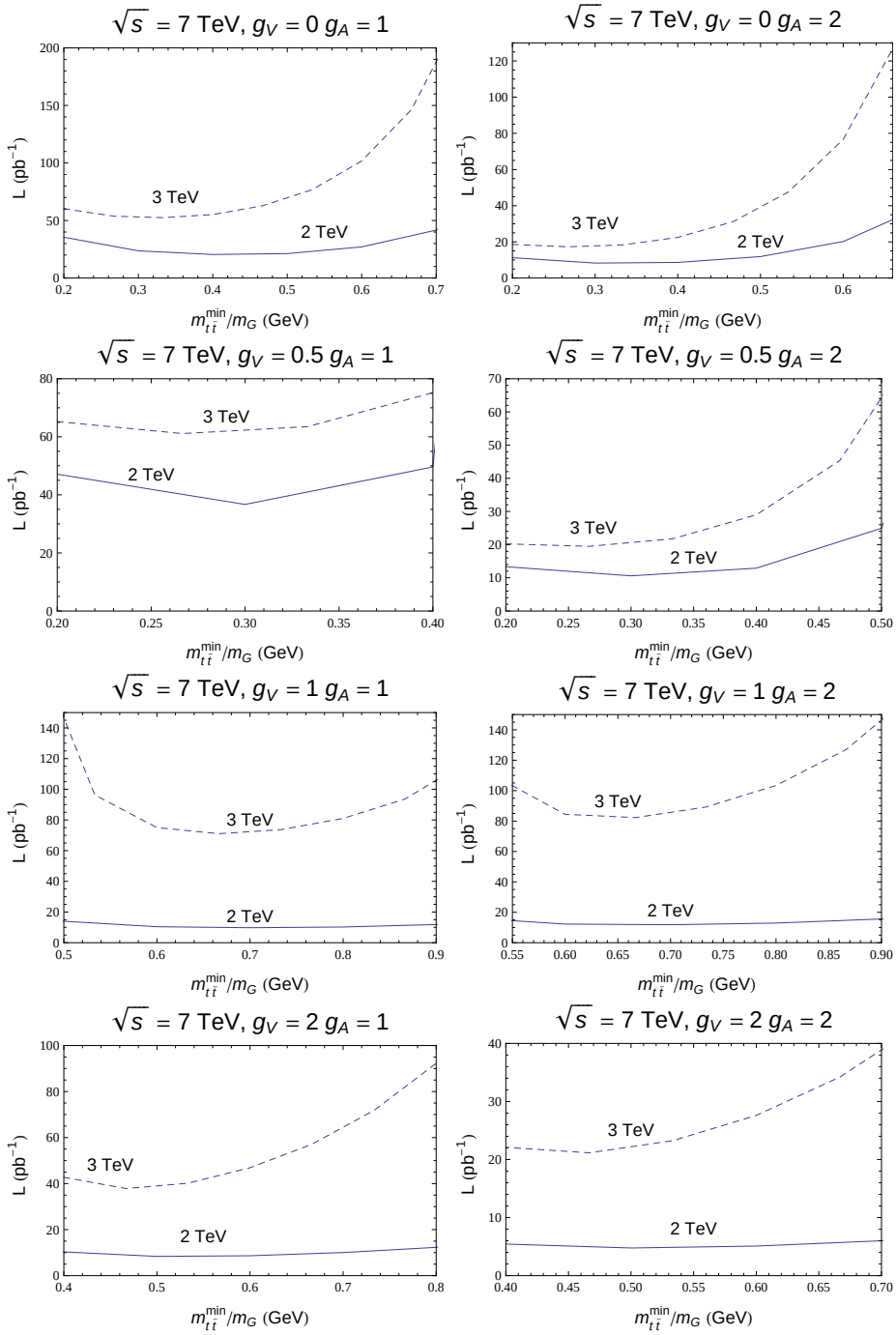

Figure 6.8: Luminosity needed to obtain a statistical significance $\mathcal{S} = 5$ at the LHC for 7 TeV energy and different sets of g_A, g_V as a function of $m_{t\bar{t}}^{\min}$ for $m_G = 2$ and 3 TeV.

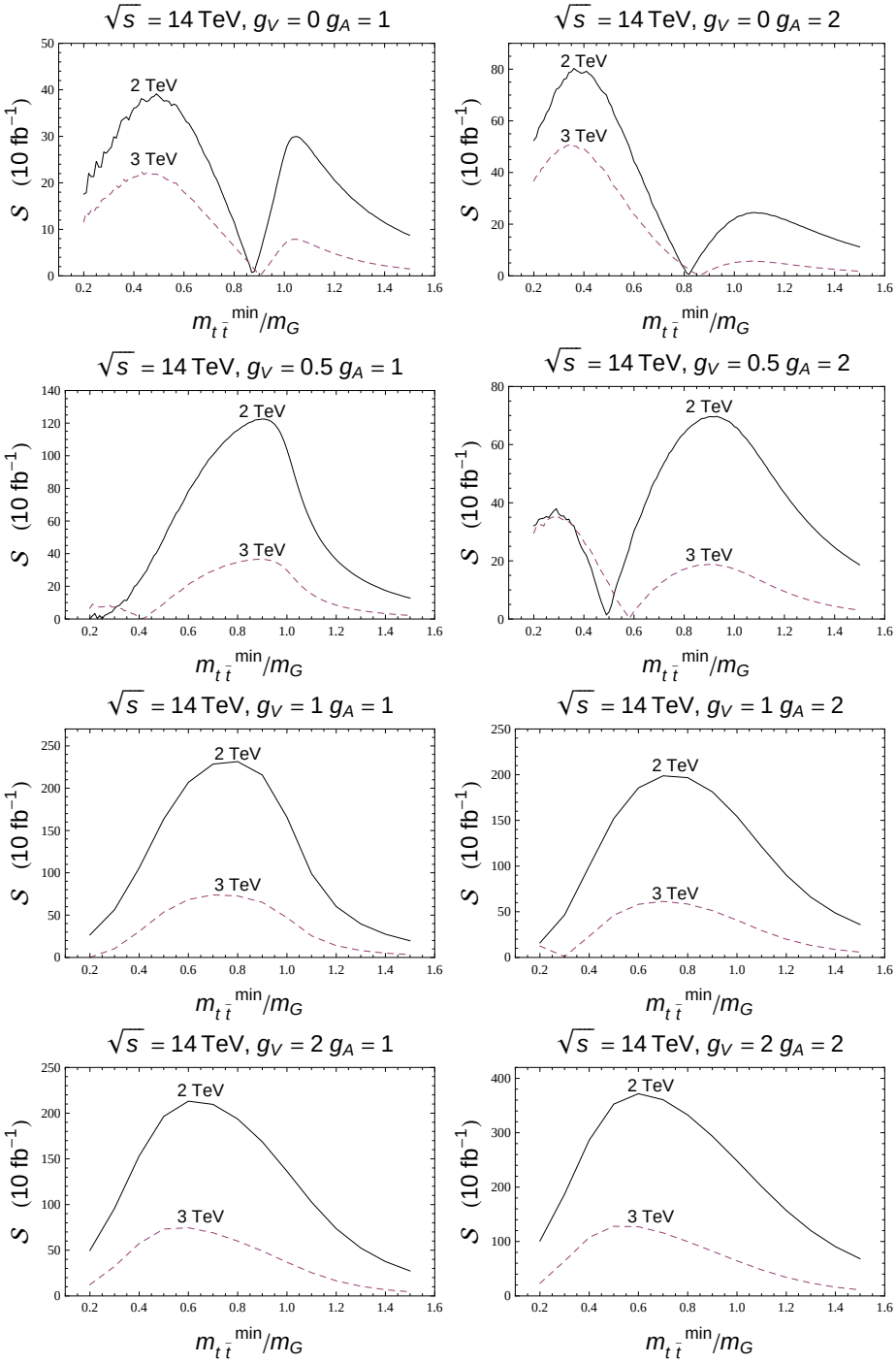

Figure 6.9: Statistical significance at LHC for 14 TeV energy and different sets of g_A, g_V as a function of the cut on the top-antitop quark pair invariant mass for $m_G = 2$ and 3 TeV.

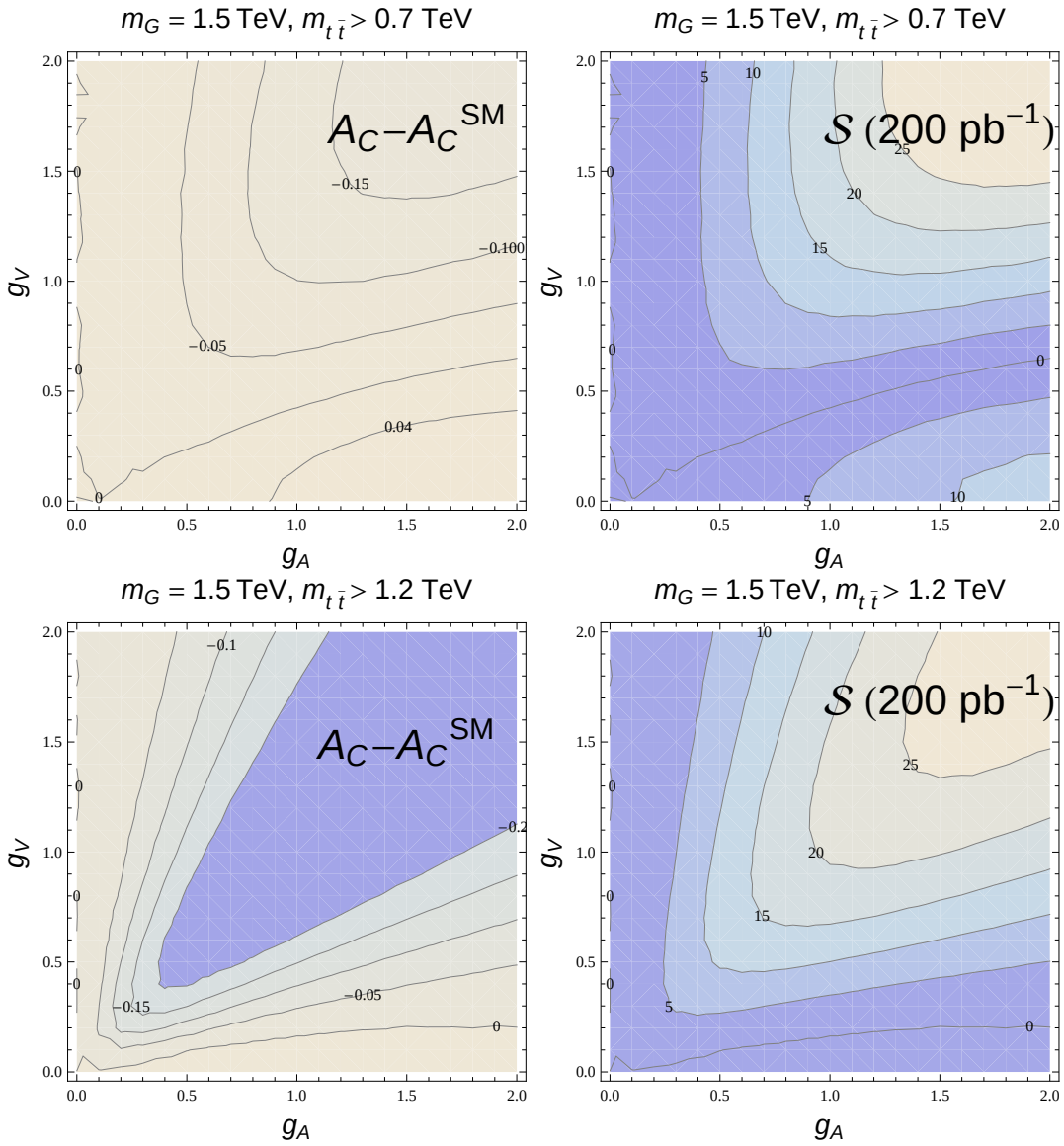

Figure 6.10: Central charge asymmetry and statistical significance at LHC in the g_A-g_V plane for 7 TeV energy, for a resonance mass $m_G = 1.5$ TeV and different values of the cut on the top-antitop quark pair invariant mass.

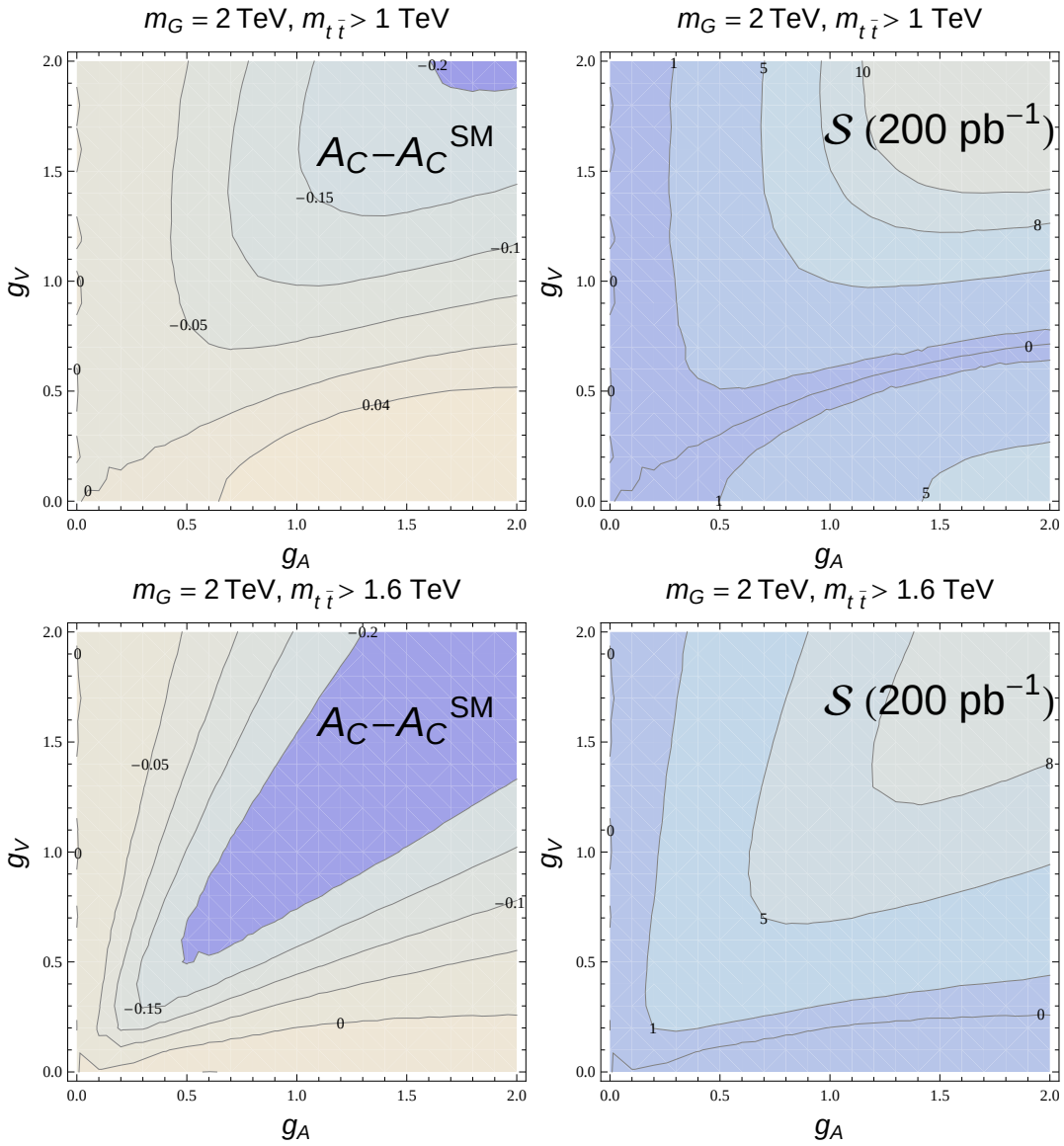

Figure 6.11: Central charge asymmetry and statistical significance at LHC in the g_A-g_V plane for 7 TeV energy, for a resonance mass $m_G = 2$ TeV and different values of the cut on the top-antitop quark pair invariant mass.

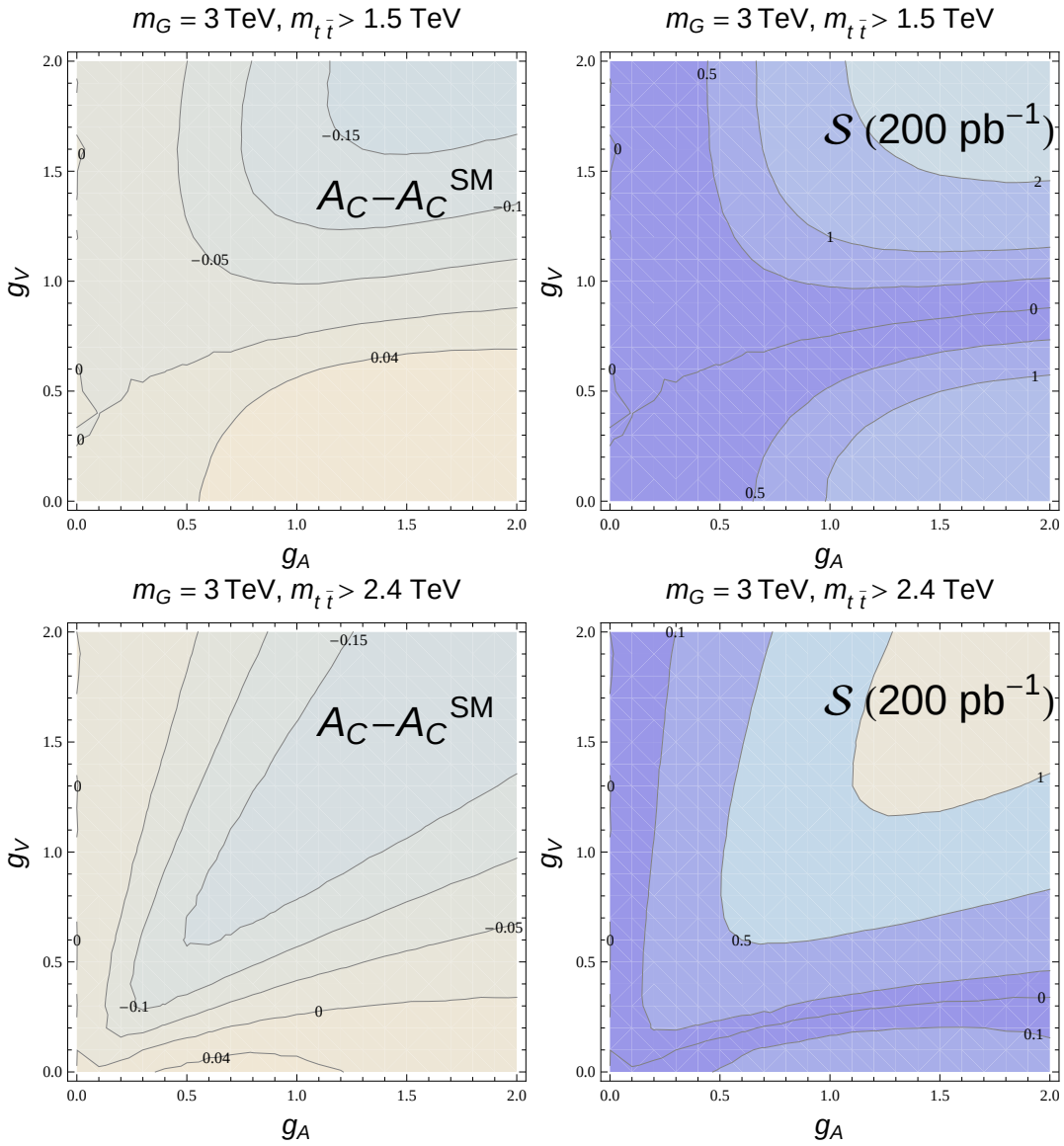

Figure 6.12: Central charge asymmetry and statistical significance at LHC in the g_A-g_V plane for 7 TeV energy, for a resonance mass $m_G = 3$ TeV and different values of the cut on the top-antitop quark pair invariant mass.

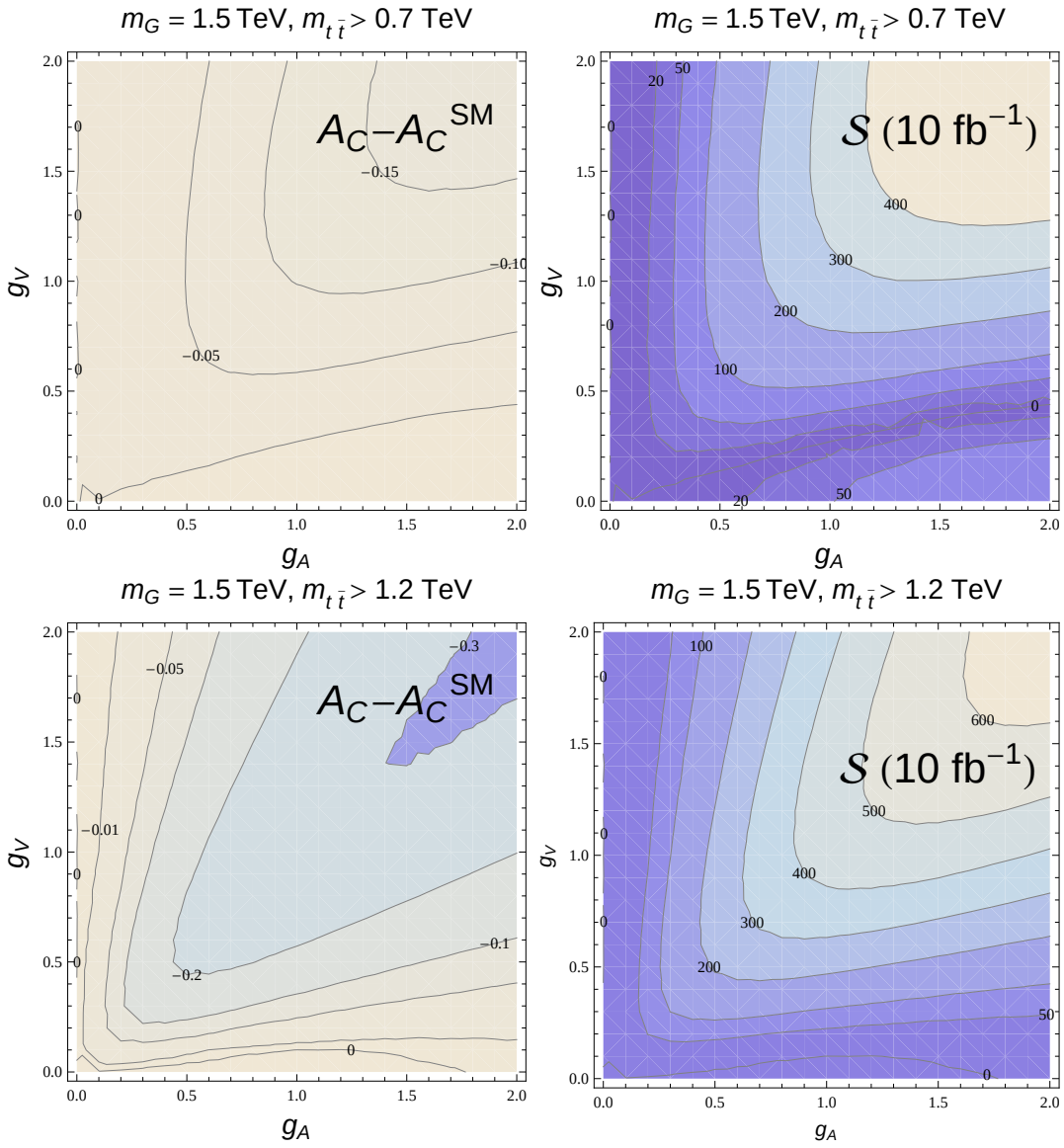

Figure 6.13: Central charge asymmetry and statistical significance at LHC in the g_A-g_V plane for 14 TeV energy, for different values of the resonance mass and the cut on the top-antitop quark pair invariant mass.

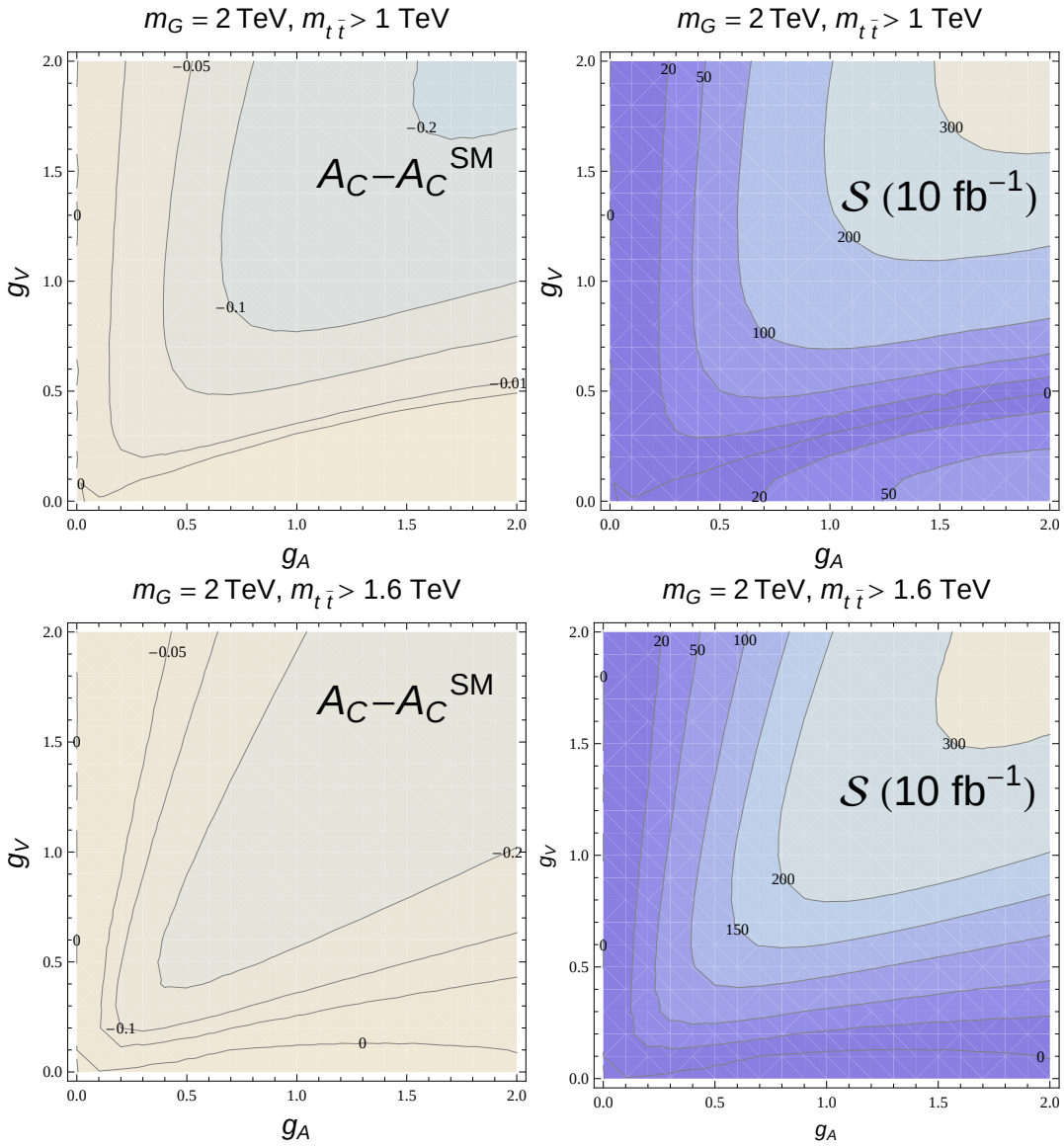

Figure 6.14: Central charge asymmetry and statistical significance at LHC in the g_A-g_V plane for 14 TeV energy, for a resonance mass $m_G = 2$ TeV and different values of the cut on the top-antitop quark pair invariant mass.

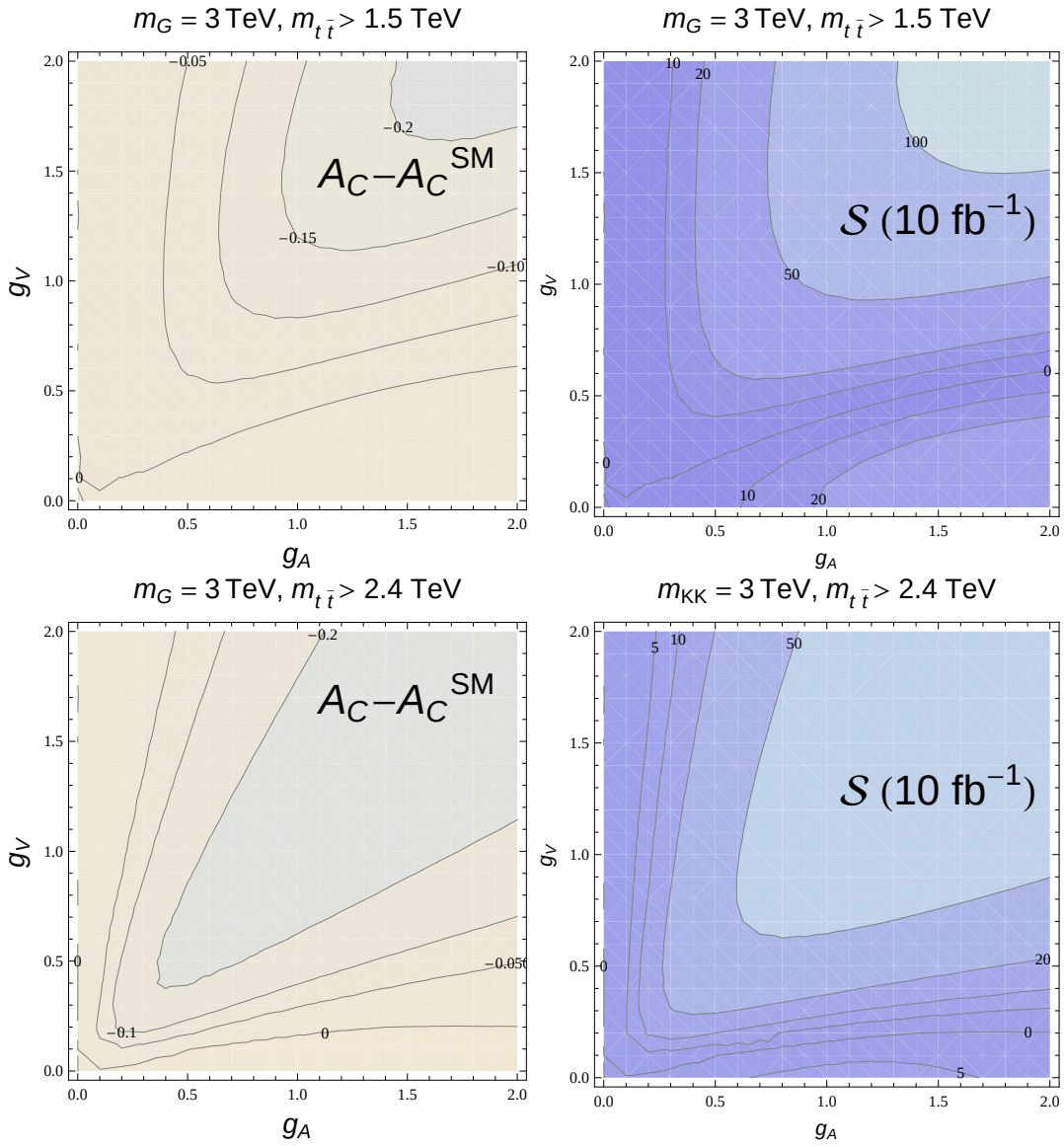

Figure 6.15: Central charge asymmetry and statistical significance at LHC in the g_A-g_V plane for 14 TeV energy, for a resonance mass $m_G = 3$ TeV and different values of the cut on the top-antitop quark pair invariant mass.

6.4 $t\bar{t}$+jet

6.4.1 Introduction

The production of top quark pairs together with one jet is important at the LHC: the exclusive cross-section for this process can reach roughly half of the total inclusive cross-section calculated at next-to-leading order [115]. The asymmetry produced in $t\bar{t}$+jet by the interference of initial- with final-state real gluon emission (Figures 4.4 d, 4.4 e, 4.4 f, 4.4 g) is, obviously, a tree level effect, and, moreover, one of the main contributions to the inclusive asymmetry.

6.4.2 QCD induced charge asymmetry for $t\bar{t}$+jet

The SM predicts a charge asymmetry in $t\bar{t}$+jet already at tree level from $q\bar{q}$ events. This asymmetry is of similar size, but of opposite sign to the total $t\bar{t}$ inclusive asymmetry [86]. The differential asymmetric cross section for $t\bar{t}$+jet is given in Appendix B.1.

In the previous section we have found that for the central asymmetry in Eq. (6.1) values of the maximum rapidity around $y_C = 0.7$ maximize the statistical significance. Thus, in the following, we fix $y_C = 0.7$, and analyze the central asymmetry in the SM as a function of the cut on $m_{t\bar{t}}$. The additional jet is defined by using the k_T algorithm described in Section 1.2, with minimum transverse momentum $p_T = 20$ GeV and the jet parameter $R = 0.5$. In Fig. 6.16 we show the results for center-of-mass energies of 7 and 10 TeV. We find that the asymmetry is positive and of the order of few percents (Fig. 6.16, left plots). As expected, at 7 TeV the asymmetry is higher than at 10 TeV, for the same value of $m_{t\bar{t}}^{\rm min}$, because the $q\bar{q}$ component is larger. The right plots in Fig. 6.16 show the luminosity that would be needed in order to have a statistical significance equal to 5. The statistical significance $\mathcal{S}^{\rm SM}$ of the measurement is defined as in (6.4). From Fig. 6.16 we see that there is a minimum in the required luminosity for low values of $m_{t\bar{t}}^{\rm min}$. Before that minimum, the luminosity increases since the corresponding asymmetry approaches zero, while after the minimum, it increases because the number of events decreases.

6.4.3 Charge asymmetry of color-octet resonances

As in the inclusive process, we consider now a toy model where a color-octet vector resonance can couple differently to light and top quarks. In this case, a new diagram appear that contribute to the asymmetry, namely the gluon emission from the exchanged particle. In Fig. 6.17 we show the complete set of diagrams that take part in the asymmetry. Compared to QCD, now asymmetric contributions are generated also by products of final-state with final-state and initial-states with initial-state bremsstrahlung ($(b+d)\otimes(b+d)$ and $(c+e)\otimes(c+e)$), besides the interferences with the new graphic $(a\otimes(a+b+c+d+e))$.

In Appendix B.2 we list the expression for the asymmetric contribution to the $t\bar{t}$+jet differential cross section. It is interesting to stress that, contrary to the SM, where top quarks contribute to the asymmetry only when they are in a color-singlet state (color factor

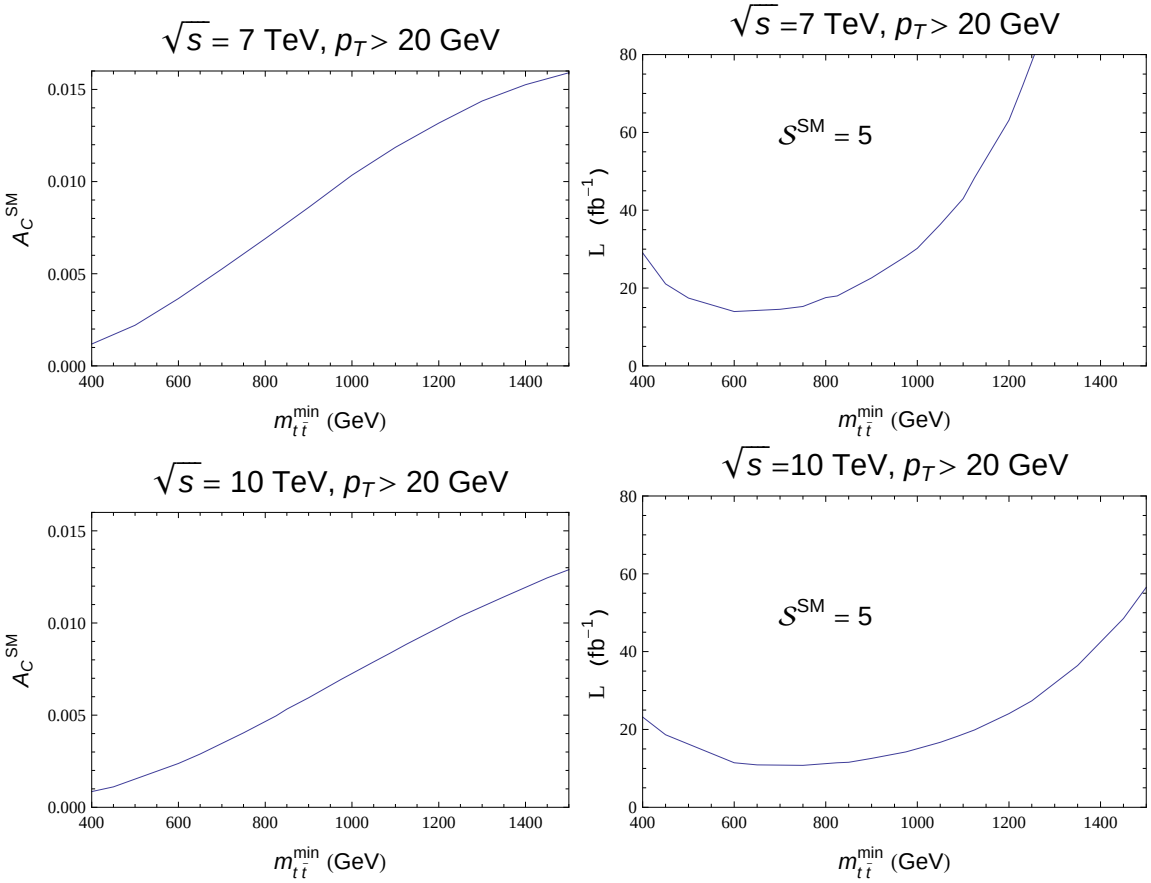

Figure 6.16: Central charge asymmetry and luminosity at the LHC from QCD, as a function of the cut $m_{t\bar{t}}^{\min}$ for $\sqrt{s} = 7$ TeV and 10 TeV.

equal to d_{abc}^2), we find also color-octet contributions proportional to the color factor f_{abc}^2. We consider now three different scenarios. A large part of the parameter space for flavor-universal couplings is disfavored because the inclusive asymmetry in that case is negative, as seen in Section 5.3. In particular, axigluons such as originally introduced [65], i. e. with $g_V^{q(t)} = 0$, $g_A^{q(t)} = 1$, would be forbidden. Yet, it is possible to generate a positive inclusive asymmetry if the lighter quarks and the top quarks couple with different sign. Thus, as a first case, we examine a "modified axigluon", with $g_V^{q(t)} = 0$ and $g_A^t = -g_A^q = 1$. In the flavor-universal scenario, the only possibility that is still allowed at the 95% C.L. is the one where g_V takes high values and g_A is constrained accordingly as a function of the resonance mass. So we choose as a second scenario $g_V^{q(t)} = 1.8$ and $g_A^{q(t)} = 0.7$. In the third scenario we focus on a Kaluza–Klein gluon excitation in a basic Randall–Sundrum model: $g_V^q = -0.2$, $g_V^t = 2.5$, $g_A^q = 0$, $g_A^t = 1.5$, as presented, for instance, in [116]. Since the axial coupling for the light quarks is zero, the inclusive central charge asymmetry vanishes at tree level. Thus, it is necessary to look at the hard emission process, where it becomes different from zero. Accordingly, the inclusive charge asymmetry will get also

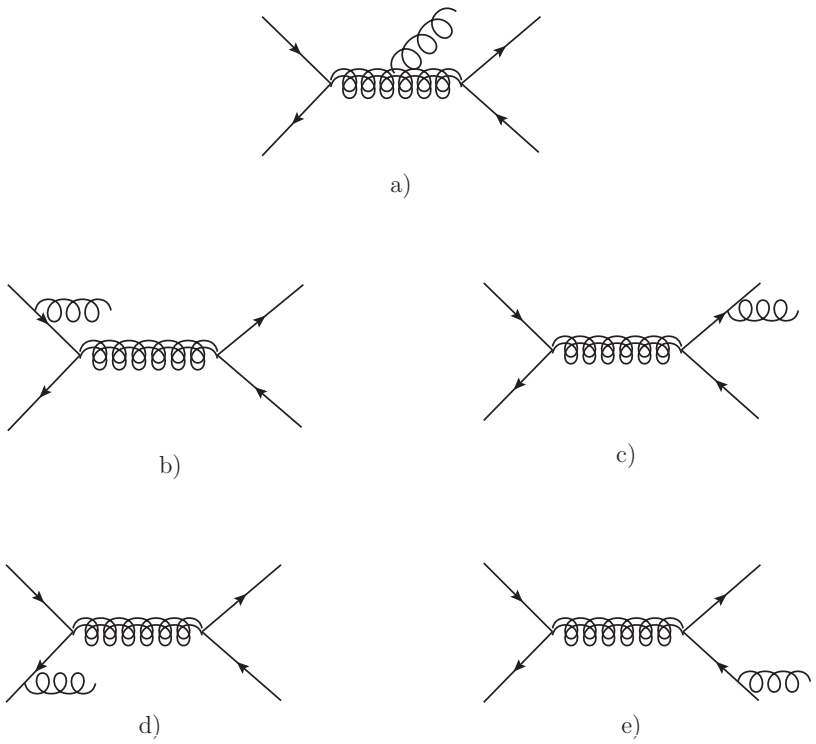

Figure 6.17: Graphs originated by $q\bar{q}$ that contribute to the charge asymmetry in quark-antiquark + jet production. The exchanged particle can be both the gluon and the massive resonance.

non-vanishing loop contributions.

The results for the asymmetry and the minimal luminosity to achieve a statistical significance of 5 are shown in Fig. 6.18. We have chosen $m_G = 1.5$ TeV as a reference mass for the resonance. As in the pure QCD case, the maximal rapidity of $y_C = 0.7$ is optimal to enhance the statistical significance, which is defined, like in (6.5) as:

$$\mathcal{S} = \frac{A_C - A_C^{\rm SM}}{\sqrt{1-(A_C^{\rm SM})^2}} \sqrt{(\sigma_t + \sigma_{\bar{t}})^{\rm SM}\, \mathcal{L}}\ . \tag{6.6}$$

The luminosity required to have a fixed significance has a minimum for low values of $m_{t\bar{t}}^{\rm min}$, at around one half the mass of the resonance, for all the scenarios. In the flavor-universal case, we found that this minimum value is reached with even softer cuts. We find also that in this scenario the needed luminosity is lower than in the other two cases, and almost of about one order of magnitude less. A few hundreds of pb^{-1} at relatively low values of $m_{t\bar{t}}^{\rm min}$ would allow a measurement in the first times of the LHC running. The Kaluza-Klein model shows an asymmetry of opposite sign compared to the other two cases. This can be an interesting way for distinguishing it from the other models. In Fig. 6.18 we also show the color-singlet contribution to the asymmetry. In the modified axigluon scenario, it has

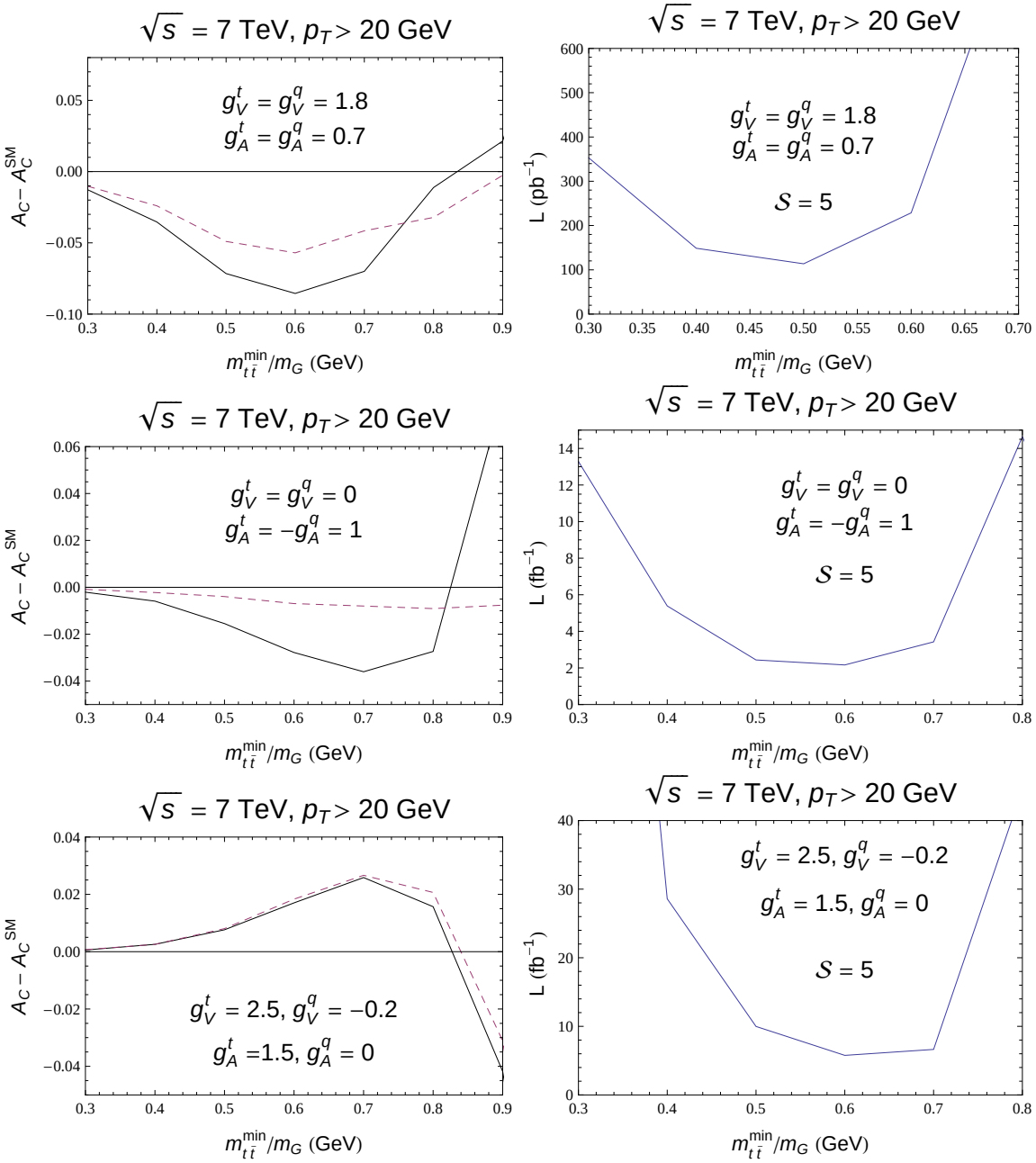

Figure 6.18: Central charge asymmetry and luminosity to obtain a statistical significance $\mathcal{S} = 5$ at the LHC, as a function of $m_{t\bar{t}}^{\min}$ for $\sqrt{s} = 7$ TeV. The dashed line represent the contribution of the d_{abc}^2 terms. $m_G = 1.5$ TeV.

opposite sign compared with the total asymmetry. In the flavor-universal scenario it is about one half of the asymmetry. In the Kaluza-Klein model, the color-octet contribution is almost zero.

6.4.4 Conclusions

In this analysis, we have explored the central charge asymmetry in $t\bar{t}$ + jet at the LHC. We have found that it receives contributions from top quark pairs both in a color-octet and in a color-singlet state. We have set a lower limit on the luminosity needed in order to have a statistical significance equal to 5 for three different scenarios at $\sqrt{s} = 7$ TeV. We have found that, in the flavor-universal case, this lower bound is around a few hundreds of pb^{-1}, while for the other scenarios few fb^{-1} are required. These values depend, of course, on the resonance mass. We have not considered the detector efficiency, so these numbers should be taken as a lower limit. For the three choices of the parameters that we have considered, the minimum of the required luminosity is reached for relatively low values of $m_{t\bar{t}}^{\text{min}}$. This is a non-trivial result as it means that relatively low energetic top quarks can already generate an asymmetry. This is an advantage, because very boosted top quarks are difficult to distinguish from jets initiated by light quarks.

NLO calculations of $t\bar{t}$+jet [93] in the SM show that the exclusive asymmetry is almost completely washed out at the Tevatron. Although there is no reason why we should find the same behavior if a heavy resonance exists, it would be interesting to extend this analysis at NLO, and to combine it with a realistic estimation of experimental efficiencies. From our analysis, the measurement of the charge asymmetry from $t\bar{t}$+jet events at the LHC seems promising, although challenging. Experimental analysis from the Tevatron with more statistics will also constrain further those resonances in the near future.

Conclusions

The next years promise to be very exciting for particle physics, due to the incoming LHC data. The insight into the TeV scale will shed light on both conceptual problems and phenomenological issues, such as the origin of mass, the dark matter constituents, the unification of gravity inside the SM or the hierarchy problem [13]. Several models have been proposed in the last decades that would account for these fundamental questions, some of which introduce new particles and interactions. Due to its high energy in the centre-of-mass, the LHC is the most suitable environment to test them.

In order to be prepared for understanding the huge amount of data that the LHC will collect, an optimal knowledge of QCD is mandatory. The ATLAS and CMS experiments will measure the final states with negligible statistical error, even in the early running, and in many cases with systematic errors smaller than those achieved by the experiments at the Tevatron. In many cases, SM backgrounds to non-SM physics can be extrapolated from background-rich to signal-rich regions, but a definite determination of the background often requires an accurate knowledge of the background cross sections [5]. This requires calculations of many QCD processes to at least NLO in perturbation theory.

In this thesis, we have addressed the challenges that the start up of the LHC presents us, from a double point of view. On one hand, we have faced the issue of improving the efficiency of scattering amplitudes calculations, looking for compact results (Chapters 2 and 3). This is necessary when the number of external legs increases, since the number of Feynman diagrams that one needs to calculate becomes huge. Moreover, such calculations can be more easily extended to higher orders. On the other hand, we have analysed the possibility of accounting for the discrepancy in the charge asymmetry that arises at 2σ at the Tevatron in top quark pair production. Considering a toy model with a heavy colored resonance, we have set constraints on the couplings and have estimated the necessary luminosity in order to achieve a good significance at the LHC (Chapters 4, 5 and 6).

As for the first part of our work, we have used techniques alternative to the usual Feynman diagram calculation. They consist of color ordering and spinor helicity formalism, combined with recursion relations. They have been used in the past thirty years to calculate n-parton amplitudes efficiently both at tree level and one or more loops. In Chapter 3 we have shown the results obtained. At the LHC the energy reached will be enough to produce a large amount of heavy particles. Thus, we have analysed massive tree level processes involving a colored scalar-antiscalar pair together with an arbitrary number of gluons, with or without a complex colorless scalar ϕ. The reason for choosing colored

scalars instead of quarks is double: on one side, they are simpler, since they do not carry helicity, and at tree level the amplitudes are related with the amplitudes of the quarks through supersymmetric Ward identities. On the other side, string theory tells us that one-loop gluon and fermion amplitudes can be decomposed in terms of supersymmetric and non-supersymmetric parts. The non-supersymmetric part is a one-loop amplitude involving scalars, which can be written from the tree level amplitude by means of the Cutkosky rules.

At first, we have calculated the amplitude $A_n(1_s; 2^+, \ldots, n-1^+; n_{\bar{s}})$ with all-positive helicity gluons and have managed to get to a result much simpler and compact than the one available in literature. Starting from the scalar QCD Lagrangian, we have derived the couplings among gluons and scalars and developed the construction of the amplitudes from off-shell recursion relations, starting with low n. We have identified the useful kinds of relationships and have applied them to the amplitude for a generic n. Then, we have validated the result obtained through the on-shell BCFW recursion relations, finding the final result:

$$A_n(1_s; 2^+, \ldots, n-1^+; n_{\bar{s}}) = i\, m^2\, \frac{[2|\Phi_{3,j}|n-1]}{y_{12}\langle\langle 2, n-1\rangle\rangle} \ . \tag{6.7}$$

The compactness of this result makes it very useful in successive calculations and as a tool to verify other results.

The next step has been to add a colorless scalar ϕ to the amplitude. Since the all-positive helicity amplitude vanishes, we have analysed the one with one–negative helicity gluon in the last position. We have used on–shell recursion relations to simplify the calculations. The starting point has been the expression found by [52]. We have used the same shift and we have applied it to our case, with the addition of ϕ. The amplitude thus obtained presented some spurious, unphysical denominators, and our aim has been to cancel them. The kernel of the procedure has been to reorganize the terms of the sum in a different way, grouping parts with the same denominators to obtain quantities in the numerator exactly equal to the spurious terms. The result is:

$$\begin{aligned} A_n(\phi; 1_s, 2^+, \ldots, n-2^+, n-1^-, n_{\bar{s}}) = \frac{-i}{y_{12}\,\langle\langle 2, n-1\rangle\rangle} \Bigg\{ & \frac{[2|\not{p}_1|n-1\rangle\langle n-1|\not{p}_1\not{p}_n|n-1\rangle}{s_{n1}} \\ + \sum_{j=2}^{n-2} \frac{m^2}{s_{n,j}} [2|\Phi_{3,j-1} & \left(\frac{\not{p}_j|n-1\rangle\langle n-1|\not{p}_n}{y_{1,j}} + \frac{\not{p}_{n,j-1}|n-1\rangle\langle n-1|\not{p}_j}{s_{n,j-1}} \right) \not{p}_{n,j}|n-1\rangle \Bigg\} \ . \end{aligned} \tag{6.8}$$

This is a very compact result and the absence of denominators makes it suitable for numerical calculations, because it does not produce any fake instability due to the vanishing of spurious denominators. The compact form of (6.8) suggests also the possibility of extending it to an arbitrary position of the negative helicity gluon.

In the second part of our work, we have focused our attention on top quark pair production at hadron colliders. The LHC will produce a huge amount of top quarks, so it

will be the perfect environment to study top quark physics. A charge asymmetry in top quark pair production is predicted in QCD at $\mathcal{O}(\alpha_s^3)$. However, a discrepancy of 2σ with the theoretical value has been found recently in the forward-backward asymmetry measurements at the Tevatron. This has aroused a considerable interest in the study of new physics models where resonances decaying to a top-antitop quark pair are produced, which also generate a charge asymmetry.

In our work, we have analyzed the charge asymmetry in top-antitop quark pair production through the exchange of a color-octet heavy boson with arbitrary vector and axial-vector couplings to quarks. We have considered the experimental setups of the Tevatron and the LHC, studying different observables and scenarios.

At the Tevatron, we have examined, at first, the scenario of flavour independent couplings. The forward-backward asymmetry and the pair asymmetry, together with the total cross section, exclude complementary corners of the parameter space. The exclusion regions are smaller for higher values of the resonance mass, since a high mass suppresses all the contributions beyond the SM. The most recent measurement excludes a negative charge asymmetry within 2σ. Moreover, although the total cross section remains unchanged in the presence of a heavy resonance, the differential distribution in the top-antitop quark invariant mass can be affected significantly, particularly for high values of the top-antitop quark pair invariant mass. For this reason, we have combined the measurement of the asymmetry and the last bin of the differential distribution of the top quark pair invariant mass to constrain the parameter space. We have found that in the flavor universal scenario the constraint is large. However, in flavor nonuniversal cases, it is still possible to reconcile the experimental data with the existence of such resonances, and already a significant region of the parameter space can be excluded. Considering that the Tevatron is still running, we expect that the next measurements will set further constraints on the charge asymmetry, since the statistical error will keep on decreasing.

At the LHC the forward-backward asymmetry vanishes, because the initial state is symmetric. However, a charge asymmetry is still observable by selecting appropriate kinematic regions. First, we have studied the statistical significance of the measurement of the central asymmetry in top quark pair inclusive production, and we have found that it is possible to tune the selection cuts in order to find a sensitive significance. The maximum of the statistical significance for the measurement of the asymmetry as predicted by QCD is obtained without introducing any cut in the invariant mass of the top-antitop quark pair, although the asymmetry is smaller in this case.

When a heavy resonance is considered, one or two maxima in the significance spectrum are found, depending on the size of the couplings. The position of the peaks depends on the ratio $m_{t\bar{t}}^{\min}/m_G$ and not on the resonance mass. One of the peaks can be located at an energy scale as low as one half of the resonance mass, or even below. Thus, data samples of top and antitop quarks that are not too energetic can be used to detect or exclude the existence of this kind of resonances. We have plotted the integrated luminosity needed in order to have a statistical significance of 5. Consistently with the significance analysis, we have found that a minimum in the luminosity appears for low values of the cut on $m_{t\bar{t}}^{\min}/m_G$. Fixing the cut to the values that maximize the statistical significance, we have

scanned the space of the couplings (g_A, g_V), finding that the pattern for the asymmetry and the significance does not depend on the mass of the resonance, but only on $m_{t\bar{t}}^{\min}/m_G$.

Successively, we have analyzed the production of top quark pairs together with one jet. In this case, the asymmetry is a tree level effect and receives contributions both from color-singlet and color-octet quark final states. This process is important at the LHC and is especially significant to test those models of resonances whose inclusive pair production does not generate a charge asymmetry at tree level. This is the case, for instance, of most of the Kaluza-Klein excitations in extra-dimensional models. After calculating the differential cross section for $t\bar{t}+$ jet, we performed the same analysis as in the inclusive case. We have found that a minimum in the luminosity needed to have a statistical significance equal to 5 is reached for pretty low values of the cut on the top-antitop quark invariant mass distribution. Again, this result opens the possibility of using low energy top quark samples to identify resonances also in exclusive production.

The calculations with the presence of resonances that we have performed in our work have been carried out at tree level. Although a more accurate analysis would require one loop calculations to ascertain the contribution of higher orders to the asymmetry, our result is important, because opens the promising possibility of measuring the charge asymmetry in top-antitop quark production already in the first period of running of the LHC.

Conclusiones

Los próximos años prometen ser muy interesantes para la física de partículas gracias a los datos del LHC. La investigación de la escala de energía del TeV arrojará luz sobre problemas conceptuales así como sobre cuestiones fenomenológicas, como, por ejemplo, el origen de las masas, los constituyentes de la materia oscura, la unificación de la gravedad dentro del SM o el problema de la jerarquía. En las últimas decadas se han propuesto distintos modelos para responder a estas preguntas fundamentales, algunos de los cuales introducen nuevas partículas e interacciones. Gracias a su alta energía en el centro de masa, el LHC es el entorno más adecuado para probarlos.

Es necesario un excelente conocimiento de QCD para comprender la gran cantidad de datos que el LHC va a acumular. Los experimentos ATLAS y CMS van a medir los estados finales con error estadístico despreciable, incluso en el primer periodo de funcionamiento, y en muchos casos con errores sistemáticos menores que los alcanzados en los experimentos de Tevatron. Esto requiere el cálculo de muchos procesos de QCD por lo menos a NLO en teoría de las perturbaciones.

En esta tesis, hemos tratado de responder a los desafíos que la puesta en marcha del LHC nos propone, desde un doble punto de vista. Por un lado, nos hemos enfrentado a la cuestión de mejorar la eficiencia del cálculo de las amplitudes de dispersión, buscando resultados compactos (capítulos 2 y 3). Esto es necesario cuando el número de patas externas aumenta, debido a que el número de diagramas de Feynman que uno necesita calcular se hace enorme. Además, estos cálculos se pueden extender más fácilmente a ordenes más altos. Por otro lado, hemos analizado la posibilidad de explicar la discrepancia en la asimetría de carga que es generada en Tevatron a dos sigmas en la producción de pares de quark top. Considerando un modelo que incluye una resonancia masiva que lleva carga de color, hemos impuesto limitaciones a las constantes de acoplo y hemos dado una estimación de la luminosidad necesaria para alcanzar una buena significancia estadística en la medida de la asimetría en el LHC (capítulos 4, 5 y 6).

En la primera parte de nuestro trabajo, hemos usado como técnicas alternativas al cálculo usual con diagramas de Feynman la descomposición de color y el formalismo de helicidad, junto con relaciones de recursión. Estas técnicas se han estado usando en los últimos treinta años para calcular amplitudes de dispersión con n partículas de forma eficiente, tanto a nivel árbol como a uno o más *loops*. En el capítulo 3 hemos mostrado los resultados obtenidos. En el LHC la energía alcanzada será suficientemente alta como para producir una gran cantidad de partículas pesadas. Por eso, hemos analizado procesos

masivos, a nivel árbol, que involucran un par de escalar-antiescalar con color, junto a un número arbitrario de gluones, en presencia o en ausencia de un escalar sin color complejo ϕ. La razón de haber escogido escalares con color en lugar de quarks es dúplice: por un lado, los escalares son más simples, debido a que no llevan helicidad y a nivel árbol sus amplitudes de dispersión están relacionadas con las amplitudes de los quarks a través de las identidades de Ward supersimétricas. Por otro lado, la teoría de cuerdas afirma que las amplitudes a un *loop* de gluones y fermiones se pueden descomponer en términos de una parte supersimétrica y otra no supersimétrica. Esta última es una amplitud a un *loop* que contiene escalares, que puede escribirse a su vez en función de amplitudes a nivel árbol, a través de las reglas de Cutkosky.

En un primer momento, hemos calculado la amplitud de dispersión $A_n(1_s; 2^+, \ldots, n-1^+; n_{\bar{s}})$, con todos los gluones de helicidad positiva y hemos conseguido obtener un resultado mucho más sencillo y compacto que la expresión ya disponible en literatura. Empezando por el Lagrangiano de la QCD escalar, hemos derivado los acoplamientos entre gluones y escalares y hemos desarrollado la construcción de las amplitudes a través de relaciones de recursión *off–shell*, partiendo de n bajos. Hemos identificado las relaciones útiles para simplificar la expresión y las hemos aplicado a la amplitud para un n genérico. Finalmente, hemos confirmado el resultado obtenido a través de las relaciones de recursión *on–shell* BCFW, llegando al resultado final:

$$A_n(1_s; 2^+, \ldots, n-1^+; n_{\bar{s}}) = i\, m^2\, \frac{[2|\Phi_{3,j}|n-1]}{y_{12}\langle\langle 2, n-1\rangle\rangle} \ . \tag{6.9}$$

La compacidad de este resultado lo convierte en un instrumento muy útil para cálculos sucesivos y para validar otros resultados.

El paso sucesivo ha sido añadir un escalar ϕ sin color a la amplitud. Debido a que la amplitud con todos los gluones de helicidad positiva es cero, hemos analizado la amplitud con un gluón de helicidad negativa en la última posición. Hemos usado relaciones de recursión *on–shell* para simplificar los cálculos. El punto de partida ha sido la expresión encontrada en [52]. Nosotros hemos usado el mismo desplazamiento de momentos y lo hemos aplicado a nuestro caso añadiendo ϕ. La amplitud obtenida de esta forma presentaba unos denominadores espurios y no físicos y nuestro objetivo ha sido cancelarlos. El principio fundamental de este procedimiento ha sido reorganizar los términos de la suma en una forma diferente, reagrupando partes con el mismo denominador para obtener cantidades que cancelaran los términos espurios. El resultado es:

$$\begin{aligned} A_n(\phi; 1_s, 2^+, \ldots, n-2^+, n-1^-, n_{\bar{s}}) = \frac{-i}{y_{12}\,\langle\langle 2, n-1\rangle\rangle} \Bigg\{ & \frac{[2|\not{p}_1|n-1\rangle\langle n-1|\not{p}_1\not{p}_n|n-1\rangle}{s_{n1}} \\ + \ \sum_{j=2}^{n-2} \frac{m^2}{s_{n,j}} [2|\Phi_{3,j-1} & \left(\frac{\not{p}_j|n-1\rangle\langle n-1|\not{p}_n}{y_{1,j}} + \frac{\not{p}_{n,j-1}|n-1\rangle\langle n-1|\not{p}_j}{s_{n,j-1}} \right) \not{p}_{n,j}|n-1\rangle \Bigg\} \ . \end{aligned} \tag{6.10}$$

Ésta es una expresión muy compacta y la ausencia de denominadores hace que sea idónea para cálculos numéricos, pues evita inestabilidades falsas asociadas con denominadores nulos. Asimismo, la forma compacta de (6.10) sugiere la posibilidad de extender el cálculo a una posición arbitraria del gluón de helicidad negativa.

En la segunda parte de nuestro trabajo, nos hemos centrado en la producción de pares de quarks top en colisionadores hadrónicos. El LHC producirá una gran cantidad de quarks top, por lo tanto va a ser el entorno perfecto para estudiar la física del top. A $\mathcal{O}(\alpha_s^3)$, QCD predice una asimetría de carga en la producción de pares de quarks top. No obstante, en Tevatron recientemente se ha encontrado una discrepancia de alrededor de 2σ entre las medidas de la asimetría *forward-backward* y la predicción de su valor teórico. Esto ha despertado un considerable interés para el estudio de modelos de nueva física donde se producen resonancias que se desintegran a un par de quarks top-antitop y que generan también una asimetría de carga.

En nuestro trabajo, hemos analizado la asimetría de carga en la producción de pares de top-antitop a través del intercambio de un bosón masivo octeto de color con acoplamiento arbitrario tanto vectorial como axial a los quarks. Hemos considerado la situación experimental de Tevatron y de LHC, estudiando distintos observables y escenarios.

En Tevatron, hemos examinado en primer lugar el escenario de acoplamientos independientes del sabor. La asimetría *forward-backward* y la asimetría *pair*, junto con la sección eficaz total, excluyen partes complementarias del espacio de los parámetros. Las regiones de exclusión son más pequeñas cuanto más alta es la masa de la resonancia, debido a que una masa grande suprime todas las contribuciones más allá del SM. Las medidas más recientes excluyen una asimetría negativa dentro de 2σ. Además, aunque la sección eficaz total permanece invariada en presencia de una resonancia masiva, la distribución diferencial de la masa invariante del par top-antitop puede resultar afectada significativamente, en particular para altos valores de la masa invariante. Por esta razón, hemos combinado la medida de la asimetría y el último intervalo de la distribución diferencial de la masa invariante para poner limitaciones sobre el espacio de los parámetros. Hemos encontrado que en el escenario de acoplamientos independientes del sabor dichas limitaciones son grandes. No obstante, en los casos de acoplamientos distintos según el sabor de los quarks es posible todavía conciliar los datos experimentales con la existencia de dichas resonancias y excluir una región significativa del espacio de los parámetros. En vista de que Tevatron sigue funcionando, esperamos que futuras medidas establezcan ulteriores limitaciones sobre la asimetría de carga, porque el error estadístico seguirá disminuyendo.

En el LHC la asimetría *forward-backward* es nula, debido a que el estado inicial es simétrico. No obstante, se puede todavía observar una asimetría de carga seleccionando regiones cinemáticas apropiadas. En primer lugar, hemos estudiado la significancia estadística de la medida de la asimetría central en la producción inclusiva de pares de quarks top-antitop y hemos establecido que es posible afinar los cortes con el fin de encontrar una significancia sensible. El máximo de la significancia estadística para la medida de la asimetría tal y como predice QCD se obtiene sin introducir ningún corte en la masa invariante del par de tops, aunque la asimetría es menor en este caso.

Cuando se toma en consideración una resonancia pesada, se encuentran uno o dos má-

ximos en el espectro de la significancia, dependiendo de la dimensión de los acoplamientos. La posición de los picos depende del cociente $m_{t\bar{t}}^{\min}/m_G$ y no de la masa de la resonancia. Uno de los picos se sitúa a una escala de energía igual a un medio de la masa de la resonancia o incluso más baja. Por lo tanto, se pueden usar muestras de datos de quarks top y antitop que no sean muy energéticos para detectar o excluir la existencia de este tipo de resonancias. Hemos calculado también la luminosidad integrada necesaria para obtener una significancia estadística igual a 5. De acuerdo con el análisis de la significancia, hemos encontrado que aparece un mínimo en la luminosidad para bajos valores del corte en $m_{t\bar{t}}^{\min}/m_G$. Fijando dicho corte a los valores que maximizan la significancia, hemos escaneado el espacio de los parámetros (g_A, g_V), encontrando que los patrones de la asimetría y de la significancia no dependen de la masa de la resonancia, sino solamente de $m_{t\bar{t}}^{\min}/m_G$.

Sucesivamente, hemos analizado la producción de pares de quarks top junto con un *jet*. En este caso, la asimetría es un efecto de nivel árbol y recibe contribuciones de estados finales tanto octetos como singletes de color. Este proceso es importante en el LHC y es especialmente significativo para probar aquellos modelos de resonancias en los cuales la producción inclusiva de pares top-antitop no genera una simetría de carga a nivel árbol. Éste es el caso, por ejemplo, de la mayoría de las excitaciones de Kaluza-Klein en modelos de dimensiones extra. Una vez calculada la sección eficaz diferencial para $t\bar{t}$ + *jet*, hemos realizado el mismo análisis del caso inclusivo. Hemos encontrado que se alcanza un mínimo en la luminosidad necesaria para obtener una significancia estadística de 5 para valores bastante bajos del corte en la distribución de la masa invariante del par top-antitop. Una vez más, este resultado abre la posibilidad de usar muestras de tops de baja energía para identificar resonancias también en la producción exclusiva.

El cálculo en presencia de resonancias que hemos llevado a cabo en nuestro trabajo es a nivel árbol. Si bien un análisis más preciso requeriría cálculos a un *loop* para establecer la contribución a la asimetría de los órdenes más altos, nuestro resultado es significativo, porque abre la prometedora posibilidad de medir la asimetría de carga en la producción de pares de top-antitop ya en el primer periodo de funcionamiento del LHC y sin necesidad de analizar tops muy energéticos y por ende difíciles de reconstruir.

Appendix A

BCFW recursion relations

The heart of these relations is to reconstruct the n–point amplitude from its singularities. A partial amplitude has singularities like $p_{i,j}^2$ only, because singularities occur when a propagator is put on–shell. Since a partial amplitude has already been color–ordered by extracting color factors, propagators only involve a sum of adjacent momenta. Let us take a gluon propagator as an example. In the limit of such a propagator going on–shell, it becomes:

$$\frac{i\delta_{ab}}{q^2}\left(-g_{\mu\nu}+\frac{n_\mu q_\nu+q_\mu n_\nu}{q\cdot n}\right)=\frac{i\delta_{ab}}{q^2}\sum_{h=\pm}\varepsilon_\mu^{h*}(q)\varepsilon_\nu^h(q)\,, \tag{A.1}$$

where n is the reference momentum of the polarization. Thus, the amplitude in the limit $P_{1,m}^2\to 0$ takes the form:

$$A_n(1,\ldots,n)\sim\sum_{h=\pm}A_{m+1}^L(1,\ldots,m,P^h)\frac{i}{P_{1,m}^2}A_{n-m+1}^R(-P^{-h},m+1,\ldots,n), \tag{A.2}$$

where we used the notation $P_{1,m}=p_1+p_2+\ldots+p_m$ and we notice that both the amplitudes are on–shell. The sum is carried out on the helicities of the internal propagator. Notice that, since in our convention all the particles are outgoing, the propagator must flip the helicity. BCFW recursion relations have exactly the same form of (A.2) with a shift performed on a spinor of the left amplitude and on a spinor of the right one.

A.1 Massless shift

Let us start considering a shift on massless particles. A (j,k) shift can be:

$$\begin{aligned}|\hat{j}] &= |j]-z|k], \qquad |\hat{j}\rangle=|j\rangle\\ |\hat{k}\rangle &= |k\rangle+z|j\rangle, \qquad |\hat{k}]=|k]\end{aligned} \tag{A.3}$$

where the shifted objects are indicated by a hat and z is a complex number. The Gordon identity

$$[i|\gamma^\mu|i\rangle=\langle i|\gamma^\mu|i]=2k_i^\mu \tag{A.4}$$

gives the following shift on the momenta:

$$\begin{aligned}\hat{p}_j^\mu(z) &= p_j^\mu - \frac{z}{2}\langle j|\gamma^\mu|k] \\ \hat{p}_k^\mu(z) &= p_k^\mu + \frac{z}{2}\langle j|\gamma^\mu|k].\end{aligned} \tag{A.5}$$

Thus, we have an amplitude that depends on z:

$$A(z) = A(p_1, .., \hat{p}_j(z), \ldots, \hat{p}_k(z), \ldots, p_n)\,. \tag{A.6}$$

This amplitude can have poles only when a propagator vanishes, that is:

$$0 = \hat{p}_{i,r}^2(z) = p_{i,r}^2 - z\langle j|\not{p}_{i,r}|k] \tag{A.7}$$

where the j momentum is assumed to belong to (i, r) and the mass is present or not according to which particle is being propagated. Thus, $A(z)$ has only simple poles in:

$$z_{i,r} = \frac{p_{i,r}^2}{\langle j|\not{p}_{i,r}|k]} \tag{A.8}$$

and it can be written as

$$A(z) = \frac{c(z)}{p_{i,r}^2 - z\langle j|\not{p}_{i,r}|k]} = -\frac{c(z)}{\langle j|\not{p}_{i,r}|k]\left(z - \frac{p_{i,r}^2}{\langle j|\not{p}_{i,r}|k]}\right)} = -\frac{c(z)}{\langle j|\not{p}_{i,r}|k](z - z_{i,r})}. \tag{A.9}$$

We know from complex analysis the residue theorem, that holds for an analytic function $f(z)$ except for isolated singular points inside the contour γ, that

$$\frac{1}{2\pi i}\oint_{\gamma\in\infty} f(z)dz = \sum_{\text{poles}} \text{Res}\, f(z). \tag{A.10}$$

Defining

$$f(z) \equiv \frac{A(z)}{z}, \tag{A.11}$$

we can write Eq. (A.10) as:

$$\frac{1}{2\pi i}\oint_{\gamma\in\infty} \frac{A(z)}{z}dz = \sum_{\text{poles}} \text{Res}\,\frac{A(z)}{z} = A(0) + \sum_{\substack{\text{poles of} \\ A(z)}} \text{Res}\,\frac{A(z)}{z} \tag{A.12}$$

where $A(0)$ is exactly the residue of $A(z)/z$ in $z = 0$. We have seen (Eq. (A.7)) that $A(z)$ has linear poles (i.e. of order 1) only in z, therefore the residues have the following form:

$$\underset{z=z_{i,r}}{\text{Res}}\,\frac{A(z)}{z} = \lim_{z\to z_{i,r}} \frac{A(z)}{z}(z - z_{i,r}). \tag{A.13}$$

Replacing $A(z)$ with the expression (A.9), we find:

$$\begin{aligned}\operatorname*{Res}_{z=z_{i,r}} \frac{A(z)}{z} &= -\lim_{z\to z_{i,r}} \frac{c(z)}{z\langle j|\not{p}_{i,r}|k](z-z_{i,r})}(z-z_{i,r}) = -\frac{c(z_{i,r})}{z_{i,r}\langle j|\not{p}_{i,r}|k]} = \\ &= -\frac{c(z_{i,r})}{p_{i,r}^2}. \end{aligned} \tag{A.14}$$

Let us now go back to the residue theorem Eq. (A.12). We observe that if $A(z)/z$ has a behaviour at least like $1/z^2$, the left–hand side vanishes, because the integral goes to zero when $z \to \infty$. In this case, the theorem tells us that

$$A(0) = -\sum_{\substack{\text{poles of}\\ A(z)}} \operatorname{Res} \frac{A(z)}{z} = \sum_{i,r} \frac{c(z_{i,r})}{p_{i,r}^2}. \tag{A.15}$$

We have seen in Eq. (A.2) that, near the pole, the amplitude splits into two parts, thus we can identify the residues of $A(z)$ with the product of A_L and A_R. The final expression is thus:

$$A = A(0) = \sum_{i,r}\sum_{h=\pm} A_{ir}^L(z_{ir})\frac{i}{p_{ir}^2}A_{ir}^R(z_{ir}). \tag{A.16}$$

In summary, in the expression (A.16) we have a sum over the different multiparticle singularities that can arise in the amplitude. This different singularities translate in the different ways that exist of dividing the amplitude in a left and a right part. These amplitudes are evaluated in the correspondent poles and are summed over the possible helicities of the propagator, too. The denominator is simply the propagator unshifted, i. e. evaluated in $z = 0$. The graphic representation of BCFW recursion relations is related in Figure A.1.

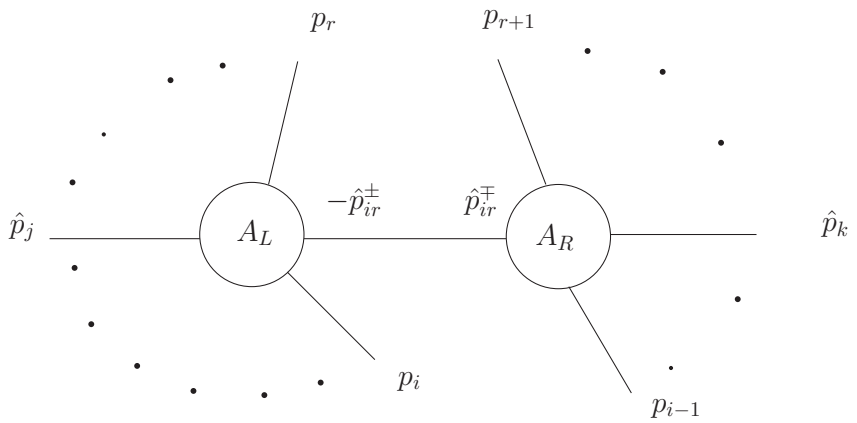

Figure A.1: Decomposition of an amplitude in BCFW recursion relations.

To complete this discussion, let us consider the three point amplitudes that can appear in (A.16) [117]. In the usual Minkowski space $(+---)$ $A_3(1,2,3) = 0$, due to momentum conservation. We can see this by noticing that every scalar product among two of the three momenta is zero, since

$$0 = p_3^2 = (p_1 + p_2)^2 = 2p_1 \cdot p_2 \,. \tag{A.17}$$

This means that either $\langle ij \rangle$ or $[ij]$ are zero, but, since they are connected by (2.25), if one is zero, the other is zero, too. The amplitude is proportional to these spinorial products, thus one finds that this amplitude vanishes. Instead, if we deal with a space with signature $(--++)$, these amplitudes do not vanish so trivially. What is the difference? In the new signature, $\tilde{\lambda}_i$ and $\overline{\lambda}_i$, in the notation of 2.2 are independent, thus the equation

$$p_i \cdot p_j = 0 \tag{A.18}$$

has two solutions: either $\langle ij \rangle = 0$ or $[ij] = 0$. Therefore, the three–point amplitude does not always vanishes. Nevertheless, there will be amplitudes that are null, depending on the shift performed on the momenta [35].

A.2 Massive shift

If the shift is performed over a massive particle, we have to change slightly Eq. (A.3). We will perform our analysis about massive quarks [52], but a similar one is valid for other particles like massive scalars. As said in the previous section, we want to perform a shift on the jth and the kth particle, but now the jth particle is a massive quark, while the kth is a gluon. For the massive particle it is useful to build a lightlike momentum related to it:

$$\ell_j := p_j - \frac{p_j^2}{2p_k \cdot p_k} p_k \,. \tag{A.19}$$

It is easy to see that ℓ_j is massless by construction. A spinorial representation can be applied to massive fermions, too, with the help of a reference momentum. Choosing this momentum equal to k, it reads:

$$\begin{aligned} u_+(p_j) &= \frac{(\not{p}_j + m)}{[\ell_j k]} |k], \qquad \overline{u}_+(p_j) = \langle k| \frac{(\not{p}_j + m)}{\langle k \ell_j \rangle}, \\ u_-(p_j) &= \frac{(\not{p}_j + m)}{\langle \ell_j k \rangle} |k\rangle, \qquad \overline{u}_-(p_j) = [k| \frac{(\not{p}_j + m)}{[k \ell_j]} \,. \end{aligned} \tag{A.20}$$

Such spinors have the correct massless limit, as can be verified by replacing p_j with the relationship given in A.19

$$\begin{aligned} u_+(p_j) &= |j\rangle, \qquad \overline{u}_+(p_j) = [j|, \\ u_-(p_j) &= |j], \qquad \overline{u}_-(p_j) = \langle j|, \end{aligned} \tag{A.21}$$

they satisfy the Dirac equations

$$(\not{p} - m)u_{\pm}(p) = 0, \qquad \overline{u}_{\pm}(p)(\not{p} - m) = 0, \tag{A.22}$$

and the completeness relation

$$\sum_{h=\pm} u_h(p)\overline{u}_h(p) = \not{p} + m\,. \tag{A.23}$$

As we saw in the previous section, we can make two different shifts, depending on the helicities of the involved particles. The one that corresponds to (A.3) is the so called anti–holomorphic shift, and it is given by

$$\begin{aligned} \widehat{u}_-(p_j) &= u_-(p_j) - z|k] \\ |\widehat{k}\rangle &= |k\rangle + z|j\rangle\,. \end{aligned} \tag{A.24}$$

To find how the momenta change, we use the following relationship among spinors and momenta:

$$p^\mu = \frac{1}{4}\mathrm{Tr}\Big(\gamma^\mu \sum_{h=\pm} u_h(p)\overline{u}_h(p)\Big)\,, \tag{A.25}$$

that brings to

$$\begin{aligned} \hat{p}_j^\mu &= p_j^\mu - \frac{z}{2}\langle \ell_j|\gamma^\mu|k] \\ \hat{p}_k^\mu &= p_k^\mu + \frac{z}{2}\langle \ell_j|\gamma^\mu|k]\,. \end{aligned} \tag{A.26}$$

In particular, we explicitly develop the contraction with the gamma matrices

$$\hat{\not{p}}_j = \not{\ell}_j + \frac{m^2}{2\ell_j \cdot p_k}\not{p}_k - z\Big(|k]\langle \ell_j| + |\ell_j\rangle[k|\Big). \tag{A.27}$$

If the momentum of the propagator is $-\hat{P}_{i,r}$, with $j \in (i,r)$, the on–shell condition $\hat{P}_{i,r}^2 = m_P^2$ imposes the value for z:

$$z = +\frac{P_{i,r}^2 - m_P^2}{\langle \ell_j|\not{P}_{i,r}|k]}. \tag{A.28}$$

The holomorphic shift causes the opposite change on the spinors:

$$\begin{aligned} \widehat{u}_-(p_j) &= u_-(p_j) - z|k\rangle \\ |\widehat{k}] &= |k] + z|j]\,. \end{aligned} \tag{A.29}$$

This analysis can be carried out also if both the shifted particles are massive, extending what has been done for p_j to p_k.

As we have seen before, BCFW recursion relations hold if the amplitude $A(z)$ goes to zero at ∞. This condition imposes a set of constraints on our choice of the shift:

- The shift cannot be performed on both fermions belonging to the same line.
- The holomorphic shift can be used for the helicity configurations (j^+, k^-), (j^+, k^+) and (j^-, k^-) except than for some specific configuration such as (q_j^+, g_k^+), $(\bar{q}_j^+, g_k^+)$, (g_j^-, q_k^-), $(g_j^-, \bar{q}_k^-)$.
- The anti–holomorphic shift can be used for the helicity configurations (j^-, k^+), (j^+, k^+) and (j^-, k^-) except than for some specific configuration such as (q_j^-, g_k^-), $(\bar{q}_j^-, g_k^-)$, (g_j^+, q_k^+), $(g_j^+, \bar{q}_k^+)$.

Appendix B

The $t\bar{t}$ production cross sections

Before recalling the different contributions to the heavy quark production cross section, let us define the notation that we have used. All the scalar invariants are normalized to the partonic center of mass energy $\hat{s}$:

$$y_{ij} \equiv 2\,\frac{p_i \cdot p_j}{\hat{s}}\,, \qquad m^2 \equiv \frac{m_Q^2}{\hat{s}}\,. \tag{B.1}$$

Moreover,

$$\beta \equiv \sqrt{1-4m^2}\,, \qquad c \equiv \beta\cos\hat{\theta}\,. \tag{B.2}$$

The polar angle of the top quark with respect to the incoming quark in the center of mass rest frame is called $\hat{\theta}$, and the color factors read $d^2_{abc} = 2C_F(N_c^2-4) = 40/3$ and $f^2_{abc} = 2C_F N_c^2 = 24$, with $N_c = 3$, $T_F = 1/2$ and $C_F = 4/3$.

The asymmetric part of a cross section is defined as:

$$d\sigma_A \equiv \frac{1}{2}[d\sigma(Q) - d\sigma(\bar{Q})]\,, \tag{B.3}$$

for every final state.

B.1 QCD

The Born cross sections for $q\bar{q}$ annihilation and gg fusion to heavy quarks are:

$$\frac{d\sigma^{q\bar{q}\to Q\bar{Q}}}{d\cos\hat{\theta}} = \alpha_s^2\,\frac{T_F C_F}{N_c}\,\frac{\pi\beta}{2\hat{s}}(1+c^2+4m^2)\,, \tag{B.4}$$

$$\frac{d\sigma^{gg\to Q\bar{Q}}}{d\cos\hat{\theta}} = \alpha_s^2\,\frac{\pi\beta}{2\hat{s}}\left(\frac{1}{N_c(1-c^2)} - \frac{T_F}{2C_F}\right)\left(1+c^2+8m^2-\frac{32m^4}{1-c^2}\right)\,. \tag{B.5}$$

In the hard gluon radiation process

$$q(p_1) + \bar{q}(p_2) \to Q(p_3) + \bar{Q}(p_4) + g(p_5) \ , \tag{B.6}$$

the asymmetric part of the bremsstrahlung interference (see Fig. 4.4 $(d+f) \otimes (e+g)$) is given by:

$$\begin{aligned}
\frac{d\sigma_A^{q\bar{q},\mathrm{hard}}}{dy_{35}\, dy_{45}\, d\Omega} &= \frac{\alpha_s^3}{4\pi\hat{s}}\, \frac{d_{abc}^2}{16N_c^2}\, \frac{1}{y_{12}\,(y_{34}+2m^2)\,y_{35}} \times \\
&\times \left\{ \frac{y_{13}}{y_{15}} \left(y_{13}^2 + y_{14}^2 + y_{23}^2 + y_{24}^2 + 2m^2(y_{34}+2m^2+y_{12}) \right) + 4m^2\, y_{24} \right\} + \\
&- (1 \leftrightarrow 2) - (3 \leftrightarrow 4) + (1 \leftrightarrow 2, 3 \leftrightarrow 4) \ .
\end{aligned} \tag{B.7}$$

Expression (B.7), once integrated in the phase space down to a cut w in the energy of the soft gluon, gives a contribution to the asymmetry formed by a part that is infrared singular and another one that depends on the cutoff. The singularity is cancelled exactly by the infrared divergence that origins in the virtual radiation (Fig. 4.4 $a \otimes (b+c)$). The sum of the soft and virtual radiative corrections is given by [86]:

$$\begin{aligned}
\frac{d\sigma_A^{q\bar{q},\mathrm{virt+soft}}}{d\cos\hat{\theta}} &= \frac{\alpha_s^3}{2\hat{s}}\, \frac{d_{abc}^2}{16N_c^2}\ \beta \left\{ B(c) - B(-c) + \right. \\
&+ \left. (1 + c^2 + 4m^2) \left[4 \log\left(\frac{1-c}{1+c} \right) \log(2w) + D(c) - D(-c) \right] \right\} \ ,
\end{aligned} \tag{B.8}$$

with the functions $B(c)$, coming from the box contribution, and $D(c)$, from soft radiation, defined as:

$$\begin{aligned}
B(c) &= \frac{1-c^2-8m^2}{1-c-2m^2} \log\left(\frac{1-c}{2} \right) + (c+2m^2) \left[2\,\mathrm{Li}_2\left(1 - \frac{2m^2}{1-c} \right) - \log^2\left(\frac{1-c}{2} \right) \right] + \\
&+ \frac{4c}{\beta^2} \frac{2-c^2-7m^2}{(1-2m^2)^2-c^2}\, m^2\ \log(m^2) + \frac{c}{2} \log^2(m^2) + \\
&- \frac{c}{2\beta^3}(1 - 8m^2 + 8m^4) \left[\log^2\left(\frac{1-\beta}{1+\beta} \right) + 4\,\mathrm{Li}_2\left(-\frac{1-\beta}{1+\beta} \right) + \frac{\pi^2}{3} \right] - c\,\frac{\pi^2}{6} \ ,
\end{aligned} \tag{B.9}$$

$$\begin{aligned}
D(c) &= 2\,\mathrm{Re} \left\{ \mathrm{Li}_2\left(\frac{-x}{1-y} \right) - \mathrm{Li}_2\left(\frac{1-x}{1-y} \right) - \mathrm{Li}_2\left(\frac{1+x}{y} \right) + \mathrm{Li}_2\left(\frac{x}{y} \right) \right\} + \\
&+ \log^2\left| \frac{y}{1-y} \right| - \mathrm{Re}\left\{ \mathrm{Li}_2(x^2) \right\} + \frac{1}{2} \log^2(x^2) - \log(x^2) \log(1-x^2) \ ,
\end{aligned} \tag{B.10}$$

where

$$x = \frac{1-c}{\sqrt{2(1-c-2m^2)}} \ , \qquad y = \frac{1}{2}\left(1 - \beta + \sqrt{2(1-c-2m^2)} \right) \ . \tag{B.11}$$

The dependence on w is compensated by the integration of (B.7) in the complementary phase space.

The asymmetric contribution from the $q(\bar{q})g$ originated process

$$q(\bar{q})(p_1) + g(p_2) \to Q(p_3) + \bar{Q}(p_4) + q(\bar{q})(p_5) \ , \tag{B.12}$$

is:

$$\begin{aligned}\frac{d\sigma_A^{qg}}{dy_{35}\,dy_{45}\,d\Omega} &= \frac{\alpha_s^3}{4\pi\hat{s}}\,\frac{d_{abc}^2}{16N_c^2}\,\frac{1}{y_{15}\,(y_{34}+2m^2)\,y_{23}}\times \\ &\times \left\{\left(\frac{y_{13}}{y_{12}}-\frac{y_{35}}{y_{25}}\right)\left(y_{13}^2+y_{14}^2+y_{35}^2+y_{45}^2+2m^2(y_{34}+2m^2-y_{15})\right)+\right. \\ &\left.+4m^2\,(y_{45}+y_{14})\right\}-(3\leftrightarrow 4)\ . \end{aligned}\tag{B.13}$$

It is infrared finite and can be obtained just by crossing of momenta from (B.7).

B.2 Heavy colored resonance

Let us define the propagator of the heavy resonance as:

$$G(s) = \frac{1}{s - m_G^2 + i\,m_G\,\Gamma_G}\ , \tag{B.14}$$

where m_G is the mass of the resonance and Γ_G is the decay width, given by:

$$\begin{aligned}\Gamma_G &\equiv \sum_q \Gamma(G\to q\overline{q}) = \frac{\alpha_s\,m_G\,T_F}{3}\left[\sum_q\left((g_V^q)^2+(g_A^q)^2\right)+\right. \\ &\left.+\sqrt{1-\frac{4m_t^2}{m_G^2}}\left((g_V^t)^2\left(1+\frac{2m_t^2}{m_G^2}\right)+(g_A^t)^2\left(1-\frac{4m_t^2}{m_G^2}\right)\right)\right]\ . \end{aligned}\tag{B.15}$$

Having $G(s)$ both real and imaginary part, it is useful to have at hand some quantities:

$$\begin{aligned}&\mathrm{Re}\{G(\hat{s})\} = \frac{\hat{s}-m_G^2}{(\hat{s}-m_G^2)^2+m_G^2\Gamma_G^2}\ , \qquad \mathrm{Im}\{G(\hat{s})\} = -\frac{m_G\,\Gamma_G}{(\hat{s}-m_G^2)^2+m_G^2\Gamma_G^2}\ , \\ &|G(\hat{s})|^2 = \frac{1}{(\hat{s}-m_G^2)^2+m_G^2\Gamma_G^2}\ , \\ &\mathrm{Re}\{G(\hat{s})^\dagger G(\hat{s}_{34})\} = \frac{(\hat{s}_{34}-m_G^2)(\hat{s}-m_G^2)+m_G^2\Gamma_G^2}{[(\hat{s}-m_G^2)^2+m_G^2\Gamma_G^2]\,[(\hat{s}_{34}-m_G^2)^2+m_G^2\Gamma_G^2]}\ , \\ &\mathrm{Re}\{G(\hat{s})G(\hat{s}_{34})\} = \frac{(\hat{s}_{34}-m_G^2)(\hat{s}-m_G^2)-m_G^2\Gamma_G^2}{((\hat{s}-m_G^2)^2+m_G^2\Gamma_G^2)((\hat{s}_{34}-m_G^2)^2+m_G^2\Gamma_G^2)} \\ &\mathrm{Im}\{G(\hat{s})^\dagger G(\hat{s}_{34})\} = \frac{(\hat{s}_{34}-\hat{s})\,m_G\,\Gamma_G}{[(\hat{s}-m_G^2)^2+m_G^2\Gamma_G^2]\,[(\hat{s}_{34}-m_G^2)^2+m_G^2\Gamma_G^2]}\ , \end{aligned}\tag{B.16}$$

The Born cross-section for $q\bar{q}$ annihilation to heavy quarks in the presence of a color-octet vector resonance reads:

$$\begin{aligned}\frac{d\sigma^{q\bar{q}\to Q\bar{Q}}}{d\cos\hat{\theta}} &= \alpha_s^2\,\frac{T_F C_F}{N_c}\,\frac{\pi\beta}{2\hat{s}}\Bigg(1+c^2+4m^2+\\ &+ 2\hat{s}\,\mathrm{Re}\{G(\hat{s})\}\left[g_V^q\,g_V^t\,(1+c^2+4m^2)+2\,g_A^q\,g_A^t\,c\right]+\\ &+ \hat{s}^2\,|G(\hat{s})|^2\Bigg[\left((g_V^q)^2+(g_A^q)^2\right)\Bigg((g_V^t)^2(1+c^2+4m^2)+\\ &+ (g_A^t)^2(1+c^2-4m^2)\Bigg)+8\,g_V^q\,g_A^q\,g_V^t\,g_A^t\,c\Bigg]\Bigg)\,. \end{aligned} \tag{B.17}$$

The parameters $g_V^q(g_V^t)$, $g_A^q(g_A^t)$ represent the vector and axial-vector couplings among the excited gluons and the light quarks (top quarks).

There are two terms in Eq. (B.17) that are odd in the polar angle and therefore there are two contributions to the charge asymmetry. The first one arises from the interference of the SM amplitude with the resonance amplitude, and the second one from the squared resonance amplitude. The former depends on the axial-vector couplings only, while the latter is proportional to both the vector and the axial-vector couplings. For large values of the resonance mass, the second term is suppressed, and the charge asymmetry will depend mostly on the value of the axial-vector couplings, and residually on the vector couplings.

The charge asymmetric piece of the hard gluon radiation process

$$q(p_1) + \bar{q}(p_2) \to Q(p_3) + \bar{Q}(p_4) + g(p_5) \ , \tag{B.18}$$

is given by:

$$\begin{aligned}
\frac{d\sigma_A^{q\bar{q},hard}}{dy_{35}\,dy_{45}\,d\Omega} &= \frac{\alpha_s^3\,\hat{s}}{4\pi N_c^2}\Bigg\{ \frac{d_1}{\hat{s}\,\hat{s}_{34}} + \left(g_V^q\,g_V^t\,d_1 - g_A^q\,g_A^t\,f_1\right)\mathrm{Re}\left\{\frac{G(\hat{s}_{34})}{\hat{s}}\right\} + \\
&+ \left(g_V^q\,g_V^t\,d_1 + g_A^q\,g_A^t\,(-f_1+f_7+2f_2)\right)\mathrm{Re}\left\{\frac{G(\hat{s})}{\hat{s}_{34}}\right\} + \\
&+ \left(g_V^q\,g_A^t\,f_3 + g_A^q\,g_V^t\,d_3\right)\mathrm{Im}\left\{\frac{G(\hat{s})}{\hat{s}_{34}} - \frac{G(\hat{s}_{34})}{\hat{s}}\right\} + \\
&+ \left[\left((g_V^q)^2+(g_A^q)^2\right)\left((g_V^t)^2\,d_1 + (g_A^t)^2\,d_2\right) - 4\,g_V^q\,g_A^q\,g_V^t\,g_A^t\ (f_1+f_2)\right]\times \\
&\quad \times\mathrm{Re}\{G(\hat{s})^\dagger G(\hat{s}_{34})\} - 2\left[\left((g_V^q)^2+(g_A^q)^2\right)\ g_V^t\,g_A^t\,f_3 + \right. \\
&+ \left. g_V^q\,g_A^q\ \left((g_V^t)^2\,d_3 + (g_A^t)^2\,d_4\right)\right]\mathrm{Im}\{G(\hat{s})^\dagger G(\hat{s}_{34})\} + \\
&+ (d_5+f_4)\left[g_A^q\,g_A^t\mathrm{Re}\left\{\frac{G(\hat{s})}{\hat{s}}\right\} + 2\,g_A^q\,g_A^t\,g_V^q\,g_V^t|G(\hat{s})|^2\right] + \\
&+ (d_6+f_5)\left[g_A^q\,g_A^t\mathrm{Re}\left\{\frac{G(\hat{s}_{34})}{\hat{s}_{34}}\right\} + 2\,g_A^q\,g_A^t\,g_V^q\,g_V^t|G(\hat{s}_{34})|^2\right] + \\
&+ g_A^q\,g_A^t\,f_6\mathrm{Re}\left\{\frac{G(\hat{s}_{34})}{\hat{s}_{34}}\right\} + g_A^q\,g_A^t\,((f_6+f_9)\frac{\hat{s}}{\hat{s}_{34}} + f_7 - 2f_2)\mathrm{Re}\{G(\hat{s})G(\hat{s}_{34})\} + \\
&+ g_V^q\,g_A^t f_8\left[-\mathrm{Im}\{G(\hat{s})G(\hat{s}_{34})\}\frac{\hat{s}}{\hat{s}_{34}} + \mathrm{Im}\left\{\frac{G(\hat{s}_{34})}{\hat{s}_{34}}\right\}\right] + \\
&+ 2g_A^t\,g_V^t\left[g_A^q\,g_V^q\hat{s}^2\left[2\left(f_6\left(1-\frac{m_G^2}{\hat{s}}\right) + (f_7+f_2)\left(y_{34}+m^2-\frac{m_G^2}{\hat{s}}\right)\right) + f_9\right] + \right. \\
&\quad \left. +((g_A^q)^2+(g_V^q)^2)f_8\frac{m_G\Gamma_G}{\hat{s}}\right]\times|G(\hat{s})|^2|G(\hat{s}_{34})|^2 \\
&- (3\leftrightarrow 4)\Bigg\}
\end{aligned} \tag{B.19}$$

where

$$
\begin{aligned}
d_1 &= \frac{c_d}{y_{35}}\left[\left(\frac{y_{13}}{y_{15}}-\frac{y_{23}}{y_{25}}\right)\left(y_{13}^2+y_{14}^2+y_{23}^2+y_{24}^2+2m^2\left(y_{34}+2m^2+1\right)\right)+4m^2\left(y_{24}-y_{14}\right)\right] \ , \\
d_2 &= \frac{c_d}{y_{35}}\left[\left(\frac{y_{13}}{y_{15}}-\frac{y_{23}}{y_{25}}\right)\left(y_{13}^2+y_{14}^2+y_{23}^2+y_{24}^2-2m^2\left(y_{34}+2m^2+1\right)\right)+4m^2\left(y_{13}-y_{23}\right)\right] \ , \\
d_3 &= \frac{c_d}{y_{35}}\left[\frac{y_{13}^2+y_{14}^2-y_{23}^2-y_{24}^2-2m^2(y_{15}-y_{25})}{y_{15}\,y_{25}}\right]\frac{4}{\hat{s}^2}\,\epsilon^{p_1\,p_2\,p_3\,p_4} \ , \\
d_4 &= \frac{c_d}{y_{35}}\left[\frac{y_{13}^2+y_{14}^2-y_{23}^2-y_{24}^2+2m^2(y_{15}-y_{25})}{y_{15}\,y_{25}}\right]\frac{4}{\hat{s}^2}\,\epsilon^{p_1\,p_2\,p_3\,p_4} \ , \\
d_5 &= \frac{c_d}{y_{35}}\left[2m^2\left(1-\frac{1-2y_{24}}{y_{35}}\right)+y_{25}+y_{24}(2m^2+y_{34}-1)+(y_{13}-y_{23})\left(\frac{2m^2}{y_{45}}+1\right)+\right. \\
&\quad \left.-(y_{13}y_{24}-y_{14}y_{23})\left(1+\frac{1}{y_{45}}\right)\right] \\
d_6 &= c_d\left[\left(\frac{y_{23}}{y_{15}}-\frac{y_{13}}{y_{25}}\right)y_{45}+\frac{1}{y_{15}y_{25}}(2y_{23}-y_{35}(3y_{14}+y_{35}+y_{13}(y_{35}+y_{45}-3)+1))\right] \\
f_1 &= \frac{c_f}{y_{35}}\left[\left(\frac{y_{23}}{y_{25}}-\frac{y_{13}}{y_{15}}\right)\left(y_{13}^2+y_{14}^2+y_{23}^2+y_{24}^2\right)+\right. \\
&\quad \left.+\ 4\left(\frac{(y_{13}+y_{15})y_{24}(y_{13}-y_{35})}{y_{15}}-\frac{(y_{23}+y_{25})y_{14}(y_{23}-y_{35})}{y_{25}}\right)\right] \ , \\
f_2 &= \frac{c_f}{y_{35}}\left[2m^2\left(y_{15}-y_{25}\right)\right] \ , \\
f_3 &= \frac{c_f}{y_{35}}\left[\frac{y_{13}^2+y_{14}^2-y_{23}^2-y_{24}^2}{y_{15}\,y_{25}}\right]\frac{4}{\hat{s}^2}\,\epsilon^{p_1\,p_2\,p_3\,p_4} \\
f_4 &= \frac{c_f}{y_{35}}\left[6m^2\left(1-\frac{1-2y_{24}}{y_{35}}\right)+3y_{25}+3y_{24}(2m^2+y_{34}-1)-(y_{13}-y_{23})\left(\frac{2m^2}{y_{45}}+1\right)+\right. \\
&\quad \left.+(y_{13}y_{24}-y_{14}y_{23})\left(1+\frac{1}{y_{45}}\right)\right] \\
f_5 &= c_f\left[3\left(\frac{y_{23}}{y_{15}}-\frac{y_{13}}{y_{25}}\right)y_{45}-\frac{1}{y_{15}y_{25}}(2y_{23}-y_{35}(3y_{14}+y_{35}+y_{13}(y_{35}+y_{45}-3)+1))\right] \\
f_6 &= \frac{2c_f}{y_{15}y_{25}}[(y_{23}-y_{25})y_{13}^3-(y_{13}-y_{15})y_{23}^3+(5y_{25}-1+y_{13}+3y_{15}+3y_{14}y_{23})y_{13}^2+ \\
&\quad -(5y_{15}-1+y_{23}+3y_{25}+3y_{24}y_{13})y_{23}^2-4(y_{13}-y_{23})-8y_{14}y_{23}] \\
f_7 &= \frac{2c_f}{y_{35}y_{45}}[y_{35}(y_{23}^3-y_{13}^3)+(-y_{23}+2y_{24}^2-y_{14}y_{23}-y_{14}y_{13}-3y_{14}+5+ \\
&\quad +y_{24}(-11+2y_{23}+4y_{14}))y_{13}^2+4(-1+y_{14}y_{23}+2y_{24}-y_{23}y_{24})y_{13}+ \\
&\quad -(-y_{13}+2y_{14}^2-y_{24}y_{13}-y_{24}y_{23}-3y_{24}+5+y_{14}(-11+2y_{13}+4y_{24}))y_{23}^2+ \\
&\quad -4(-1+y_{24}y_{13}+2y_{14}-y_{13}y_{14})y_{23}] \\
f_8 &= 2c_f\left[\left(\frac{1}{y_{15}}-\frac{1}{y_{25}}\right)(y_{13}+y_{23})+\frac{1}{y_{35}}(y_{13}-y_{23}-y_{14}+y_{24})\right]\frac{4}{\hat{s}^2}\,\epsilon^{p_1\,p_2\,p_3\,p_4} \\
f_9 &= -8c_f((y_{24}-2)y_{13}^2-(y_{14}-2)y_{23}^2+2(y_{13}-y_{23})-4y_{13}y_{24}+y_{14}y_{24}(y_{13}-y_{23})) \qquad \text{(B.20)}
\end{aligned}
$$

The colour factor are $c_d = \frac{d^2_{abc}}{16}$ and $c_f = \frac{f^2_{abc}}{16}$.

The charge asymmetric contribution of the flavor excitation process

$$q(\bar{q})(p_1) + g(p_2) \to Q(p_3) + \bar{Q}(p_4) + q(\bar{q})(p_5) \ , \tag{B.21}$$

is infrared finite and can be obtained just by crossing of the momenta ($2 \leftrightarrow 5$) from Eq. (B.19).

Bibliography

[1] L. Evans and P. Bryant, JINST **3**, S08001 (2008).

[2] J. Alcaraz *et al.* [LEP Collaborations and ALEPH Collaboration and DELPHI Collaboration and L3 Collaboration and OPAL Collaboration and LEP Electroweak Working Group], arXiv:0712.0929 [hep-ex].

[3] F. Ambroglini *et al.*, "Proceedings of the Workshop on Monte Carlo's, Physics and Simulations at the LHC PART I," arXiv:0902.0293 [hep-ph].

[4] J. R. Ellis, Nature **448**, 297 (2007).

[5] Z. Bern *et al.* [NLO Multileg Working Group], "The NLO multileg working group: Summary report,", published in "Les Houches 2007, Physics at TeV colliders", 1-120 arXiv:0803.0494 [hep-ph].

[6] J. A. M. Vermaseren, A. Vogt and S. Moch, Nucl. Phys. B **724**, 3 (2005).

[7] R. K. Ellis, W. J. Stirling and B. R. Webber, "QCD and Collider Physics", Cambridge University Press.

[8] P. Nason "Introduction to QCD" Prepared for The 1997 European School of High Energy Physics, Menstrup, Denmark, 25 May-7 Jun 1997.

[9] G. Hanson *et al.*, Phys. Rev. Lett. **35**, 1609 (1975).

[10] F. Wilczek, Proc. Nat. Acad. Sci. **102**, 8403 (2005) [Int. J. Mod. Phys. A **20**, 5753 (2005 RMPHA,77,857-870.2005)].

[11] ZEUS Collaboration (S. Chekanov *et al.*), Phys. Rev. D67:012007, 2003

[12] S. Bethke, Eur. Phys. J. C **64**, 689 (2009)

[13] G. Altarelli, arXiv:1002.4957 [hep-ph].

[14] S. D. Ellis, D. E. Soper, Phys. Rev. D **48**, 3160 (1993).

[15] S. Catani, Y. L. Dokshitzer and B. R. Webber, Phys. Lett. B **285**, 291 (1992).

[16] S. D. Ellis, J. Huth, N. Wainer, K. Meier, N. Hadley, D. Soper and M. Greco, Proceedings of Research Directions For The Decade, Snowmass 1990, Snowmass, July 1990, ed. E.L. Berger, p. 134, (World Scientific, Singapore, 1992).

[17] G. P. Salam, G. Soyez, JHEP **0705**, 086 (2007).

[18] M. Cacciari, G. P. Salam and G. Soyez, JHEP **0804**, 063 (2008).

[19] A. Gehrmann-De Ridder, T. Gehrmann, E. W. N. Glover and G. Heinrich, Phys. Rev. Lett. **99**, 132002 (2007). JHEP **0712**, 094 (2007); Phys. Rev. Lett. **100**, 172001 (2008); JHEP **0905**, 106 (2009).

[20] S. Moch, J. A. M. Vermaseren and A. Vogt, Nucl. Phys. B **688**, 101 (2004); Nucl. Phys. B **691**, 129 (2004).

[21] A. Bredenstein, A. Denner, S. Dittmaier and S. Pozzorini, Phys. Rev. Lett. **103**, 012002 (2009).

[22] C. F. Berger *et al.*, Phys. Rev. D **80**, 074036 (2009).

[23] M. L. Mangano and S. J. Parke, Phys. Rept. **200**, 301 (1991).

[24] M. L. Mangano, S. J. Parke and Z. Xu, Nucl. Phys. B **298**, 653 (1988).

[25] Z. Xu, D. H. Zhang and L. Chang, Nucl. Phys. B **291**, 392 (1987).

[26] Z. Kunszt, Nucl. Phys. B **271**, 333 (1986).

[27] M. L. Mangano, Nucl. Phys. B **309**, 461 (1988).

[28] S. J. Parke and T. R. Taylor, Phys. Rev. Lett. **56**, 2459 (1986).

[29] F. A. Berends and W. T. Giele, Nucl. Phys. B **306**, 759 (1988).

[30] Z. Bern, L. J. Dixon and D. A. Kosower, Phys. Rev. D **71**, 105013 (2005); Phys. Rev. D **72**, 125003 (2005) Phys. Rev. D **73**, 065013 (2006)

[31] E. Witten, Commun. Math. Phys. **252**, 189 (2004).

[32] R. Penrose, J. Math. Phys. **8**, 345 (1967).

[33] L. J. Dixon, PoS **HEP2005**, 405 (2006).

[34] F. Cachazo, P. Svrcek and E. Witten, JHEP **0409**, 006 (2004).

[35] R. Britto, F. Cachazo and B. Feng, Nucl. Phys. B **715**, 499 (2005).

[36] P. Mastrolia, "Twistors and unitarity," arXiv:hep-ph/0610190.

[37] R. Britto, F. Cachazo, B. Feng and E. Witten, Phys. Rev. Lett. **94**, 181602 (2005).

[38] S. D. Badger, E. W. N. Glover, V. V. Khoze and P. Svrcek, JHEP **0507**, 025 (2005).

[39] S. D. Badger, E. W. N. Glover and V. V. Khoze, JHEP **0601**, 066 (2006).

[40] S. Dawson and R. P. Kauffman, Phys. Rev. Lett. **68**, 2273 (1992).

[41] R. P. Kauffman, S. V. Desai and D. Risal, Phys. Rev. D **55**, 4005 (1997) [Erratum-ibid. D **58**, 119901 (1998)].

[42] V. Del Duca, A. Frizzo and F. Maltoni, JHEP **0405**, 064 (2004).

[43] L. J. Dixon, E. W. N. Glover and V. V. Khoze, JHEP **0412**, 015 (2004).

[44] C. Schwinn and S. Weinzierl, JHEP **0603**, 030 (2006).

[45] L. J. Dixon, TASI 95:539-584, [arXiv:hep-ph/9601359].

[46] Z. Bern, L. J. Dixon and D. A. Kosower, Ann. Rev. Nucl. Part. Sci. **46**, 109 (1996).

[47] D. Forde and D. A. Kosower, Phys. Rev. D **73**, 065007 (2006).

[48] P. Ferrario, G. Rodrigo and P. Talavera, Phys. Rev. Lett. **96**, 182001 (2006).

[49] C. F. Berger, V. Del Duca and L. J. Dixon, Phys. Rev. D **74**, 094021 (2006) [Erratum-ibid. D **76**, 099901 (2007)].

[50] T. Figy and D. Zeppenfeld, Phys. Lett. B **591**, 297 (2004).

[51] G. Rodrigo, JHEP **0509**, 079 (2005).

[52] C. Schwinn and S. Weinzierl, JHEP **0704**, 072 (2007).

[53] F. Abe *et al.*, Phys. Rev. Lett. 73, 225 (1994).

[54] S. Abachi *et al.* [D0 Collaboration], Phys. Rev. Lett. **74**, 2632 (1995).

[55] S. W. Herb *et al.*, Phys. Rev. Lett. **39**, 252 (1977).

[56] J. R. Incandela, A. Quadt, W. Wagner and D. Wicke, Prog. Part. Nucl. Phys. **63**, 239 (2009).

[57] [Tevatron Electroweak Working Group and CDF Collaboration and D0 Collaboration], CDF Note 9717, D0 Note 5899 arXiv:0903.2503 [hep-ex].

[58] W. Bernreuther, J. Phys. G **35**, 083001 (2008).

[59] T. Aaltonen *et al.* [CDF Collaboration], Phys. Rev. Lett. **102**, 222003 (2009).

[60] C. T. Hill and E. H. Simmons Phys. Rept. **381**, 235 (2003) [Erratum-ibid. **390**, 553 (2004)].

[61] J. M. Campbell, J. W. Huston and W. J. Stirling Rept. Prog. Phys. **70**, 89 (2007).

[62] Y. L. Dokshitzer, Sov. Phys. JETP **46** (1977) 641; L. N. Lipatov, Sov. J. Nucl. Phys. **20** (1975) 95; V. N. Gribov and L. N. Lipatov, Sov. J. Nucl. Phys. **15** 438 (1972); G. Altarelli and G. Parisi, Nucl. Phys. **B126** 298 (1977).

[63] Y. Bai and Z. Han, JHEP **0904**, 056 (2009).

[64] U. Baur and L. H. Orr, Phys. Rev. D **77**, 114001 (2008).

[65] J. C. Pati and A. Salam, Phys. Lett. B **58** 333 (1975); L. J. Hall and A. E. Nelson, Phys. Lett. B **153** 430 (1985); J. Bagger, C. Schmidt and S. King, Phys. Rev. D **37** 1188 (1988);

[66] F. Cuypers, Z. Phys. C **48** 639 (1990).

[67] P. H. Frampton and S. L. Glashow, Phys. Lett. B **190** 157 (1987); P. H. Frampton and S. L. Glashow, Phys. Rev. Lett. **58** 2168 (1987).

[68] C. T. Hill, Phys. Lett. B **266** 419 (1991); C. T. Hill and S. J. Parke, Phys. Rev. D **49** 4454 (1994); R. S. Chivukula, A. G. Cohen and E. H. Simmons, Phys. Lett. B **380** 92 (1996).

[69] D. A. Dicus, C. D. McMullen and S. Nandi, Phys. Rev. D **65** 076007 (2002).

[70] L. Randall and R. Sundrum, Phys. Rev. Lett. **83** 3370 (1999).

[71] K. Agashe, A. Belyaev, T. Krupovnickas, G. Perez and J. Virzi, Phys. Rev. D **77** 015003 (2008).

[72] K. Agashe, A. Falkowski, I. Low and G. Servant, JHEP **0804** 027 (2008).

[73] B. Lillie, L. Randall and L. T. Wang, JHEP **0709** 074 (2007); B. Lillie, J. Shu and T. M. P. Tait, Phys. Rev. D **76** 115016 (2007).

[74] A. Djouadi, G. Moreau and R. K. Singh, Nucl. Phys. B **797** 1 (2008).

[75] J. Bagger, C. Schmidt and S. King, Phys. Rev. D **37** 1188 (1988).

[76] CDF Collaboration, "Search for new particles decaying to dijets in $p\bar{p}$ collisions at $\sqrt{s} = 1.96$ TeV," CDF note 9246 (2008).

[77] O. Antuñano, J. H. Kühn and G. Rodrigo, Phys. Rev. D **77** 014003 (2008).

[78] G. Rodrigo, PoS **RADCOR2007** 010 (2008) [arXiv:0803.2992 [hep-ph]].

[79] L. M. Sehgal and M. Wanninger, Phys. Lett. B **200** 211 (1988).

[80] D. Choudhury, R. M. Godbole, R. K. Singh and K. Wagh, Phys. Lett. B **657** 69 (2007).

[81] D. Atwood, A. Aeppli and A. Soni, Phys. Rev. Lett. **69**, 2754 (1992).

[82] E. H. Simmons, arXiv:hep-ph/0011244.

[83] N. Arkani-Hamed, S. Dimopoulos and G. R. Dvali, Phys. Lett. B **429**, 263 (1998); I. Antoniadis, N. Arkani-Hamed, S. Dimopoulos and G. R. Dvali, Phys. Lett. B **436**, 257 (1998).

[84] T. Kaluza, "On The Problem Of Unity In Physics," Sitzungsber. Preuss. Akad. Wiss. Berlin (Math. Phys.) **1921** 966 (1921); O. Klein, Z. Phys. **37** 895 (1926) [Surveys High Energ. Phys. **5** 241 (1986)].

[85] E. Witten, Nucl. Phys. B **186**, 412 (1981).

[86] J. H. Kühn and G. Rodrigo, Phys. Rev. D **59**, 054017 (1999); Phys. Rev. Lett. **81**, 49 (1998).

[87] F. A. Berends, K. J. F. Gaemers and R. Gastmans, Nucl. Phys. B **63**, 381 (1973).

[88] T. Aaltonen *et al.* [CDF Collaboration], Phys. Rev. Lett. **101** 202001 (2008).

[89] V. M. Abazov *et al.* [D0 Collaboration], Phys. Rev. Lett. **100** 142002 (2008).

[90] G. L. Strycker *et al.* [CDF Collaboration], Conf. Note 9724 (March 2009).

[91] R. Bonciani, S. Catani, M. L. Mangano and P. Nason, Nucl. Phys. B **529**, 424 (1998) [Erratum-ibid. B **803**, 234 (2008)].

[92] L. G. Almeida, G. Sterman and W. Vogelsang, Phys. Rev. D **78** 014008 (2008).

[93] S. Dittmaier, P. Uwer and S. Weinzierl, Phys. Rev. Lett. **98**, 262002 (2007).

[94] P. H. Frampton, arXiv:0910.0307 [hep-ph]; P. H. Frampton, J. Shu and K. Wang, arXiv:0911.2955 [hep-ph].

[95] C. D. Carone, J. Erlich and M. Sher, Phys. Rev. D **78** 015001 (2008).

[96] M. V. Martynov and A. D. Smirnov, Mod. Phys. Lett. A **24** 1897 (2009).

[97] A. R. Zerwekh, arXiv:0908.3116 [hep-ph].

[98] A. Djouadi, G. Moreau, F. Richard and R. K. Singh, arXiv:0906.0604 [hep-ph].

[99] A. Arhrib, R. Benbrik and C. H. Chen, arXiv:0911.4875 [hep-ph].

[100] S. Jung, H. Murayama, A. Pierce and J. D. Wells, arXiv:0907.4112 [hep-ph].

[101] K. Cheung, W. Y. Keung and T. C. Yuan, arXiv:0908.2589 [hep-ph].

[102] J. Shu, T. M. P. Tait and K. Wang, arXiv:0911.3237 [hep-ph].

[103] P. Ferrario and G. Rodrigo, Phys. Rev. D **78** 094018 (2008); J. Phys. Conf. Ser. **171**, 012091 (2009).

[104] P. Ferrario and G. Rodrigo, Phys. Rev. D **80** 051701 (2009).

[105] P. Ferrario and G. Rodrigo, JHEP **1002**, 051 (2010).

[106] C. Amsler *et al.* [Particle Data Group], Phys. Lett. B **667**, 1 (2008).

[107] A. D. Martin, W. J. Stirling and R. S. Thorne, Phys. Lett. B **636** 259 (2006).

[108] The Tevatron Electroweak Working Group, "A combination of CDF and D0 results on the mass of the top quark", arXiv:hep-ex/0703034.

[109] CDF Collaboration, CDF note 9913 "Combination of CDF top quark pair production cross section measurements with up to 4.6 fb^{-1}."

[110] M. Cacciari, S. Frixione, M. L. Mangano, P. Nason and G. Ridolfi, JHEP **0404** 068 (2004).

[111] M. Cacciari, S. Frixione, M. M. Mangano, P. Nason and G. Ridolfi, JHEP **0809**, 127 (2008).

[112] "LHC Performance Workshop", Chamonix 2010.

[113] CMS collaboration, JHEP **0210** 041 (2010).

[114] J. Stirling home page, www.hep.phy.cam.ac.uk/$\sim$ wjs/partons2008nlo.jpg

[115] S. Dittmaier, P. Uwer and S. Weinzierl, Eur. Phys. J. C **59**, 625 (2009).

[116] B. Lillie, L. Randall and L. T. Wang, JHEP **0709** 074 (2007); B. Lillie, J. Shu and T. M. P. Tait, Phys. Rev. D **76** 115016 (2007) .

[117] R. Britto, F. Cachazo and B. Feng, Nucl. Phys. B **725**, 275 (2005).